University of Warsaw
Faculty of Physics

DISSERTATION

Many-body Correlations as a Resource for Quantum Metrology

Author:
Artur Niezgoda

Supervisor:
dr hab. Jan Chwedeńczuk

April 17, 2021

Abstract

Many-body Correlations as a Resource for Quantum Metrology

by Artur Niezgoda

Quantum metrology is a field of physics that exploits quantum phenomena in order to increase precision of measurements. In atom interferometry, a branch of metrology, such measurements are bounded by the shot-noise limit whenever the system is classically correlated. It has been shown that states exhibiting quantum correlations – such as entanglement – enhance the sensitivity of quantum sensors, allowing for precision beyond the standard quantum limit. For these reasons, entanglement is a useful resource for quantum metrology. However, the strongest entangled states exhibit a phenomenon known as nonlocality that has been the object of intensive research for several decades. Nonlocally correlated states are also of scientific interest from the perspective of quantum metrology.

We begin by showing that the interference pattern formed by two overlapping Bose-Einstein condensates can be used to detect Bell correlations in the system. In our analysis we include various noise sources present in typical experiments.

In the next step, we explore systems of Bose-Einstein condensates in two-mode and three-mode configurations, in which the entangled states useful for quantum metrology are generated through the dynamics governed by the given Hamiltonians. We show a scheme allowing for ultra-precise measurements that saturate the quantum Cramér-Rao bound.

We then derive a correlator that detects many-body correlations from the single element of the density matrix. Moreover, we show that such an object, properly analyzed, provides information about the extent of many-body entanglement and nonlocality. We illustrate our findings with experimentally accessible interacting spin chains.

In the last part of this dissertation we derive a lower bound for quantum Fisher information using the previously constructed correlators, and we affirm that many-body nonlocality is a resource for quantum metrology.

Streszczenie

Korelacje wielociałowe jako zasób dla metrologii kwantowej

Artur Niezgoda

Metrologia kwantowa to dziedzina fizyki, która wykorzystuje zjawiska kwantowe w celu zwiększenia precyzji pomiarów. W interferometrii atomowej, technice metrologii wykorzystującej atomy, granica szumu śrutowego zadaje maksymalną dokładność pomiaru przy użyciu układów klasycznie skorelowanych. Wykazano, że stany wykazujące korelacje kwantowe – takie jak splątanie – zwiększają dokładność czujników kwantowych umożliwiając precyzję wykraczającą poza standardową granicę kwantową. Z tych powodów splątanie jest użytecznym zasobem dla metrologii kwantowej. Wśród układów najsilniej splątanych występuje zjawisko zwane nielokalnością, które jest przedmiotem intensywnych badań od kilkudziesięciu lat. Stany nielokalnie skorelowane są również przedmiotem zainteresowania naukowego z perspektywy metrologii kwantowej.

Zaczynamy od pokazania tego, że prążki interferencyjne będące wynikiem interferencji dwóch kondensatów Bosego-Einsteina można wykorzystać do wykrycia korelacji Bella w układach kwantowych. W naszej analizie uwzględniamy różne źródła szumu występujące w typowych eksperymentach.

W kolejnym kroku badamy układy kondensatów Bosego-Einsteina w konfiguracjach dwu- i trój-modowych, w których stany splątane przydatne w metrologii kwantowej są generowane poprzez dynamikę zadaną Hamiltonianem. Prezentujemy schemat pozwalający na ultra-precyzyjne pomiary, które nasycają kwantową granicę Craméra-Rao.

Następnie wyprowadzamy korelator, który wykrywa korelacje wielociałowe z pojedynczego elementu macierzy gęstości. Ponadto pokazujemy, że taki obiekt, odpowiednio przeanalizowany, dostarcza informacji o stopniu wielociałowego splątania i nielokalności. Nasze odkrycia ilustrujemy dostępnymi eksperymentalnie oddziałującymi łańcuchami spinowymi.

W ostatniej części niniejszej rozprawy, przy użyciu wcześniej skonstruowanych korelatorów, wyprowadzamy dolną granicę dla kwantowej informacji Fishera i stwierdzamy, że wielociałowa nielokalność jest zasobem metrologii kwantowej.

Acknowledgements

Firstly and above all others, I thank dr hab. Jan Chwedeńczuk for guiding me during the last 6 years. His dedication and brilliance have been an inspiration for me, and I am most grateful for all the wisdom he has imparted.

Secondly, I wish to thank dr hab. Emilia Witkowska for including me in her team at the Institute of Physics of The Polish Academy of Sciences since 2017. I cherish our fruitful discussions advancing scientific research, as well as her intellectual acuity and personal kindness.

Special thanks to Augusto Smerzi and Luca Pezzé for their guidance in realizing my Erasmus Internship and also to Marco Gabbrielli for welcoming me to Florence, Italy – a turning point in my personal and professional life.

I want to acknowledge Tomasz and Gabriela Wasak for their great hospitality in Dresden, and for Tomasz's and Francesco Piazza's counsel in Germany.

Chciałbym także podziękować moim rodzicom, Annie i Grzegorzowi, oraz bratu Radosławowi za wsparcie i pomoc na każdym etapie mojego życia.

In addition to my parents, brother, many cousins, especially Szymon, I would also like to thank Alicja, Jacek, Maciek, Magda and many others for their encouragement, friendship and joyful memories in Poland.

Finally, I would like to thank a very special person in my life, Steven Pico, for igniting my interest in international culture and art. Through Steven I have learned to respect all the valiant individuals world-wide who fight to defend and advance academic freedom, social equality, freedom of thought and freedom of expression.

Contents

Dedicated to Steven

Introduction

"The most exciting phrase to hear in science, the one that heralds new discoveries, is not 'Eureka!' (I found it!) but 'That's funny....' "

Isaac Asimov

By the end of 19th Century it was believed that physics had come to the point where the most important laws had already been discovered. In the early 1900s, however, many doubts were raised as theoretical descriptions of some physical phenomena based on fundamental laws led to absurd conclusions when applied to special cases. These single incompatibilities would soon inspire a few great thinkers to lead the world of physics into the modern era.

The first significant steps toward developing a new theory were undertaken when Max Planck proposed an explanation of black-body radiation by assuming that electromagnetic energy could be emitted only in quantized form. Planck's approach explained experimental observations very well, though the meaning of quanta remained a purely formal assumption. In 1905, in one of his Annus mirabilis papers [1], Albert Einstein proposed a simple description of photons, the quanta of light, that would explain the experimental data of the photoelectric effect. This revolution started a process that culminated in the formulation of a consistent quantum theory describing physical phenomena on the atomic level. The development of quantum mechanics led to many discoveries and explained phenomena in areas where classical mechanics had failed. Within quantum mechanics lies the foundation for many modern technologies. One brilliant idea by Planck, like the domino effect, started a revolution in physics that shaped the world we know today.

Although numerous problems were solved through scientific progress in the 20th Century, many new topics and questions emerged. One great example is the connection between general relativity and quantum mechanics which, despite many years of exploration, has not yet been established. Equipped with powerful computers and algorithms, today's scientists continue to search for signs of new physics that will illuminate a pathway into a new era. Even entanglement, which allows for measurements with precision beyond classical limits and is a main resource in quantum metrology, remains a bit of a mystery nowadays. Although a handful of interpretations of quantum mechanics have fostered debate regarding the effect of entanglement on the measured system, collective agreement exists that entanglement produces correlations between measurement outcomes which are exploited in many branches of quantum information, such as quantum cryptography, quantum computing and, most significantly from our perspective, quantum interferometry. There is one type of correlations to which special attention has been devoted – nonlocality – and research in this area has led to advanced applications in quantum theory and computing [2].

One main focus of this dissertation is to explore a class of entangled states useful for quantum metrology in commonly-used experimental setups. We devote a special interest to the strongest type of quantum correlations, namely Bell's nonlocality, providing new methods of its detection. At the end of this work we establish a link between

the presence of nonlocality and quantum metrology. Although as scientists, we are aware that only a few individuals will be remembered through the ages for their great breakthroughs, we hope that through our research we will build on previous successes and advance discoveries as we approach the next turning point in the history of physics.

This dissertation is structured in the following way:

- Chapter 1 is devoted to the concept of quantum correlations. We discuss the historical events that led to the formation of the Bell theorem and then provide a condition that allows us to distinguish entangled states. One of the Bell inequalities is derived and then we demonstrate that, in some special cases, this inequality can be violated – signaling the nonlocal character of quantum theory.

- We introduce in Chapter 2 the basic concepts of quantum metrology. We present how information about some unknown parameter θ encoded in a system can be estimated using the tools of statistical mechanics. We derive a bound for the precision of any unbiased estimator, introducing Fisher information, and we show that its optimization over all possible measurements, called the quantum Fisher information (QFI), sets the ultimate bound for the precision of the estimation process. Finally, we discuss the relation between Fisher information and entanglement, introducing a criterion for useful states for sub-shot noise interferometry.

- In Chapter 3 we present a method for detecting Bell correlations from the interference pattern formed by two overlapping Bose-Einstein condensates. We show the relation between Bell witness and the precision of the phase estimation through a fit of the one-body density to the interference pattern. We illustrate our results for the bosonic Josephson junction in the presence of experimental imperfections such as finite temperature, energy imbalance of the wells, limited detection resolution and fluctuations of the atom number.

- We discuss the generation of entangled states useful for quantum metrology in spin-1/2 and spin-1 Bose-Einstein condensates in Chapter 4. We quantify entanglement using the QFI and present optimal generators for interferometric transformation. We show that the inverse of the error propagation formula for parity measurement saturates the QFI, enabling precision at the Heisenberg level.

- In Chapter 5 we introduce a correlator, allowing us to extract the information about many-body entanglement and nonlocality from the single element of the density matrix. We present our results with examples of the one-dimensional Ising model and XXZ spin chain.

- Finally, in Chapter 6, we derive a lower bound of the QFI in the language of the Bell correlators introduced in Chapter 5. The results presented here allow us to establish a link between metrology and many-body nonlocality. We apply our results to a one-dimensional Ising model and a Bose-Einstein condenstate in a double-well potential.

The results included in this dissertation are based on the research published in the following papers:

1. Artur Niezgoda, Jan Chwedeńczuk, Luca Pezzé, and Augusto Smerzi, *Detection of Bell correlations at finite temperature from matter-wave interference fringes,* Phys. Rev. A 99, 062115 (2019);

2. Artur Niezgoda, Miłosz Panfil, and Jan Chwedeńczuk, *Characterizing quantum correlations in spin chains*, Phys. Rev. A 102, 042206 (2020);

3. Artur Niezgoda, Emilia Witkowska, and Safoura Sadat Mirkhalaf, *Twist-and-store entanglement in bimodal and spin-1 Bose-Einstein condensates*, Phys. Rev. A 102, 053315 (2020); and

4. Artur Niezgoda, Jan Chwedeńczuk, *Many-body nonlocality as a resource for quantum-enhanced metrology*, arXiv:2011.06612 (2020).

Other publications:

1. Artur Niezgoda, Dariusz Kajtoch, Emilia Witkowska, *Efficient two-mode interferometers with spinor Bose-Einstein condensates*, Phys. Rev. A 98, 013610 (2018);

2. Artur Niezgoda, Dariusz Kajtoch, Joanna Dziekańska, Emilia Witkowska, *Optimal atomic interferometry robust to detection noise using spin-1 atomic condensates*, New J. Phys. 21, 093037 (2019); and

3. Artur Niezgoda, Jan Chwedeńczuk, Tomasz Wasak, Francesco Piazza, *Cooperatively-enhanced precision of hybrid light-matter sensors*, arXiv:2007.13649 (2020).

Chapter 1

Quantum Correlations

In this chapter we discuss some of the most prominent consequences of quantum correlations. Firstly, we present a short insight in the "EPR paradox" [3] that led to the introduction of the postulates of local realism and the subsequent formulation of Bell inequalities [4]. In the second step we provide a condition for separability of quantum states, which allows us to distinguish states with a special type of correlations, i.e. the entanglement. Finally, we derive one of the Bell inequalities based on a simple hypothetical experiment involving two spatially-separated systems. We show that some special entangled states are able to violate this inequality, signaling the nonlocal character of quantum theory.

Contents

In 1932, John von Neumann outlined the basics of nonrelativistic quantum mechanics [5]. Albert Einstein, Boris Podolsky and Nathan Rosen (EPR) [3] pointed out a problem nowadays referred to as the "EPR paradox": in correlated two-particle systems, the outcome of the measurement on one particle can be determined by performing a proper measurement on the other particle. Assuming that the measurement on the second particle does not affect the first one – in the sense that no superluminal (faster-than-light) communication is allowed – Einstein, Podolsky and Rosen stated that the outcomes must be ascribed to physical quantities prior to measurement, thus implying that quantum theory should be expanded by adding extra "hidden variables" that would be crucial when predicting the measurement outcomes.

In the 1935 EPR paper, the three physicists considered the predictions for measurements of position and momentum. After 15 years, in 1950, David Bohm simplified the EPR experiment by considering discrete measurements of spin-1/2 particles [6] instead of the continuous range of the outcomes for position and momentum. We will simplify this hypothetical experiment even further by considering measurements of photon polarizations, which are closely related to Bohm's experiment. Since photons are massless particles, the spin definition of massive particles is irrelevant, as there is no rest frame for moving with speed-of-light photons [7]. However, the polarization of the light is generally accepted as its spin angular momentum, since this corresponds to helicity, the projection of the spin operator onto the momentum operator. The two possible values of helicity, $+\hbar$ and $-\hbar$, coincide with horizontal and vertical polarization of a photon, which can be determined by using a polarizing filter. The photon will either pass through or be absorbed by the ideal filter with a certain orientation, and the probability of such event may be calculated using simple linear optics.

Imagine that two photons are traveling apart from each other in the same direction, prepared in the so-called "twin state" polarization. The term twin state means

that these two photons, when measured using identical polarizing filters, will always produce the same result. In quantum mechanics this state is defined by an entangled isotropic state of the form:

$$|\Psi\rangle = \frac{1}{\sqrt{2}} \left(|x\rangle_1 \otimes |x\rangle_2 + |y\rangle_1 \otimes |y\rangle_2 \right), \tag{1.1}$$

where $|x\rangle_i$ ($|y\rangle_i$) represents a polarization state of the i-th photon that is guaranteed to pass through a horizontal (vertical) filter and be absorbed by a vertical (horizontal) filter. To measure polarization of both photons we use identical polarizing filters oriented at the same angle. If the first photon passes through then, from the form of the state in Eq. (1.1), we are assured that the second one will pass as well. Also, if the first photon is absorbed, then it is guaranteed that the second photon will share the same fate. Therefore, the outcomes are perfectly correlated.

Since the measurement of the polarization on the second photon can be determined by measuring the polarization of the first photon, the authors of the EPR paper suggested that the polarization of the second photon is a well-defined observable. Since the measurement on the first photon did not affect the other photon, the outcome of the measurement must have been decided even before any measurement was performed. Therefore they introduced an "element of reality" existing in the second photon – that would provide information about the polarization – while performing a measurement on the first photon.

In contrast, quantum mechanics states that the poralizations of the photons are not precisely defined before the measurements take place. The form of the state in Eq. (1.1) indicates the existence of correlations between both photons, but neither has a well-defined individual polarization. Einstein, Podolsky and Rosen argued, that quantum mechanics cannot specify an element of reality responsible for measurement outcomes. The uncertainties that emerged in quantum theory are a result of neglecting such elements and consequently quantum mechanical theory is incomplete. Their hypothesis assumed that the system of the second photon knew all about the first photon long before any measurement was performed. Such "elements of reality", referred to later as "hidden variables", would also be local in the sense that "spooky action" at a distance could be excluded. The conclusion found in the EPR paper was used as an assumption in the local hidden variable model, formalized by John Stewart Bell in 1964 [4], which provides constraints on the set of inequalities on statistical correlations for bipartite systems. Violation of any of these inequalities would signal that an assumption of the existence of such local "elements of reality" is incorrect.

In the following sections we will provide a mathematical description of quantum correlations, starting with the condition for determining whether the state is entangled or characterized by classical correlations.

1.1 Entangled Quantum Systems

The nonclassical aspect of entanglement was first recognized in 1935 by Erwin Schrödinger. Inspired by the EPR paper [3], Schrödinger noticed that the two-particle EPR state cannot be written as a product of the states of each particle. This phenomenon is still of importance in 21st Century physics, since it can be now produced in various systems, e.g. photons [8–10], trapped ions [11, 12] and other massive particles [13–16]. Entanglement is exploited in tests of the fundamentals of quantum mechanics such as the Hong-Ou-Mandel effect [8, 17, 18], ghost imaging [9, 19, 20], the sub-Poissonian atom number fluctuations [21] or the violation of the Cauchy-Schwarz

inequality [22–24]. Therefore, it is important to translate Schrödinger's conclusion into mathematical language.

In order to determine if the quantum state is entangled, we begin by specifying which states are not entangled. This can be decided by using a simple condition of separability. Let us consider a quantum system composed of two subsystems, namely A and B. If the pure state of that system cannot be expressed as the product of both subsystems, i.e.

$$|\Psi\rangle_{AB} = |\varphi\rangle_A \otimes |\phi\rangle_B, \tag{1.2}$$

where $|\varphi\rangle_A$ ($|\phi\rangle_B$) describes subsystem A (B), then the state is entangled [25]. Analogically, the mixed state is entangled if its density matrix cannot be expressed as

$$\hat{\varrho}_{AB} = \sum_i p_i \hat{\varrho}_A^{(i)} \otimes \hat{\varrho}_B^{(i)}, \tag{1.3}$$

where $\hat{\varrho}_{A,B}$ are local density matrices of particles A and B, $p_i > 0$ and $\sum_i p_i = 1$. The states described by formulas given in Eq. (1.2) or (1.3) are called separable (or not entangled) and are characterized by classical correlations, established via local operations [26], like mixing the product states. For $N = 2$, the quantum state is either entangled or separable, but when $N > 2$ further classification is necessary [27, 28]. A state of fully separable N particles has the form

$$|\Psi\rangle = |\psi^{(1)}\rangle \otimes |\psi^{(2)}\rangle \otimes ... \otimes |\psi^{(N)}\rangle \tag{1.4a}$$

$$\hat{\varrho}_{sep} = \sum_k p_k |\Psi_k\rangle\langle\Psi_k|, \tag{1.4b}$$

where $|\psi^{(i)}\rangle$ is a state of the i-th particle and $\sum_k p_k = 1$. A multiparticle state is then entangled if, for at least two qubits, the reduced two-qubit density matrix is entangled. The number of entangled particles is quantified by the so-called entanglement depth, which is defined by the largest number of non-separable qubits. For example, a quantum state is i-separable if it can be written in the form of a mixture of i-producible pure states [29]:

$$|\Psi_{i-prod}\rangle = |\psi_1\rangle \otimes |\psi_2\rangle \otimes ... \otimes |\psi_m\rangle \tag{1.5a}$$

$$\hat{\varrho}_{i-sep} = \sum_k p_k |\Psi_{i-prod,k}\rangle\langle\Psi_{i-prod,k}|, \tag{1.5b}$$

where $|\psi_j\rangle$ is a state of maximum i particles and $m \geq N/i$ holds. The quantum state is i-particle entangled if it is i-separable but not $(i-1)$-separable. In other words, a state is i-particle entangled if the correlations cannot be explained assuming entanglement between $i-1$ particles.

Strongly entangled states can manifest other phenomena such as steerability (or EPR-steering), for which the entanglement is a necessary but insufficient condition [30]. Let us consider a pure state of two systems, held by two distant observers, Alice and Bob,

$$|\Psi\rangle = \sum_{n=1}^{\infty} c_n |u_n\rangle|\psi_n\rangle = \sum_{n=1}^{\infty} d_n |v_n\rangle|\varphi_n\rangle, \tag{1.6}$$

where $\{|u_n\rangle\}$ and $\{|v_n\rangle\}$ ($\{|\psi_n\rangle\}$ and $\{|\varphi_n\rangle\}$) are two orthonormal bases of Alice's

(Bob's) system. The existence of such states implies that if Alice performs measurement in the basis $\{|u_n\rangle\}$ then Bob's system collapses into one of the states $\{|\psi_n\rangle\}$, analogically for the other basis. Therefore Alice can "steer" Bob's system, despite the separation and the fact that both systems no longer interact. One of the consequences of this phenomenon is that Alice's measurement can increase the precision of Bob's measurement on his system [31–33].

Nevertheless, certain steerable states can exhibit even stronger correlations between parties, namely Bell correlations. A common feature of this class of states is nonlocality, which requires both the presence of entanglement and steerability in the system. In the next section we will derive the condition for observing Bell correlations in the given system.

1.2 Bell Nonlocality

Bell's theorem is one of the most important scientific discoveries, representing a remarkable contribution to our understanding of physics. In his paper [4], Bell showed that a theory satisfying locality constraints and realism is, in general, in contradiction to quantum theory. Over the past 50 years, nonlocality of quantum theory has become the subject of intensive studies. We will now provide a mathematical description of a locality constraint for experiments involving two separate systems. We will derive one of the Bell inequalities and show that, in some special cases, quantum theory predicts its violation, thus signalling nonlocality.

Let us consider two systems that may have interacted in the past – for example, they could have been produced by the same source. In our experiment, these two systems are now space-like separated and can be measured by one of the two distant observers, Alice and Bob. Both independently choose measurements on their system. We denote Alice's and Bob's choice by x and y, respectively, and the outcomes of performed measurements on the two systems by a and b. It is natural to expect that the outcomes a and b may vary from shot to shot, even if the same measurements x and y are performed. In general the results of the experiment are governed by a probability distribution $p(ab|xy)$ and for correlated outcomes of measurements it holds

$$p(ab|xy) \neq p(a|x)p(b|y). \tag{1.7}$$

The expectation, using local theory, is that the correlations between the measurements do not result from the effect of the direct influence of one system on the other, especially if they are space-like separated, but were rather established during their interaction in the past. Their communication is not prohibited; however, we assume that the measurement is performed before any information from the second system is transferred. For example, we can assume a situation where the two systems A (Alice's) and B (Bob's) are separated, see Fig. 1.1, and at a given moment, indicated by the RNG symbol, both observers choose a random basis for their measurements. As indicated by the measurement symbol, these measurements are completed before any information about the basis choice from the other system has been transferred with the speed of light (colored regions). This means that there should exist some past factors that have joint influence on the outcomes of the measurements and are responsible for the dependence between a and b. Such factors can be described by some variables λ, and modify the probability distribution in Eq. (1.7) in a way that the probabilities for obtaining the results a and b should now factorize

$$p(ab|xy,\lambda) = p(a|x,\lambda)p(b|y,\lambda). \tag{1.8}$$

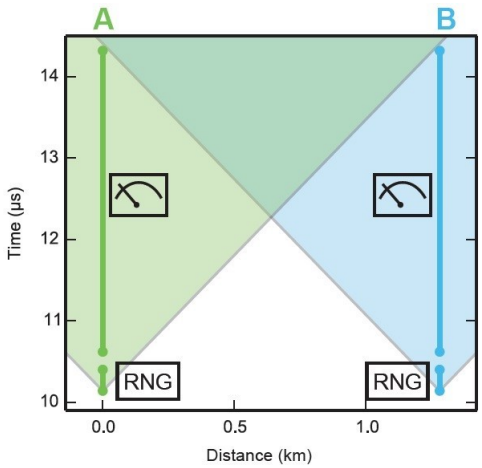

Figure 1.1: Space-time diagram of the Bell test from [34]. The x-axis denotes distance between the measurements performed at location A and B, and the y-axis is time scale starting at $10\mu s$. We can assume that preparation of the system takes place in the first $10\mu s$. At the moment indicated by the RNG symbol, the setups at A and B choose a random basis. The readout on each side, indicated by the measurement symbol, is completed before any information about the basis choice from the other side can be transferred with the speed of light (colored regions). Such an experimental setup ensures that neither of the measurements has any immediate effect in the space-separated regions.

The probability of the outcome a (b) depends now only on the past variables λ and the choice of the local measurement x (y), but not on the measurement performed on the distant system. In general, λ will also vary in each run of the experiment, even with the fixed preparation procedure. Thus, the range of values of λ is described by a probability distribution $q(\lambda)$, which also assumes that the measurement choices x and y are independent of λ. The result we get

$$p(ab|xy) = \int_{\Lambda} d\lambda q(\lambda) p(a|x,\lambda) p(b|y,\lambda) \tag{1.9}$$

represents a precise condition for locality, without assumptions of determinism or classicality and with no restrictions on the physical laws. The index Λ indicates integration over a complete set of hidden variables. If Eq. (1.9) can explain correlations between two distant particles, then events in one region of space-time should not have any impact on events in spacelike separated regions.

One can, however, design an experiment involving entangled particles that cannot be explained assuming the decomposition given in Eq. (1.9). For simplicity we consider an experiment with only two measurement choices for each of the observers $x, y \in \{0, 1\}$ for which possible outcomes are labeled $a, b \in \{-1, +1\}$. The expectation value of the product ab for given measurements choices x and y is then

$$E(a_x, b_y) = \sum_{a,b} ab\, p(ab|xy). \tag{1.10}$$

Let's consider an expression

$$S = E(a_0, b_0) + E(a_1, b_0) + E(a_0, b_1) - E(a_1, b_1) \tag{1.11}$$

which is a function of probabilities $p(ab|xy)$. Using Eq. (1.9) in the definition of $E(a_x, b_y)$ we can rewrite this average as an expectation value

$$E(a_x, b_y) = \sum_{a,b} \int_\Lambda d\lambda q(\lambda) A_x(\lambda) B_y(\lambda) \tag{1.12}$$

of a product of local averages $A_x(\lambda) = \sum_a ap(a|x,\lambda)$ and $B_y(\lambda) = \sum_b bp(b|y,\lambda)$ taking values from $[-1,1]$. Inserting Eq. (1.12) into Eq. (1.11), we got $S = \int_\Lambda d\lambda q(\lambda)\mathcal{S}(\lambda)$, where

$$\mathcal{S}(\lambda) = A_0(\lambda)B_0(\lambda) + A_0(\lambda)B_1(\lambda) + A_1(\lambda)B_0(\lambda) - A_1(\lambda)B_1(\lambda). \tag{1.13}$$

Since we have $A_0(\lambda), A_1(\lambda) \in [-1,1]$, the expression (1.13) is limited from above

$$\mathcal{S}(\lambda) \leq |B_0(\lambda) + B_1(\lambda)| + |B_0(\lambda) - B_1(\lambda)|, \tag{1.14}$$

which assuming, without loss of generality, that $B_0(\lambda) \geq B_0(\lambda) \geq 0$ yields the upper bound for $\mathcal{S}(\lambda) \leq 2$ and in consequence

$$|S| \leq 2. \tag{1.15}$$

Combining expression (1.11) with the limitation in Eq. (1.15), we arrive at

$$S = |E(a_0,b_0) + E(a_1,b_0) + E(a_0,b_1) - E(a_1,b_1)| \leq 2, \tag{1.16}$$

known as the Clauser-Horne-Shimony-Holt (CHSH) inequality [35]. It is one of the Bell inequalities verified by any model satisfying the locality condition given in Eq. (1.9), but violated by performing proper measurements on the entangled state.

Let us consider an experiment in which the two systems measured by Bob and Alice are two qubits in the singlet state

$$|\Psi^-\rangle = \frac{1}{\sqrt{2}} \left(|\uparrow\rangle_1 \otimes |\downarrow\rangle_2 - |\downarrow\rangle_1 \otimes |\uparrow\rangle_2 \right), \tag{1.17}$$

where $|\uparrow\rangle$ and $|\downarrow\rangle$ are the eigenstates of the spin projection in z-direction with the eigenvalues ± 1, respectively. The measurement choices x and y are associated with vectors $\vec{x}$, $\vec{y}$ corresponding to Alice's measurement $\vec{x}\cdot\vec{\sigma}$ on the first qubit and Bob's $\vec{y}\cdot\vec{\sigma}$ on the second, where $\vec{\sigma} = \{\vec{\sigma}_1, \vec{\sigma}_2, \vec{\sigma}_3\}$ is Pauli vector. The expectation value is then

$$E(a_x, b_y) = \langle\Psi^-|(\vec{x}\cdot\vec{\sigma})^{(A)}(\vec{y}\cdot\vec{\sigma})^{(B)}|\Psi^-\rangle = -\vec{x}\cdot\vec{y}. \tag{1.18}$$

Now if the two settings of measurements $x \in \{0,1\}$ correspond to measurements in the orthogonal directions $\hat{e}_1$ and $\hat{e}_2$ and the settings $y \in \{0,1\}$ to directions $-(\hat{e}_1+\hat{e}_2)/\sqrt{2}$ and $(-\hat{e}_1+\hat{e}_2)/\sqrt{2}$, then we arrive at $E(a_0,b_0) = E(a_1,b_0) = E(a_0,b_1) = 1/\sqrt{2}$ and $E(a_1,b_1) = -1/\sqrt{2}$. The result is $S = 2\sqrt{2} > 2$ which is a violation of inequality (1.15) and thus the locality constraint in Eq. (1.9).

Since 1972, the violation of the Bell inequality has been confirmed in many experiments involving photons [36–43], ions in a Paul trap [44], solid state spins [45], Josephson phase qubits [46] and even many-body systems such as Bose-Einstein condensates [47].

The main foci of this thesis explore new methods for detecting Bell correlations in quantum systems, and the link between the presence of Bell's nonlocality and

quantum metrology. Therefore, in the following chapter we will introduce the basics of estimation theory in order to provide a short introduction to the world of precise measurements.

Chapter 2

Estimation Theory

In this chapter we introduce some basic concepts of quantum metrology. We consider a system whose properties depend on some unknown parameter θ. Estimation theory sets its goal to deduce the value of θ with the highest possible precision. We derive a bound for the uncertainty of any unbiased estimator using the Fisher information and then show that it can be saturated asymptotically in the special case of the maximum likelihood estimator. We present an alternative method of estimation based on the first and the second moments, and conclude that the uncertainty is a lower bound for the Fisher information. Additionally we derive the upper bound, called the quantum Fisher information. Finally, we show that entangled states can enhance the precision of the estimation beyond the classical limit and therefore entanglement is a resource for quantum metrology.

Contents

Every day using common devices we perform countless measurements, some of which can be appraised simply and directly, such as distance, using standardized apparatus. Performing other measurements requires more complicated processes. For example, in order to find velocity of an object we have to measure its displacement during the time period when the change of position occurred. The precision of such a process depends on the uncertainty of both the distance measurement and the clock. Generally speaking, the more complicated the process of measurement is, the more factors affecting the precision of the results. Although one may think that on an everyday basis we should be satisfied with relatively low precision, the demand for exceptionally precise measurements is growing in numerous widely-available technologies, such as global positioning systems which require highly precise atomic clocks [48–50]. In order to reach a desirable level of precision we have to dive into the world of atoms and molecules, where the laws of classical physics no longer work and quantum mechanics is required to provide a correct description of the measurement process.

Therefore, we must adapt our tools to be able to perform highly precise measurements on the quantum systems. For example, to measure the temperature of an object we usually bring it to the equilibrium with a thermometer and then read out the temperature. However, if we use ultra-cold gases, such a procedure is no longer possible because, due to the fragility of the system, it needs to be isolated from

any macroscopic environment. Alternatively, we may use the methods of statistical mechanics to estimate the temperature from the measurements of the momentum or spatial profile of the gas. We now take a closer look at the tools of estimation theory.

2.1 Estimators

We assume that some properties of a system depend on a parameter θ. This parameter can be associated, e.g. with the position of a particle x, its mass m, or for quantum systems a relative phase between two sub-systems. The goal of estimation procedure is to find the value of that parameter with the highest possible precision. In order to do so properly, we need to perform a measurement x, the outcome of which depends strongly on θ, i.e. $x(\theta)$. Now let us consider a situation, where m measurements of x were performed in one experimental sequence. Based on the results, we build an estimator Θ that provides the value of the parameter θ:

$$\theta_E^{(i)} = \Theta(x_1^{(i)}, x_2^{(i)}, ..., x_m^{(i)}), \tag{2.1}$$

where the superscript i indicates an i-th experimental sequence. In practice the results x_j will fluctuate from shot to shot. Thus in order to find the estimation error we have to repeat the experimental sequence multiple times. After M repetitions we arrive with the set of estimated values $\Theta^{(1)}, \Theta^{(2)}, ..., \Theta^{(M)}$ which can be used to plot the histogram of $\Theta^{(i)}$(Fig. 2.1) and estimate the unknown parameter θ using for example the mean value of this distribution:

$$\langle\Theta\rangle = \frac{1}{M}\sum_{i=1}^{M}\theta_E^{(i)}. \tag{2.2}$$

In general, averaging can be performed over all possible values of the measurement x_j using joined probability distribution of these values $P(x_1, x_2, ..., x_m|\theta)$, which conditionally depends on the true value of the unknown parameter. The average in Eq. (2.2) takes the form:

$$\langle\Theta\rangle = \int dx_1...dx_m\Theta(x_1, ..., x_m)P(x_1, ..., x_m|\theta). \tag{2.3}$$

Since the estimator is a function of fluctuating outcomes, we expect that some estimators are better than others. In general we would like our estimator to have a minimal variance

$$\Delta^2\Theta \equiv \int d\vec{x}\,(\Theta(\vec{x}) - \theta)^2\,P(\vec{x}|\theta), \tag{2.4}$$

where $\vec{x} = (x_1, ..., x_m)$. But since we could choose an estimator to be a constant function $\langle\Theta(\vec{x})\rangle = \theta_0$, which with a pinch of luck could be equal to the true value $\theta_0 = \theta$ and therefor have zero uncertainty, we need a condition that eliminates cases such as this. Thus we can consider estimators that satisfy the unbiasedness condition

$$\langle\Theta\rangle = \theta, \tag{2.5}$$

which means that on average the estimator gives the true value for all values of θ. In practice, we may find that an optimal estimator for the whole range of parameter θ does not exist. Therefore, generally we consider estimators that are asymptotically

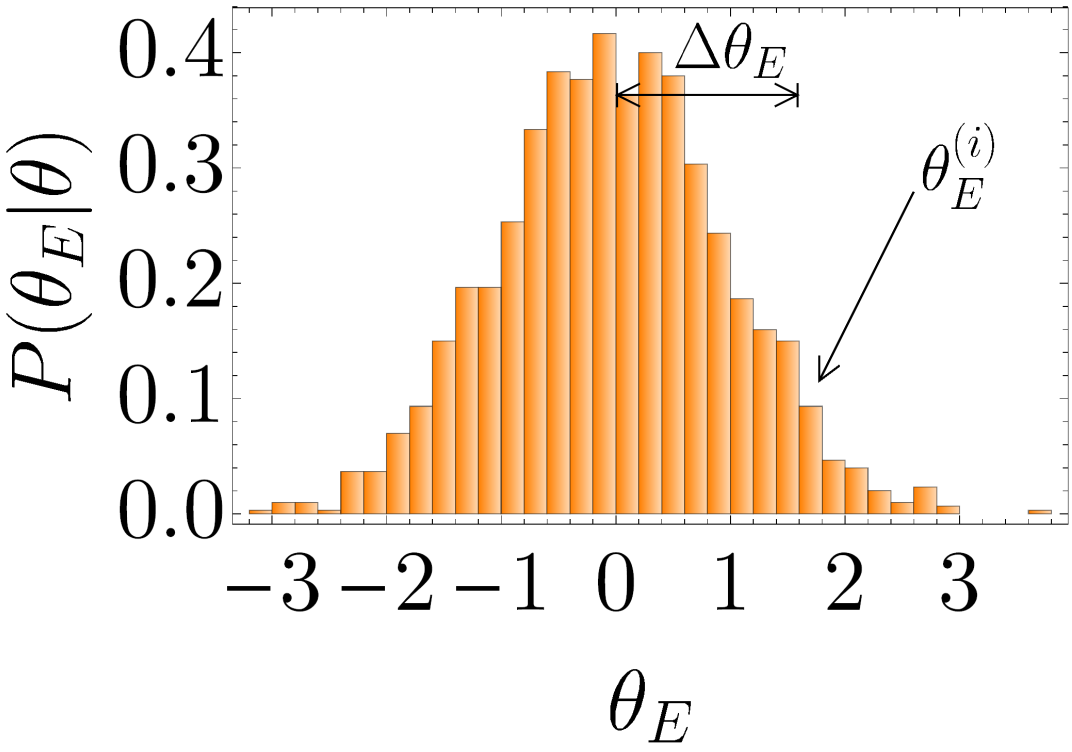

Figure 2.1: An example of a histogram for Θ with m = 2000. The estimated value of the unknown parameter is the mean value $\langle\Theta\rangle$ of the histogram, whilst the precision is given by the width of the distribution. For $m \to \infty$ the histogram resembles normal distribution as a consequence of the central limit theorem.

unbiased, i.e. an average value tends to the true value of the parameter θ for $m \to \infty$:

$$\lim_{m\to\infty} \langle\Theta\rangle = \theta. \tag{2.6}$$

Additionally, an optimal estimator would have to be consistent – meaning that, with an increasing number of measurements, the probability that that estimator will give results closer to the true value θ will increase as well

$$\lim_{m\to\infty} \Theta(x_1^{(i)}, ..., x_m^{(i)}) = \theta \text{ for all } i. \tag{2.7}$$

In other words, as the sample size increases, the distribution of the estimator will concentrate at the true value of the parameter θ.

We have presented here conditions that have to be satisfied in order to choose an optimal estimator. In addition we would like to minimize the variance in Eq. (2.4), which requires knowledge of all possible estimators. In practice it is much easier to proceed using another criterion, so, in the next section, we will derive a lower bound of the variance for any unbiased estimator – the Cramér-Rao bound – that can be used to determine useful estimators.

2.2 The Cramér-Rao Bound

The Cramér-Rao bound was developed independently through the work of Cramér [51], Rao [52], and Frechet [53], who found a lower bound to the variance of any arbitrary estimator. For an unbiased estimator and m independent measurements, the Cramér-Rao bound reads

$$\Delta\Theta \geqslant \Delta\theta_{CRB} = \frac{1}{\sqrt{\mathcal{I}_m(\theta)}}, \tag{2.8}$$

where

$$\mathcal{I}_m(\theta) = \int d\vec{x} \frac{1}{P(\vec{x}|\theta)} \left(\frac{\partial P(\vec{x}|\theta)}{\partial \theta} \right) \tag{2.9}$$

is the Fisher information [54, 55] and m stands for x_m measurements in the joined probability distribution $P(x_1, x_2, ..., x_m|\theta)$.

To derive the Cramér-Rao bound we start with the assumption that the estimator is unbiased, see Eq. (2.5), for which the following condition is satisfied

$$\frac{d\langle\Theta\rangle}{d\theta} = \int d\vec{x}\Theta(\vec{x}) \frac{dP(\vec{x}|\theta)}{d\theta} = 1, \tag{2.10}$$

while the probability function is regular

$$\int d\vec{x} \frac{dP(\vec{x}|\theta)}{d\theta} = \frac{d}{d\theta} \int d\vec{x} P(\vec{x}|\theta) = 0. \tag{2.11}$$

Rewriting Eq. (2.3) under the unbiasedness condition, we obtain

$$\int d\vec{x}(\Theta(\vec{x}) - \theta) P(\vec{x}|\theta) = 0. \tag{2.12}$$

A derivative of Eq. (2.12) with respect to θ, based on Eqs. (2.10) and (2.11), gives

$$\int d\vec{x}(\Theta(\vec{x}) - \theta) \frac{dP(\vec{x}|\theta)}{d\theta} = 1. \tag{2.13}$$

Then, using the Cauchy-Schwarz inequality stating that for two functions $f(\vec{x})$ and $g(\vec{x})$ the following condition is satisfied

$$\left| \int d\vec{x} f(\vec{x}) g(\vec{x}) \right|^2 \leqslant \int d\vec{x} \left| f(\vec{x}) \right|^2 \int d\vec{x} \left| g(\vec{x}) \right|^2, \tag{2.14}$$

with $f(\vec{x}) = \frac{1}{\sqrt{P(\vec{x}|\theta)}} \frac{\partial P(\vec{x}|\theta)}{\partial \theta}$ and $g(x) = \sqrt{P(\vec{x}|\theta)}(\Theta(\vec{x}) - \theta)$, we arrive at the final inequality

$$\int d\vec{x} \left(\Theta(\vec{x}) - \theta \right)^2 P(\vec{x}|\theta) \int d\vec{x} \frac{1}{P(\vec{x}|\theta)} \left(\frac{\partial P(\vec{x}|\theta)}{\partial \theta} \right)^2 \geqslant 1, \tag{2.15}$$

where we can recognize the variance of the estimator from Eq. (2.4) in the first part and the Fisher information from Eq. (2.9) in the second part. In the case where $x_1, ..., x_m$ are the same, single and independent measurements, the joint probability

simplifies $P(\vec{x}|\theta) = \prod_{j=1}^{m} p(x_j|\theta)$ and so the Fisher information takes a form

$$\mathcal{I}_m(\theta) = m \int dx \frac{1}{p(x|\theta)} \left(\frac{\partial p(x|\theta)}{\partial \theta} \right) = m\mathcal{I}(\theta). \tag{2.16}$$

As the result, the Cramér-Rao bound now reads

$$\Delta\Theta \geqslant \frac{1}{\sqrt{m\mathcal{I}(\theta)}}, \tag{2.17}$$

where the factor $\frac{1}{m}$ is a consequence of the additivity of the Fisher information. In addition to the expression in Eq. (2.16), Fisher information can be also calculated from the following expressions:

$$\mathcal{I}(\theta) = \left\langle \left(\frac{d}{d\theta} \log \left(P(\vec{x}|\theta) \right) \right)^2 \right\rangle \tag{2.18}$$

$$\mathcal{I}(\theta) = - \left\langle \frac{d^2}{d\theta^2} \log \left(P(\vec{x}|\theta) \right) \right\rangle. \tag{2.19}$$

If Eq. (2.17) is saturated then the estimator is optimal and moreover it is called efficient. The saturation of the Cramér-Rao bound is equivalent to the saturation of the Cauchy-Schwarz inequality (2.14), hence the condition

$$\frac{1}{\sqrt{P(\vec{x}|\theta)}} \frac{\partial P(\vec{x}|\theta)}{\partial \theta} = \alpha(\theta) \sqrt{P(\vec{x}|\theta)} (\Theta - \theta). \tag{2.20}$$

The above equation can be solved analytically with a Gaussian probability distribution

$$P(\vec{x}|\theta) = \prod_{i=1}^{N} \frac{1}{\sqrt{2\pi\sigma^2}} e^{-\frac{(x_i-\theta)^2}{2\sigma^2}}, \tag{2.21}$$

with $\Theta(\vec{x}) = \sum_{i=1}^{N} \frac{x_i}{N}$ and $\alpha(\theta) = \frac{N}{\sigma^2}$. The result implies that if the probability in the estimator is Gaussian, it saturates the Cramér-Rao bound. Although we never know if the saturating estimator exists, there is one estimator that always asymptotically saturates the Cramér-Rao bound – which will we prove in the following section.

2.3 Maximum Likelihood Estimator

As mentioned previously, we never know if the estimator that saturates Eq. (2.17) exists, unless the probability $P(\vec{x}|\theta)$ is Gaussian. Fortunately we can always build the Maximum Likelihood Estimator (MLE) that saturates the Cramér-Rao bound asymptotically.

We establish such estimator by assuming that x is measured m times, and the probability of the outcome $p(x|\theta)$ is known. We construct the following likelihood function

$$\mathcal{L}(\varphi) = \log \left(\prod_{j=1}^{m} p(x_j|\varphi) \right), \tag{2.22}$$

which is the function of variable φ with the other variables fixed by the measurement outcomes. The estimator is now defined with the value of φ for which $\mathcal{L}$ is maximized

$$\Theta_{MLE}^{(m)}: \qquad \left.\frac{\partial \mathcal{L}(\varphi)}{\partial \varphi}\right|_{\varphi=\Theta_{MLE}^{m}} = 0. \tag{2.23}$$

In other words, if we put the true value of the parameter in Θ_{MLE}, then the probability to observe x_j would be the highest. The asymptotic efficiency of the MLE plays the essential role in the parameter estimation, meaning that the MLE saturates the Cramér-Rao bound for a large number of identical and independent measurements. In order to prove this, first we show that the MLE is consistent. We calculate the difference between Eq. (2.22) and the likelihood function with the true value of the parameter θ as follows:

$$\mathcal{L}(\varphi) - \mathcal{L}(\theta) = \sum_{j=1}^{m} \log\left(\frac{p(x_j|\varphi)}{p(x_j|\theta)}\right) \xrightarrow{m\to\infty} m \int dx p(x|\theta) \log\left(\frac{p(x|\varphi)}{p(x|\theta)}\right). \tag{2.24}$$

We bound the result from above using the expression $\log(\beta) \leqslant \beta - 1$ and obtain

$$m \int dx p(x|\theta) \log\left(\frac{p(x|\varphi)}{p(x|\theta)}\right) \leqslant m \int dx p(x|\theta) \left(\frac{p(x|\varphi)}{p(x|\theta)} - 1\right) = 0. \tag{2.25}$$

The last expression is bounded by 0 for $p(x|\varphi) = p(x|\theta)$, hence $\varphi = \theta$. Therefore the MLE is consistent in the limit $m \to \infty$, i.e.

$$\lim_{m\to\infty} \Theta_{MLE}^{(m)} = \theta. \tag{2.26}$$

To prove asymptotic unbiasedness we start with a calculation of the derivative of the likelihood function from Eq. (2.22) with respect to φ and expand it in the Taylor series around the true value θ

$$\mathcal{L}'(\varphi) = \mathcal{L}'(\theta) + \mathcal{L}''(\theta)(\varphi - \theta) + ... \tag{2.27}$$

If we choose $\varphi = \Theta_{MLE}^{m}$ then by definition we have $\mathcal{L}'(\Theta_{MLE}^{m}) = 0$. Assuming $m \gg 1$ we use the consistency of MLE and thus we can neglect the higher order terms. As a result we obtain

$$\Theta_{MLE}^{m} - \theta \simeq -\frac{\mathcal{L}'(\theta)}{\mathcal{L}''(\theta)}. \tag{2.28}$$

The second derivative of the likelihood function from Eq. (2.22) has a form

$$\mathcal{L}''(\theta) = \sum_{i=1}^{m} \left[-\frac{1}{p(x_i|\theta)^2} \left(\left.\frac{\partial p(x_i|\varphi)}{\partial \varphi}\right|_{\varphi=\theta} \right)^2 + \frac{1}{p(x_i|\theta)} \left.\frac{\partial^2 p(x_i|\varphi)}{\partial \varphi^2}\right|_{\varphi=\theta} \right], \tag{2.29}$$

for which the summation can be replaced with an integral by averaging with the probability $p(x|\theta)$ under the condition $m \to \infty$:

$$\mathcal{L}''(\theta) \xrightarrow{m\to\infty} m \int dx \left[-\frac{1}{p(x|\theta)} \left(\left.\frac{\partial p(x|\varphi)}{\partial \varphi}\right|_{\varphi=\theta} \right)^2 + \left.\frac{\partial^2 p(x|\varphi)}{\partial \varphi^2}\right|_{\varphi=\theta} \right]. \tag{2.30}$$

The second expression in the parenthesis of Eq. (2.30) vanishes, and the remaining part

is equal to $-m\mathcal{I}(\theta)$. By implementing the result into the denominator of Eq. (2.28), we obtain

$$\Theta_{MLE}^{(m)} - \theta \simeq \frac{1}{m}\sum_{i=1}^{m}\left[\frac{1}{\mathcal{I}(\theta)}\frac{1}{p(x_i|\theta)}\frac{\partial p(x_i|\theta)}{\partial\varphi}\bigg|_{\varphi=\theta}\right]. \tag{2.31}$$

Now we can see that the object on the right-hand side of Eq. (2.31) is an average of m random variables in the square bracket. The Central Limit Theorem [56] states that with $m \to \infty$ the probability distribution of the object tends to Gaussian distribution, so the mean value of the object on the left-hand side can be calulated as follows:

$$\begin{aligned}\left\langle\Theta_{MLE}^{(m)} - \theta\right\rangle &\xrightarrow{m\to\infty} \int dx p(x|\theta)\left[\frac{1}{\mathcal{I}(\theta)}\frac{1}{p(x|\theta)}\frac{\partial p(x|\theta)}{\partial\varphi}\bigg|_{\varphi=\theta}\right] = \\ &= \frac{1}{\mathcal{I}(\theta)}\int dx\frac{\partial p(x|\theta)}{\partial\varphi}\bigg|_{\varphi=\theta} = 0.\end{aligned} \tag{2.32}$$

The last expression proves that the MLE is unbiased. The final step is to show that the MLE saturates the Cramér-Rao bound. Based on Eq. (2.32), we can calculate the variance of the estimator

$$\begin{aligned}\Delta^2\Theta_{MLE}^{m} &\xrightarrow{m\to\infty} \frac{1}{m}\int dx p(x|\theta)\left[\frac{1}{\mathcal{I}(\theta)}\frac{1}{p(x|\theta)}\frac{\partial p(x|\theta)}{\partial\varphi}\bigg|_{\varphi=\theta}\right]^2 = \\ &= \frac{1}{m}\frac{1}{\mathcal{I}(\theta)^2}\int dx\frac{1}{p(x|\theta)}\left(\frac{\partial p(x|\theta)}{\partial\varphi}\bigg|_{\varphi=\theta}\right)^2 = \frac{1}{m}\frac{1}{\mathcal{I}(\theta)}.\end{aligned} \tag{2.33}$$

This proves that the MLE is an asymptotically efficient estimator. Although the MLE requires a priori knowledge of $P(\vec{x}|\theta)$ for the complete domain of θ and the set of the measurement outcomes $\vec{x}$, it has been used in several experiments [57–61]. There are also alternative methods to estimate the unknown parameter θ. In the next section we present an estimation from the method of moments.

2.4 The Method of Moments

The method of moments takes advantage of collective properties of the probability distribution such as the mean value $\bar{x}$ and variance $\Delta^2 x$, but may be used as long as $\bar{x}$ is a monotonous function of parameter θ. The expectation value $\bar{x}$ over m measurement results $x_1, ..., x_m$, where $x_i \equiv x_i(\theta)$, is given with

$$\bar{x}_m = \frac{1}{m}\sum_{j=1}^{m} x_j. \tag{2.34}$$

The expected value of the estimator of the method of moments Θ_{mom} will then be the value for which $\bar{x} = \bar{x}_m$. This method requires the average value $\bar{x}$ to be a monotonous function of the parameter θ. Therefore, applying the Taylor expansion of $\bar{x}_m$ around the true value θ yields

$$\bar{x}_m \approx \bar{x} + \frac{d\bar{x}}{d\theta}(\Theta_{\text{mom}} - \theta). \tag{2.35}$$

By identifying $\bar{x}_m - \bar{x} \approx \Delta x/\sqrt{m}$ and $\Theta_{\text{mom}} - \theta \approx \Delta\theta_{\text{mom}}$ we obtain

$$\Delta\theta_{\text{mom}} = \frac{\Delta x}{|\sqrt{m}\frac{d\bar{x}}{d\theta}|}. \tag{2.36}$$

The uncertainty obtained using the method of moments is the lower bound to the Fisher information [62], i.e.

$$\mathcal{I}(\theta) \geqslant \frac{\left(\frac{\partial\bar{x}}{d\theta}\right)^2}{\Delta^2 x}, \tag{2.37}$$

so, in other words, the Fisher information is more sensitive to the change of the parameter θ than the average moments of probability distribution. One may then ask if the upper bound can be derived. The answer is positive, and we will go through the process in the following section.

2.5 The Ultimate Bound

For quantum systems probability is expressed in the language of the Positive-Operator Valued Measures $\hat{\Pi}_x$ – positive semi-definite matrices that sum up to the identity matrix

$$\sum_x \hat{\Pi}_x = \hat{\mathbb{1}} \text{ or } \int dx\, \hat{\Pi}_x = \hat{\mathbb{1}}. \tag{2.38}$$

Using these operators, the probability of obtaining the outcome x when measured on the system described with density matrix $\hat{\rho}_\theta \equiv \hat{\rho}(\theta)$ has the form

$$p(x|\theta) = \text{Tr}\left[\hat{\Pi}_x\hat{\rho}_\theta\right]. \tag{2.39}$$

The quantum estimation scheme requires us to find not only an optimal estimator but also an optimal measurement for our system; besides that, it resembles the classical procedure. Therefore, first we will derive the quantum Cramér-Rao bound. Classical Fisher information, defined in Eq. (2.9), can be rewritten using the definition of probability given in Eq. (2.39) as follows:

$$\mathcal{I}_\theta = \int dx \frac{1}{\text{Tr}\left[\hat{\Pi}_x\hat{\rho}_\theta\right]}\left(\frac{\partial\text{Tr}\left[\hat{\Pi}_x\hat{\rho}_\theta\right]}{\partial\theta}\right)^2 = \int dx \frac{1}{\text{Tr}\left[\hat{\Pi}_x\hat{\rho}_\theta\right]}\left(\text{Tr}\left[\hat{\Pi}_x\frac{\partial\hat{\rho}_\theta}{\partial\theta}\right]\right)^2. \tag{2.40}$$

Let us denote that the derivative of the density matrix is given with

$$\frac{\partial\hat{\rho}_\theta}{\partial\theta} = \frac{1}{2}\left[\hat{L}_\theta\hat{\rho}_\theta + \hat{\rho}_\theta\hat{L}_\theta\right], \tag{2.41}$$

where $\hat{L}_\theta$ is a θ-dependent operator called the symmetric logarithmic derivative (SLD) [63]. In eigenbasis of $\hat{\rho}_\theta$, i.e. $\hat{\rho}_\theta = \sum_i p_i|i\rangle\langle i|$, where $p_i \equiv p_i(\theta), p_i \geqslant 0$ and $\sum_i p_i = 1$, we have

$$\langle i|\frac{\partial\hat{\rho}_\theta}{\partial\theta}|j\rangle = \frac{1}{2}\left(p_i\langle i|\hat{L}_\theta|j\rangle + \langle i|\hat{L}_\theta|j\rangle p_j\right), \tag{2.42}$$

hence

$$\langle i|\hat{L}_\theta|j\rangle = \frac{2}{p_i + p_j}\langle i|\frac{\partial\hat{\rho}_\theta}{\partial\theta}|j\rangle. \tag{2.43}$$

We now take the enumerator of Eq. (2.40) and based on the Hermitian properties of $\hat{\rho}_\theta, \hat{L}_\theta$ and $\hat{\Pi}_x$ we obtain

$$\begin{aligned}\mathrm{Tr}\left[\hat{\Pi}_x\frac{1}{2}\left(\hat{L}_\theta\hat{\rho}_\theta + \hat{\rho}_\theta\hat{L}_\theta\right)\right] &= \mathrm{Tr}\left[\frac{1}{2}\left(\hat{\Pi}_x\hat{L}_\theta\hat{\rho}_\theta + \left(\hat{\Pi}_x\hat{L}_\theta\hat{\rho}_\theta\right)^\dagger\right)\right] = \\ &= \mathrm{Re}\left(\mathrm{Tr}\left[\hat{\Pi}_x\hat{L}_\theta\hat{\rho}_\theta\right]\right) \leqslant \mathrm{Tr}\left[\hat{\Pi}_x\hat{L}_\theta\hat{\rho}_\theta\right].\end{aligned} \tag{2.44}$$

This expression is saturated if the imaginary part is equal to zero, i.e. $\mathrm{Im}\left(\mathrm{Tr}\left[\hat{\Pi}_x\hat{L}_\theta\hat{\rho}_\theta\right]\right) = 0$. Using the Cauchy-Schwarz inequality with respect to the Hilbert-Schmidt matrix scalar product $|\mathrm{Tr}\left[AB^\dagger\right]|^2 \leqslant \mathrm{Tr}\left[A^\dagger A\right]\mathrm{Tr}\left[B^\dagger B\right]$, where we set $A = \sqrt{\hat{\Pi}_x\hat{\rho}_\theta}$ and $B = \sqrt{\hat{\Pi}_x\hat{L}_\theta\hat{\rho}_\theta}$, we arrive at

$$|\mathrm{Tr}\left[\hat{\Pi}_x\hat{L}_\theta\hat{\rho}_\theta\right]|^2 \leqslant \mathrm{Tr}\left[\hat{\Pi}_x\hat{\rho}_\theta\right]\mathrm{Tr}\left[\hat{L}_\theta\hat{\Pi}_x\hat{L}_\theta\hat{\rho}_\theta\right]. \tag{2.45}$$

Then, by substituting the above inequality into Eq. (2.40), we obtain an inequality

$$\mathcal{I}(\theta) \leqslant \int dx \mathrm{Tr}\left[\hat{L}_\theta\hat{\Pi}_x\hat{L}_\theta\hat{\rho}_\theta\right] = \mathrm{Tr}\left[\hat{L}_\theta^2\hat{\rho}_\theta\right] \equiv F_Q(\hat{\rho}_\theta), \tag{2.46}$$

where $F_Q(\hat{\rho}_\theta)$ is quantum Fisher information, fully determined by the output state $\hat{\rho}_\theta$. In fact, the quantum Fisher information is Fisher information maximized over all measurements [64], thus the condition $\mathcal{I}(\theta) \leqslant F_Q$ always holds. With this new result, we can set a corresponding bound on the estimation for unbiased estimators with m independent measurements, called the quantum Cramér-Rao bound [63] which reads

$$\Delta\Theta_{CR} \geqslant \Delta\Theta_{QCR} = \frac{1}{\sqrt{mF_Q(\hat{\rho}_\theta)}}. \tag{2.47}$$

To simplify the expression of quantum Fisher information, we can calculate the trace in Eq. (2.46), i.e.

$$F_Q(\hat{\rho}_\theta) = \mathrm{Tr}\left[\hat{L}_\theta^2\hat{\rho}_\theta\right] = \sum_{i,j}\frac{p_i + p_j}{2}|\langle i|\hat{L}_\theta|j\rangle|^2. \tag{2.48}$$

The average value of the SLD operator is given with Eq. (2.43) for $p_i + p_j \neq 0$, therefore we obtain

$$F_Q(\hat{\rho}_\theta) = \sum_{i,j}\frac{2}{p_i + p_j}|\langle i|\frac{\partial\hat{\rho}_\theta}{\partial\theta}|j\rangle|^2. \tag{2.49}$$

Finally we have to calculate the derivative of the density matrix

$$\partial_\theta\hat{\rho}_\theta = \sum_k(\partial_\theta p_k)|k\rangle\langle k| + \sum_k p_k\left(|\partial_\theta k\rangle\langle k| + |k\rangle\langle\partial_\theta k|\right), \tag{2.50}$$

whose elements take the following form

$$\langle i|\partial_\theta \hat{\rho}_\theta|j\rangle = \partial_\theta p_i \delta_{ij} + p_i\langle \partial_\theta i|j\rangle + p_j\langle i|\partial_\theta j\rangle. \tag{2.51}$$

Using the identity $\partial_\theta\langle i|j\rangle = \langle\partial_\theta i|j\rangle + \langle i|\partial_\theta j\rangle = 0$ we obtain

$$\langle i|\partial_\theta \hat{\rho}_\theta|j\rangle = \partial_\theta p_i \delta_{ij} + p_i\langle \partial_\theta i|j\rangle - p_j\langle \partial_\theta i|j\rangle \tag{2.52}$$

and by implementing it into the Eq. (2.49), we arrive at a simple formula for the quantum Fisher information

$$\begin{aligned} F_Q(\hat{\rho}_\theta) &= \sum_{i,j} \frac{2}{p_i + p_j} |\partial_\theta p_i \delta_{i,j} + (p_i - p_j)\langle \partial_\theta i|j\rangle|^2 = \\ &= \sum_i \frac{(\partial_\theta p_i)^2}{p_i} + 2\sum_{i,j} \frac{(p_i - p_j)^2}{p_i + p_j} |\langle \partial_\theta i|j\rangle|^2. \end{aligned} \tag{2.53}$$

Let us now consider a scenario where the information of the parameter θ is imprinted on the quantum system in the initial state, described with density matrix $\hat{\rho}_{in}$, through some unitary transformation

$$\hat{\rho}_{in} \to \hat{\rho}_\theta = e^{-i\theta\hat{h}} \hat{\rho}_{in} e^{i\theta\hat{h}}, \tag{2.54}$$

where $\hat{h}$ is generator of the evolution. Therefore, since the eigenvalues do not change, the formula for the quantum Fisher information is of the following form

$$F_Q(\hat{\rho}_\theta) = 2\sum_{i,j} \frac{(p_i - p_j)^2}{p_i + p_j} |\langle i|\hat{h}|j\rangle|^2 \tag{2.55}$$

with the condition $p_i + p_j > 0$ [64, 65]. For the special case of pure states, e.g. $\hat{\rho}_\theta = |\Psi(\theta)\rangle\langle\Psi(\theta)|$, the quantum Fisher information reduces to

$$F_Q(\Psi(\theta)) = 4\left(\langle \partial_\theta\Psi(\theta)|\partial_\theta\Psi(\theta)\rangle - |\langle \partial_\theta\Psi(\theta)|\Psi(\theta)\rangle|^2\right), \tag{2.56}$$

which for unitary transformation is equal to

$$F_Q(\Psi(\theta)) = 4\left(\langle\Psi_0|\hat{h}^2|\Psi_0\rangle - |\langle\Psi_0|\hat{h}|\Psi_0\rangle|^2\right) = 4\Delta^2\hat{h}. \tag{2.57}$$

Note that here the quantum Fisher information does not depend on θ, due to commutation between $\hat{h}$ and $e^{\pm i\theta\hat{h}}$. In general, if the unitary transformation has a more complicated form, for example $U(\theta) = e^{-i(\hat{A}\theta + \hat{B})}$, then the generator of evolution is calculated according to

$$\hat{h} = (\partial_\theta \hat{U}(\theta))\hat{U}^\dagger(\theta). \tag{2.58}$$

In general, the quantum Fisher information is limited by

$$F_Q(\Psi(\theta)) \leqslant 4\Delta^2\hat{h}, \tag{2.59}$$

which is saturated for the pure states. Inequality (2.59) provides a powerful tool for distinguishing metrologically useful states from the point of view of the parameter estimation. Before we demonstrate this tool, we want to focus our attention on the two-mode quantum interferometry.

The two-mode quantum interferometer is a device that imprints a relative phase θ between the two modes. Such an operation can be represented by a unitary transformation of the form

$$U(\theta) = e^{-i\theta \hat{J}_{\vec{n}}}. \tag{2.60}$$

Here $\hat{J}_{\vec{n}}$ consists of angular momentum operators $\{\hat{J}_x, \hat{J}_y, \hat{J}_z\}$ forming Lie algebra with commutation relation $[\hat{J}_i, \hat{J}_j] = i\varepsilon_{ijk}\hat{J}_k$. In the case of two-mode interferometer the operators can be defined as a sum of Pauli matrices acting on each particle independently

$$\hat{J}_k = \frac{1}{2}\sum_i \hat{\sigma}_k^{(i)}. \tag{2.61}$$

Eq. (2.60) corresponds to the rotation, for which the direction $\vec{n}$ can be optimized in order to maximize the quantum Fisher information ([66] and reference therein). Thus we can use another definition of quantum Fisher information which depends on the input state $\hat{\rho}$ and the generator of the interferometric rotation $\hat{\Lambda}_{\vec{n}}$, which for simplicity we will refer to as an interferometer. The quantum Fisher information is then defined as [67]

$$F_Q(\hat{\rho}, \hat{\Lambda}_{\vec{n}}) = 4\vec{n}^T \cdot \Gamma(\hat{\rho}) \cdot \vec{n}, \tag{2.62}$$

where $\hat{\Lambda}_{\mathbf{n}} = \hat{\Lambda} \cdot \mathbf{n}$, $\hat{\Lambda}$ is the vector of generators spanning Lie algebra and $\vec{n}$ is a unit vector defining the interferometer. $\Gamma(\hat{\rho})$ is the covariance matrix of the form

$$\Gamma_{i,j}(\hat{\rho}) = \frac{1}{2}\sum_{k,l} \frac{(v_k - v_l)^2}{v_k + v_l} Re\left[\langle k|\hat{\Lambda}_i|l\rangle\langle l|\hat{\Lambda}_j|k\rangle\right]. \tag{2.63}$$

v_k and v_l are eigenvalues of the eigenvector $|k\rangle$ and $|l\rangle$ of the input density matrix $\hat{\rho} = \sum_k v_k|k\rangle\langle k|$ and $\hat{\Lambda}_j$ as an element of $\hat{\Lambda}_{\vec{n}}$. The dimension of the covariance matrix is equal to the squared number of generators in Lie algebra, for instance in bosonic $SU(2)$ we have 9 elements in the 3x3 covariance matrix. The maximal value of the quantum Fisher information is then given by the largest eigenvalue $\lambda_{\max}$ of the covariance matrix and the generator of the optimal interferometric rotation is determined by the corresponding eigenvector. The choice of direction of $\hat{\Lambda}_n$ strongly influences the presision of the measurement.

2.5.1 Physical Interpretation of the Fisher Information

Estimation of the unknown parameter is related to the statistical distance between neighboring quantum states [64]. The precision of phase estimation for an interferometer is associated with the smallest phase shift for which two states $\hat{\rho}_{in}$ and $\hat{\rho}_{d\theta}$ can be distinguished. For this reason it is justified to introduce a statistical difference

$$d_H^2(P_0, P_{d\theta}) = 1 - \mathcal{F}_{cl}(P_0, P_{d\theta}), \tag{2.64}$$

called the Hellinger distance [68], where $\mathcal{F}_{cl}(P_0, P_{d\theta}) = \sum_x \sqrt{p(x|0)p(x|d\theta)}$ is the overlap of probability distributions called fidelity. The Taylor expansion of d_H around $\theta = 0$, i.e.

$$d_H^2(P_0, P_{d\theta}) = \frac{\mathcal{I}(0)}{8} d\theta^2 + \mathcal{O}(d\theta^3) \tag{2.65}$$

shows that the Fisher information can be identified with the statistical speed

$$v_H = \frac{\partial d_H}{\partial \theta} = \sqrt{\mathcal{I}(0)/8}, \tag{2.66}$$

which measures how the probability distribution varies with the shift of the parameter θ. Since the Fisher information depends on the measurement choice, we can maximize the Hellinger distance over all possible observables, namely Bures distance [69]

$$d_B(\hat{\rho}_0, \hat{\rho}_{d\theta}) = \max_{\hat{\Pi}_x} d_H(P_0, P_{d\theta}), \tag{2.67}$$

which reads [70]

$$d_B^2(\hat{\rho}_0, \hat{\rho}_{d\theta}) = 1 - \mathcal{F}_Q(\hat{\rho}_0, \hat{\rho}_{d\theta}), \tag{2.68}$$

where $\hat{\rho}_{d\theta} = e^{-id\theta\hat{\Lambda}_n}\hat{\rho}_0 e^{id\theta\hat{\Lambda}_n}$ and the quantum fidelity between two states $\mathcal{F}_Q(\hat{\rho}_0, \hat{\rho}_{d\theta})$ has a form

$$\mathcal{F}_Q(\hat{\rho}_0, \hat{\rho}_{d\theta}) = \sqrt{\sqrt{\hat{\rho}_{d\theta}}\hat{\rho}_0\sqrt{\hat{\rho}_{d\theta}}}. \tag{2.69}$$

As in Eq. (2.64), d_B can also be expanded into Taylor series around $\theta = 0$ giving

$$d_B^2 = \frac{F_Q(\hat{\rho}_0, \hat{\Lambda}_n)}{8} d\theta^2 + \mathcal{O}(\theta^3). \tag{2.70}$$

Thus the quantum Fisher can also be identified with the square of a quantum statistical speed

$$v_B = \frac{\partial d_B}{\partial \theta} = \sqrt{\mathcal{F}_Q(\hat{\rho}_0, \hat{\Lambda}_n)/8}. \tag{2.71}$$

This means that input states $\hat{\rho}_0$ for which quantum Fisher information has high value are sensitive to optimal interferometric rotation $\hat{\Lambda}_n$, in the way that even a small change of parameter θ allows us to distinguish $\hat{\rho}_{d\theta}$ from the initial state (see Fig. 2.2). Therefore, it increases the precision of the estimation the of parameter θ.

2.6 States Useful for Quantum Metrology

In Chapter 1 we discussed the nonclassical effects manifesting with entanglement. In this section we prove that entangled states can enhance precision in estimation procedure over the best achievable sensititvity obtained using nonentangled states.

In order to derive a mathematical bound that allows one to indentify states that provide high precision, we assume a unitary transformation $U(\theta)$ represented by a linear interferometer that does not entangle particles in the system itself, i.e.

$$\hat{\varrho}_{sep}^{in} \xrightarrow{\hat{U}(\theta)} \hat{\varrho}_{sep}^{out}(\theta), \tag{2.72}$$

where $\hat{\varrho}_{sep}^{in}$ is a separable state of N particles. This can be realized, for example, if the generator of the evolution is given with the angular momentum operator defined as in Eq. (2.61). Consequently the transformation does not correlate particles, and

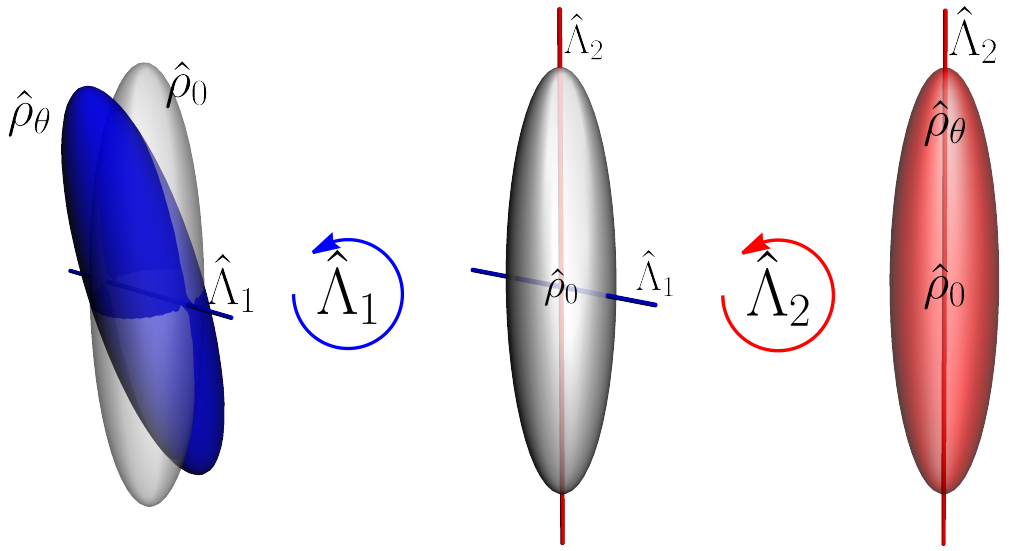

Figure 2.2: An example of interferometric rotation of the initial state $\hat{\rho}_0$ (gray cigar shape). The output state produced by interferometer given by $\hat{\Lambda}_1$ (blue cigar shape) is distinguishable from the input state $\hat{\rho}_0$, consequently the quantum system is sensitive to the shift of the parameter θ. Alternatively, if the direction is not optimal, for example $\hat{\Lambda}_2$, the states will be indistinguishable and estimation of the parameter θ will no longer be possible. The blue solid line and red solid line present the rotation axis for $\hat{\Lambda}_1$ and $\hat{\Lambda}_2$, respectively.

the unitary transformation can be rewritten in the form

$$\hat{U}(\theta) = \prod_{i=1}^{N} \hat{U}^{(i)}(\theta). \tag{2.73}$$

Previously, we showed that the precision of estimation parameter θ imprinted by the interferometer is bounded by quantum Fisher information, i.e. $\Delta\theta \propto 1/\sqrt{F_q}$. Moreover, with a choice of generator $\hat{h} = \vec{n} \cdot \vec{\hat{J}} = \hat{J}_{\vec{n}}$, from the inequality (2.59) we get

$$F_Q \leqslant 4 \left\langle \Delta^2 \hat{J}_{\vec{n}} \right\rangle. \tag{2.74}$$

For a separable state of a form (1.4a), using the definition in Eq. (2.61), we can show that

$$\begin{aligned} F_Q \leqslant 4 \left\langle \Delta^2 \hat{J}_{\vec{n}} \right\rangle &= \left\langle \left(\sum_i \hat{\sigma}_k^{(i)} \right)^2 \right\rangle - \left\langle \frac{1}{2} \sum_i \hat{\sigma}_k^{(i)} \right\rangle^2 = \\ &= N - \left(\left\langle \frac{1}{2} \sum_i \hat{\sigma}_k^{(i)} \right\rangle^2 - \sum_{i \neq j} \left\langle \hat{\sigma}_n^{(i)} \right\rangle \left\langle \hat{\sigma}_n^{(j)} \right\rangle \right) = \\ &= N - \left\langle \frac{1}{2} \sum_i \hat{\sigma}_k^{(i)} \right\rangle^2 \leqslant N. \end{aligned} \tag{2.75}$$

The above result shows that the sensitivity of the interferometer for nonentangled states is bounded by the so-called shot-noise limit or standard quantum limit

$$\Delta\theta_{est} \geqslant \frac{1}{\sqrt{m}\sqrt{N}}. \tag{2.76}$$

In general, we see that

$$F_Q \leqslant 4\left\langle \Delta^2 \hat{J}_{\vec{n}} \right\rangle \leqslant \left\langle \left(\sum_i \hat{\sigma}_k^{(i)} \right)^2 \right\rangle \leqslant N^2, \tag{2.77}$$

which provides the upper bound for the precision: the so-called Heisenberg limit

$$\Delta\theta_{est} \geqslant \frac{1}{\sqrt{m}} \frac{1}{N}. \tag{2.78}$$

By combining both Eqs. (2.76) and (2.78), the uncertainty of the estimation in range

$$\frac{1}{\sqrt{m}\sqrt{N}} > \Delta\theta_{est} \geqslant \frac{1}{\sqrt{m}} \frac{1}{N} \tag{2.79}$$

requires $F_Q > N$ and, in consequence, the entangled input state in the interferometer. This shows that entanglement is a necessary resource for precision beyond the standard quantum limit [62, 71].

In this chapter we covered the basics of estimation theory, an essential part of quantum metrology. We derived a bound for the classical process of estimation, and proved that entangled states are crucial in the process of ultra precise measurements. In the next chapter we will present a method for detecting Bell correlations based on the interference pattern formed by two overlaping Bose-Einstein condensates and we will make a first atempt towards establishing a relation between the Bell nonlocality and metrology.

Chapter 3

Bose-Einstein Condensate in a Double Well

In this chapter we present a method for detection of Bell correlations using the fit of the one-body density function to the interference pattern, formed by two overlapping Bose-Einstein condensates, with the relative phase as a free parameter. Part of this study was originally a subject of my Secondary Degree Thesis [72]. However, it was greatly expanded during my PhD studies [73], and published as a research paper. These extensive results justify inclusion as part of a PhD thesis.

To begin we introduce the scheme of the Josephson junction in Bose-Einstein condensates. In the next step we bring in the concept of squeezing to classify the ground states for both attractive and repulsive interactions in the model. Then, we introduce a method of phase estimation from the interference pattern and connect it to the Bell witness, signaling the presence of the Bell correlations in the system. Finally, we illustrate the efficiency of such witness in the presence of the experimental imperfections: finite temperature, energy imbalance of the wells, limited detection resolution and atom number fluctuations.

Contents

Bose-Einstein condensate (BEC) is an exotic form of matter, created for the first time in 1995 by Carl Wieman and Eric Cornell's group at the University of Colorado at Boulder [74]. Shortly thereafter Wolfgang Ketterle reported the successful creation of BEC with hundreds times more atoms than his precursors, allowing him to perform spectacular measurements of the properties of the condensate such as interference of two separate condensate clouds [75]. These achievements started a new era of scientific exploration, bringing novel ways to test the foundations of quantum theory. The system of ultra-cold atoms can be used, for example, to study the Josephson effect [76] by confining a single BEC in a double-well potential [77].

A bosonic Josephson junction (BJJ) consists of two localized matter wave packets weakly coupled by the tunneling of particles through the barrier due to a chemical potential gradient. The BEC is confined in a double-well potential

$$V_{dw} = \frac{1}{2}M(\omega_x^2 x^2 + \omega_y^2 y^2 + \omega_z^2 z^2) + V_0 \cos^2\left(\frac{\pi x}{d}\right), \tag{3.1}$$

which contains three-dimensional harmonic confinement characterized by the three trapping frequencies $\omega_{x,y,z}$ and one-dimensional periodic potential of a height V_0 and a periodicity of d acting as the barrier. Parameter M stands for atomic mass. Due to weak coupling to the environment the quantum description of this system can be simplified using a two-mode approximation. Therefore, a bosonic field operator is given with

$$\hat{\Psi}(\mathbf{r},t) = \psi_a(\mathbf{r},t)\hat{a} + \psi_b(\mathbf{r},t)\hat{b}, \tag{3.2}$$

where $\hat{a}$ and $\hat{b}$ annihilate a particle in the left and right well, respectively, and $\psi_{a,b}$ are the ground state single-particle wave functions generated by the external potential in both wells. The wave functions ψ_a and ψ_b are not orthogonal, i.e. $\int d\mathbf{r}\psi_j^*(\mathbf{r},t)\psi_k(\mathbf{r},t) = \delta_{jk} + \epsilon(1-\delta_{jk})$ for $j,k = a,b$, where ϵ is the overlap between the modes of opposite wells. However, since $\epsilon \ll 1$, the overlap can be neglected and the local modes can be treated as orthogonal [78]. Thus, with the normalization condition $\int d\mathbf{r} \left\langle \hat{\Psi}^\dagger(\mathbf{r},t)\hat{\Psi}(\mathbf{r},t) \right\rangle = \left\langle \hat{a}^\dagger\hat{a} + \hat{b}^\dagger\hat{b} \right\rangle = N$, where N is the total number of particles, the two-mode approximation of the BJJ Hamiltonian is given by

$$\hat{H} = \hbar\chi\hat{J}_z^2 - \hbar\Omega\hat{J}_x + \hbar\delta\hat{J}_z, \tag{3.3}$$

where χ and Ω are the strength of interactions and the coupling parameters, respectively, and $\hbar\delta$ is the energy difference between the wells. The parameters χ and Ω can be controlled precisely in the experiment, while δ can change from shot to shot. To this end, we assume $\Omega \geqslant 0$ without loss of generality. The first operator in Hamiltonian (3.3), $\hat{J}_z^2$, describes intaractions between atoms, $\hat{J}_x$ accounts for the linear coupling between the wells and $\hat{J}_z$ stands for the energy imbalance between both sites. For the N-body system of bosons in two modes, the angular momentum operators in Hamiltonian (3.3) can be mapped on a system of spin-$1/2$, where the two modes of BJJ, namely $|a\rangle$ corresponding to the left well and $|b\rangle$ to the right well, can be identified with two spin states $+1/2$ and $-1/2$ [78]. Thus, the collective angular momentum operators, defined previously with Pauli matrices (see Eq. (2.61)), can be rewritten in terms of the creation and annihilation operators acting in each mode, in so-called Schwinger representation [79], as follows:

$$\hat{J}_x = \frac{1}{2}\left(\hat{a}^\dagger\hat{b} + \hat{b}^\dagger\hat{a}\right), \tag{3.4a}$$

$$\hat{J}_y = \frac{1}{2i}\left(\hat{a}^\dagger\hat{b} - \hat{b}^\dagger\hat{a}\right), \tag{3.4b}$$

$$\hat{J}_z = \frac{1}{2}\left(\hat{a}^\dagger\hat{a} - \hat{b}^\dagger\hat{b}\right). \tag{3.4c}$$

The BEC trapped in the double-well potential is an example of the external BJJ. If the barrier is high enough, the ground state and the first excited state are almost degenerated and separated from higher energy levels of potential. The two-mode approximation is valid even if the weak interactions are included. In the case of the external junction, the parameters in Hamiltonian (3.3) are identified as [78, 80, 81]

$$\hbar\Omega = |E_b - E_a|, \tag{3.5a}$$

$$\hbar\chi = \frac{8\pi\hbar^2 a_s}{M}\int d\mathbf{r}|\psi_a(\mathbf{r},t)|^2|\psi_b(\mathbf{r},t)|^2, \tag{3.5b}$$

where E_a and E_b are the energies of the modes a and b, M is the atomic mass and

a_s is the s-wave scattering length positive for repulsive interactions and negative for attractive interactions.

Another possible realization of a BJJ can be achieved with a trapped BEC in two different hyperfine states. The coupling is produced by an electromagnetic field that coherently transfers atoms between two states via Rabi rotations [82, 83]. In the internal BJJ the cross-interaction term, involving the overlap of two different atomic-species orbitals $\psi_{a,b}(\mathbf{r},t)$ cannot be neglected, since both species are confined in the same harmonic potential. The many-body Hamiltonian is given by Eq. (3.3) with coefficients of the following form

$$\hbar\Omega = \Omega_R \int d\mathbf{r}\psi_a^*(\mathbf{r},t)\psi_b(\mathbf{r},t), \tag{3.6a}$$

$$\hbar\chi = U_{aa} + U_{bb} - 2U_{ab}, \tag{3.6b}$$

$$U_{ij} = \frac{2\pi\hbar^2 a_s^{(i,j)}}{M} \int d\mathbf{r}|\psi_a(\mathbf{r},t)|^2|\psi_b(\mathbf{r},t)|^2, \tag{3.6c}$$

where Ω_R is the Rabi frequency and $a_s^{(a,a)}, a_s^{(b,b)}, a_s^{(a,b)}$ are intra-species and inter-species s-wave scattering lengths. In the internal BJJ we can assume that single particle wave functions of the two hyperfine states are the same, i.e. $\psi_a(\mathbf{r}) \simeq \psi_b(\mathbf{r})$ and effects can be neglected during Rabi coupling pulses with $\Omega \gg N\chi$.

In the next section we provide a semi-classical approach of Hamiltonian (3.3) in order to elucidate the structure of the ground states in different regimes of the interactions.

3.1 Mean-field Approximation and Beyond

In order to understand the structure of the ground states we use the mean-field approximation [84, 85]. The dynamics of the BJJ model in the classical phase space is acquired by replacing the mode operators with complex numbers as follows: $\hat{a} \to \sqrt{N_a}e^{-\phi_a}, \hat{b} \to \sqrt{N_b}e^{-\phi_b}$, where $N_{a,b}$ are the numbers of particles and $\phi_{a,b}$ the phases of the condensate in modes $|a\rangle$ and $|b\rangle$, respectively. Therefore, we replace the pseudospin operators in Eq. (3.4) with real numbers:

$$\hat{J}_x \to \frac{N}{2}\sqrt{1-z^2}\cos\phi, \tag{3.7a}$$

$$\hat{J}_y \to \frac{N}{2}\sqrt{1-z^2}\sin\phi, \tag{3.7b}$$

$$\hat{J}_z \to \frac{N}{2}z, \tag{3.7c}$$

where $\phi = \phi_a - \phi_b$ is the relative phase between modes and $z = \frac{N_a - N_b}{N}$ is the fraction of population difference. The mean-field approximation of the Hamiltonian (3.3) is then

$$H(z,\varphi) = \frac{\Lambda z^2}{2} - \sqrt{1-z^2}\cos\phi + \Xi z, \tag{3.8}$$

where the energy unit is $\frac{1}{2}N\hbar\Omega, \Lambda = N\chi/\Omega$ and $\Xi = \delta/\Omega$. From this point we focus on the case with $\delta = 0$, unless explicitly stated.

In the next step of our analysis, we use a naive procedure of quantization of the classical Hamiltonian (3.8). We expand Eq. (3.8) to the second order around the minimum point ($z = 0, \phi = 0$) and replace the conjugate number and phase variables,

z and ϕ, with operators $\hat{z}, \hat{\phi} = -\frac{2i}{N}\hat{\partial}_z$. It is important to note that the rigorous phase operator in quantum mechanics is missing, so the above process may bring notable artifacts when the phase fluctuations are large. Therefore we obtain the quantum Hamiltonian

$$\hat{H}_z = -\frac{2}{N^2}\hat{\partial}_z^2 + \frac{\Lambda+1}{2}\hat{z}^2 \tag{3.9}$$

in the number representation. If, instead, we replace $z \to \frac{2i}{N}\hat{\partial}_\phi$ and $\phi \to \hat{\phi}$, obeying the same commutation relation, we obtain the quantum Hamiltonian in a phase representation

$$\hat{H}_z = -\frac{2(\Lambda+1)}{N^2}\hat{\partial}_\phi^2 + \frac{1}{2}\hat{z}^2. \tag{3.10}$$

Hamiltonians (3.9) and (3.10) predict the Gaussian wave function for the ground state [86] when $\Lambda > -1$ with variances

$$\sigma_z^2 = \frac{1}{N\sqrt{1+\Lambda}} \text{ and } \sigma_\phi^2 = \frac{\sqrt{1+\Lambda}}{N}. \tag{3.11}$$

The potential changes at $\Lambda = -1$ and, therefore, the improvements have to be made by considering the second-order expansion of Eq. (3.8) around $\phi = 0$ and rewriting the term $\frac{1}{2}\sqrt{1-z^2}\phi^2 = \phi\frac{1}{2}\sqrt{1-z^2}\phi$. This leads to

$$\hat{H}_z = -\hat{\partial}_z\frac{2}{N^2}\sqrt{1-\hat{z}}\hat{\partial}_z + W_0(\hat{z}) \tag{3.12}$$

with

$$W_0(\hat{z}) = \frac{\Lambda\hat{z}^2}{2} - \sqrt{1-\hat{z}^2}. \tag{3.13}$$

Hamiltonian (3.12) describes a fictitious quantum particle with effective mass moving in the $z-$direction in an anharmonic one-dimensional potential W_0. The above Hamiltonian was derived by [87] using a continous approximation of the population imbalance z, and avoiding commutation relations between phase and number operators. In the analyzed case ($\Xi = 0$) the effective potential is harmonic when $\Lambda > -1$, changes to quadratic at $\Lambda = -1$ and changes to a double-well shape for $\Lambda < -1$ with the wells centered at $z_\pm = \pm\sqrt{1-1/\Lambda^2}$.

3.2 Ground States of the BJJ Model

The structure of the ground state of the BJJ Model depends strongly on the character of the interactions. When the interactions are repulsive the fluctuations in atom number between the two modes are energetically unfavorable, while the phase fluctuations are increased. However, in the case of attractive interactions, the system favors all atoms localized in one mode. For weak attractive interactions, moreover, we observe reduced phase fluctuations. Therefore it is convenient to characterize these fluctuations in the language of spin-squeezing parameter. This concept is related to entangled states for which spin variance along one direction is squeezed, at the cost of anti-squeezed variance along an orthogonal direction [88, 89]. Moreover, it is also a resource to interferometry beyond the standard quantum limit. In general, the spin-squeezing parameter can be defined in many different ways, but for the use

of this chapter we choose the one introduced by David Wineland [88]. Wineland's squeezing parameter ξ_R^2 is linked to the sensitivity of the states to the unitary rotation represented by generators $\hat{J}_{\mathbf{n}}$. The sensitivity of the phase estimation from the spin measurement along a direction $\mathbf{n}_1$ orthogonal to the rotation direction $\mathbf{n}_2$ can be calculated from the method of moments as follows:

$$\Delta^2\theta = \frac{\Delta^2 \hat{J}_{\mathbf{n}_1}}{m|\partial \left\langle \hat{J}_{\mathbf{n}_1} \right\rangle / \partial\theta|^2}, \text{ for } m \gg 1. \tag{3.14}$$

Using the Baker-Campbell-Hausdorff formula:

$$e^{\hat{X}}\hat{Y}e^{-\hat{X}} = \hat{Y} + \left[\hat{X}, \hat{Y}\right] + \frac{1}{2!}\left[\hat{X}, \left[\hat{X}, \hat{Y}\right]\right] + \frac{1}{3!}\left[\hat{X}, \left[\hat{X}, \left[\hat{X}, \hat{Y}\right]\right]\right] + ... \tag{3.15}$$

and the commutation relation $\left[\hat{J}_{\mathbf{n}_1}, \hat{J}_{\mathbf{n}_2}\right] = i\hat{J}_{\mathbf{n}_3}$, we obtain

$$\left\langle \hat{J}_{\mathbf{n}_1} \right\rangle = \left\langle e^{i\theta\hat{J}_{\mathbf{n}_2}} \hat{J}_{\mathbf{n}_1} e^{-i\theta\hat{J}_{\mathbf{n}_2}} \right\rangle_0 = \left\langle \hat{J}_{\mathbf{n}_1} \right\rangle_0 \cos\theta + \left\langle \hat{J}_{\mathbf{n}_3} \right\rangle_0 \sin\theta, \tag{3.16}$$

where subscript 0 indicates the average calculated on the state prior to the rotation. Therefore, the phase sensitivity in Eq. (3.14) for $\theta \to 0$ is

$$\Delta^2\theta = \frac{\Delta^2 \hat{J}_{\mathbf{n}_1}}{m\left|\left\langle \hat{J}_{\mathbf{n}_3} \right\rangle\right|^2}, \text{ for } m \gg 1. \tag{3.17}$$

The squeezing parameter can be defined by the condition for sub-shot noise precision

$$\xi_R^2 \equiv \frac{\Delta^2\theta}{\Delta^2\theta_{SN}} = \frac{N\Delta^2 \hat{J}_{\mathbf{n}_1}}{\left|\left\langle \hat{J}_{\mathbf{n}_3} \right\rangle\right|^2} < 1, \tag{3.18}$$

where $\Delta^2\theta_{SN} = 1/(mN)$. The state is spin-squeezed along the direction $\mathbf{n}_1$ whenever the above inequality holds, i.e. $\xi_R^2 < 1$.

Based on these results, we now determine a structure of the ground state of the Hamiltonian (3.3). First, we rewrite our Hamiltonian in the following form ($\hbar = 1$)

$$\hat{H} = \frac{\Lambda}{N}\hat{J}_z^2 - \hat{J}_x + \delta\hat{J}_z, \tag{3.19}$$

where $\Lambda = \frac{N\Omega}{\chi}$ can be negative for attractive interactions and positive for repulsive interactions, and δ is the energy imbalance between the modes.

Noninteracting System $\Lambda = 0$

When $\Lambda = 0$, no interactions are present in the system and the Hamiltonian (3.19) is reduced to $\hat{H} = -\hat{J}_x$. The ground state in this case is a coherent spin state (CSS), polarized in the positive direction of the x-axis

$$|\Psi\rangle = \frac{1}{\sqrt{N!}}\left(\frac{\hat{a}^\dagger + \hat{b}^\dagger}{\sqrt{2}}\right)^N |0,0\rangle. \tag{3.20}$$

CSS can be rewritten in the basis of mode occupations with the coefficients of binomial form

$$|\Psi\rangle = \sum_{n=0}^{N} C_n |n, N-n\rangle = \frac{1}{2^{N/2}} \sum_{n=0}^{N} \sqrt{\binom{N}{n}} |n, N-n\rangle. \tag{3.21}$$

For $N \gg 1$ the binomial distribution given in Eq. (3.21) can be approximated with a Gaussian distribution

$$\frac{1}{2^{N/2}} \sqrt{\binom{N}{n}} \approx \frac{1}{(\sigma^2 \pi/2)^{1/4}} e^{-\frac{(n-\frac{N}{2})^2}{\sigma^2}} \tag{3.22}$$

with the width $\sigma = \sqrt{N}$ controlling fluctuations between the two modes. Measuring the spin component along x direction we obtain $\left\langle \hat{J}_x \right\rangle = N/2$, while measurements in any orthogonal direction give $\left\langle \hat{J}_\perp \right\rangle = 0$ and $\Delta^2 \hat{J}_\perp = \frac{N}{4}$. Therefore, no squeezing is present as $\xi^2 = 1$, and sensitivity of phase estimation $\Delta\theta = 1/(mN)$ corresponds to a shot-noise limit.

Positive Nonlinearity

For positive effective nonlinearity ($\Lambda > 0$) the ground state of Hamiltonian (3.19) can mostly be approximated by the Gaussian distribution with $\sigma_N < \sqrt{N}$, characterizing a squeezed atom-number distribution. Therefore the fluctuations of spin along the z-axis ($\Delta \hat{J}_z$) will be reduced at the cost of anti-squeezing in the y-direction. We can distinguish three regimes depending on the value of Λ [90]: the Rabi, Josephson and Fock regimes.

In the Rabi regime ($0 < \Lambda \ll 1$), the BJJ is dominated by tunneling and so a relative phase between the two modes is well-defined, leading to high coherent states $\left(\left\langle \hat{J}_x \right\rangle \approx N/2\right)$. With the Gaussian ground state approximation we obtain

$$\Delta^2 \hat{J}_z = N^2 \sigma_z^2 / 4, \tag{3.23a}$$

$$\Delta^2 \hat{J}_y = N^2 \sigma_\phi^2 / 4, \tag{3.23b}$$

where the number and phase distribution widths are

$$\sigma_z^2 = 1/(N\sqrt{\Lambda + 1}), \tag{3.24a}$$

$$\sigma_\phi^2 = \sqrt{\Lambda + 1}/N. \tag{3.24b}$$

Therefore we see that the state is spin-squeezed in z-direction and the parameter from Eq. (3.18) is given by

$$\xi_R^2 = \frac{1}{\sqrt{\Lambda + 1}}. \tag{3.25}$$

In the Josephson regime, $1 \ll \Lambda \ll N$, the number fluctuations are further reduced, but coherence remains high and the Gaussian approximation still holds. The Gaussian number and phase distribution widths are well approximated by $\sigma_z^2 = 1/(N\sqrt{\Lambda})$ and

$\sigma_\phi^2 = \sqrt{\Lambda}/N$, hence the number-squeezing parameter is given by

$$\xi_R^2 = \frac{1}{\sqrt{\Lambda}}. \tag{3.26}$$

In the Fock regime, where the effective nonlinearity is very large comparing to the atom number, $\Lambda \gg N^2$, a fragmented BEC is created. The phase fluctuations in the Fock regime are ill-defined and the Gaussian approximation is no longer valid. In the limit of $N \to \infty$ the energetically favorable state is the one where all atoms are equally divided between both modes, consequently it is approximated by

$$|\Psi\rangle_{GS} \approx |N/2\rangle_a |N/2\rangle_b \qquad \text{for even } N \tag{3.27a}$$

$$|\Psi\rangle_{GS} \approx \frac{1}{\sqrt{2}} \left(|\frac{N+1}{2}\rangle_a |\frac{N-1}{2}\rangle_b + |\frac{N-1}{2}\rangle_a |\frac{N+1}{2}\rangle_b \right) \qquad \text{for odd } N. \tag{3.27b}$$

In this regime, the ground state is an extremely spin-squeezed state with both number fluctuations $\Delta^2 \hat{J}_z$ and mean spin length $\left\langle \hat{J}_x \right\rangle$ vanishing; however the squeezing parameter ξ_R^2 is finite, but susceptible to experimental noise. It is given by

$$\xi_R^2 = \frac{2}{N+2} \qquad \text{for even } N \tag{3.28a}$$

$$\xi_R^2 = \frac{4N}{N(N+2)+1} \qquad \text{for odd } N. \tag{3.28b}$$

Negative Nonlinearity

In the symmetric Josephson junction, a negative nonlinearity favors a configuration in which all the particles are localized in one mode, hence the number fluctuations are enhanced. Competition between the coupling and interaction gives rise to quantum phase transition with discrete symmetry breaking, which occurs at $\Lambda = -1$ in the thermodynamic limit ($N \to \infty$ and $\chi \to 0$) [91–93]. The properties of the condensate near the transition point have been studied in recent years [94, 95], leading to a distinction between two phases: the disordered phase and the ordered phase.

In the disordered phase, $1 < \Lambda < 0$, the Gaussian approximation remains valid for weak attractive interactions (thus Eqs. (3.23) and (3.24) remain valid as well). The phase fluctuations are reduced, compared to the noninteracting case, at the cost of the atom number anti-squeezing. The state remains coherent, $\left\langle \hat{J}_x \right\rangle \approx N/2$, and the squeezing parameter is given by

$$\xi_R^2 = \sqrt{\Lambda + 1}. \tag{3.29}$$

The ordered phase, corresponding to $\Lambda < -1$, is characterized by the macroscopic superposition of the states of atoms localized on the left and on the right well of the effective double-well potential given by Eq. (3.13). The ground state can be approximated by the superposition of two Gaussian distributions centered at $z_\pm = \pm\sqrt{1 - 1/\Lambda^2}$, which in the basis of mode occupations for even N has the form

$$|\Psi\rangle_{GS} = \sum_{n=0}^{N/2} \frac{1}{\sqrt{2}(\sigma^2\pi/2)^{1/4}} \left(e^{-\frac{(n-\frac{N}{2}z_+)^2}{\sigma^2}} |n, N-n\rangle + e^{-\frac{(n-\frac{N}{2}z_-)^2}{\sigma^2}} |N-n, n\rangle \right), \tag{3.30}$$

where $\sigma = \frac{\sqrt{\Lambda^2-1}}{N|\Lambda|}$. With increasing attractive interactions, the mean spin length is vanishing ($\left\langle \hat{J}_x \right\rangle = \frac{N}{2}\frac{1}{|\Lambda|}$) and the ground state is no longer squeezed since

$$\xi_R^2 = |\Lambda|\sqrt{\Lambda^2 - 1}. \tag{3.31}$$

For $\Lambda \ll -\sqrt{N}$ the ground state can be approximated by a NOON state, a superposition of all particles either in a or in b mode:

$$|\Psi\rangle_{GS} = \frac{1}{\sqrt{2}}(|N,0\rangle + |0,N\rangle), \tag{3.32}$$

which leads to maximal fluctuations of the atom number imbalance between two modes. Therefore, it is sensitive to rotations around the z-axis as the quantum Fisher information given by Eq. (2.57) reaches the Heisenberg limit, namely $F_Q = 4\Delta^2\hat{J}_z = N^2$. Although it is useful for quantum metrology, infinitesimally small energy imbalances ($\delta \neq 0$) destroy the symmetry of $W_0(z)$ and thus the state in Eq. (3.32).

The insight into the structure of the ground states of the BJJ model is important in the perspective of construction of a witness capable of detecting the Bell correlations in the system. However, before we present the main results of this chapter, we must discuss the procedure of estimation of a relative phase between two interfering BECs.

3.3 Estimation from the One-body Density Function

The first step of this estimation scheme is the preparation of a BEC in a double well. After that step is completed, a phase shift φ between two modes can be imprinted. This is done by applying an external force that leads to an energy imbalance δ_φ between the two modes for a time t_φ short enough so the effects of tunneling and interaction are negligible $\chi t_\varphi, \Omega t_\varphi \ll \varphi$, where $\varphi = \delta_\varphi t_\varphi$ (we set $\hbar \equiv 1$). In the next step, the trap is turned off and the wave packets, initially localized in the two wells, expand and overlap. Consequently, the field operator can be approximated by

$$\hat{\Psi}(\mathbf{r}, t_f, \varphi) = \phi(\mathbf{r}, t_f)(\hat{a}e^{\frac{i}{2}(\mathbf{kr}+\varphi)} + \hat{b}e^{-\frac{i}{2}(\mathbf{kr}+\varphi)}), \tag{3.33}$$

where $\phi(\mathbf{r}, t_f)$ is the common envelope, $\mathbf{k} = 2\mathbf{r}_0 M/t_f, 2\mathbf{r}_0$ is the vector pointing from the center of one well to the other, M is the mass of an atom and t_f is the flight time.

After the expansion time t_f, in so-called far-field, the wave packets form fringes and the phase φ can be estimated [96] using the fit of the normalized one-body density function

$$\varrho(\mathbf{r}, t_f, \varphi) = \frac{\left\langle \hat{\Psi}(\mathbf{r}, t_f, \varphi)^\dagger \hat{\Psi}(\mathbf{r}, t_f, \varphi) \right\rangle}{N}. \tag{3.34}$$

Using the field operators from Eq. (3.33) we obtain

$$\begin{aligned} \varrho(\mathbf{r}, t_f, \varphi) &= \frac{1}{N}|\phi(\mathbf{r}, t_f)|^2 \left\langle \hat{a}^\dagger\hat{a} + \hat{b}^\dagger\hat{b} + \hat{a}^\dagger\hat{b}e^{-\frac{i}{2}(\mathbf{kr}+\varphi)} + \hat{b}^\dagger\hat{a}e^{\frac{i}{2}(\mathbf{kr}+\varphi)} \right\rangle = \\ &= |\phi(\mathbf{r}, t_f)|^2 \left[1 + \frac{2}{N}\left(\left\langle \hat{J}_x \right\rangle \cos(\mathbf{kr}+\varphi) + \left\langle \hat{J}_y \right\rangle \sin(\mathbf{kr}+\varphi)\right)\right]. \end{aligned} \tag{3.35}$$

For the Hamiltonian (3.19) the eigenstates have real coefficients in the occupation basis, thus $\left\langle \hat{J}_y \right\rangle = 0$. This condition will also hold when we will consider different

sources of the noise, such as thermal fluctuations. Therefore, the visibility of the fringes is given with

$$\nu = \frac{\varrho_{\max} - \varrho_{\min}}{\varrho_{\max} + \varrho_{\min}} = \frac{2}{N} |\left\langle \hat{J}_x \right\rangle|, \text{ where} \tag{3.36a}$$

$$\varrho_{\max/\min} = \frac{|\phi(\mathbf{r}, t_f)|^2}{N} \left(N \pm 2 \left| \left\langle \hat{J}_x \right\rangle \right| \right). \tag{3.36b}$$

Hence, the one-body density can be expressed using the visibility ν as follows

$$\varrho(\mathbf{r}, t_{\mathrm{f}}; \varphi) = \frac{\left\langle \hat{\Psi}^\dagger(\mathbf{r}, t_{\mathrm{f}}, \varphi) \hat{\Psi}(\mathbf{r}, t_{\mathrm{f}}, \varphi) \right\rangle}{N} = 1 + \nu \cos(\mathbf{k} \cdot \mathbf{r} + \varphi). \tag{3.37}$$

In the experiment, the central interference fringes, where the density is almost constant, are of primary interest.

The phase estimation of φ can be performed by fitting the one-body density $\varrho(\mathbf{r}, t_{\mathrm{f}}; \varphi_{\mathrm{est}})$ to the measurement of the position of the atoms, i.e. by using the least-squares method, with φ_{est} as a free parameter. This gives an asymptotically unbiased estimator φ_{est} of φ [97]. Sensitivity of the double-well interferometer, thus a variance of the estimator φ_{est}, has the following form [97]

$$\Delta^2 \varphi_{\mathrm{est}} = \frac{1}{N} \left[\xi_\phi^2 + \frac{\sqrt{1 - \nu^2}}{\nu^2} \right], \tag{3.38}$$

where $\xi_\phi^2 = N \left\langle \hat{J}_y^2 \right\rangle / \langle \hat{J}_x \rangle^2$ is the spin-squeezing parameter [98]. When $\xi_\phi^2 < 1$, the state is phase-squeezed [88, 89], with reduced variance of $\hat{J}_y$ spin component. We introduce the parameter

$$\mathcal{A} \equiv N \Delta^2 \phi_{est} - 1 = \xi_\phi^2 + \frac{\sqrt{1 - \nu^2} - \nu^2}{\nu^2} \tag{3.39}$$

which indicates sub-shot noise sensitivity when $\mathcal{A} < 0$.

In the next section we present the main result of this chapter by introducing a Bell witness capable of detecting the Bell correlations and relating it to the parameter $\mathcal{A}$.

3.4 The Bell Inequality Witness

Bell correlations can be observed in the states that are entangled, although entanglement alone is insufficient for nonlocality. Therefore, the entanglement criteria, such as the separability condition or the squeezing parameter from Eq. (3.18), cannot be used to determine if a system violates a Bell inequality. However, in this section we will introduce a criterion that adapts the squeezing parameter and will relate it to the sensitivity of the double-well interferometer introduced in the previous section.

We focus on the Bell witness introduced in Refs. [99, 100], i.e. $B(\theta) \equiv \langle \hat{B}(\theta) \rangle$, where

$$\hat{B}(\theta) = 2N \cos^2\left(\frac{\theta}{2}\right) - 4\hat{J}_1 + +8 \sin^2\left(\frac{\theta}{2}\right) \left[-\hat{J}_1 \sin\left(\frac{\theta}{2}\right) + \hat{J}_2 \cos\left(\frac{\theta}{2}\right) \right]^2 \tag{3.40}$$

is built from only one- and two-body operators. $\hat{J}_1$ and $\hat{J}_2$ denote a pair of operators in the orthogonal directions. The Bell witness signals Bell correlations if $B(\theta) < 0$.

To relate the parameter $\mathcal{A}$ to the witness of Bell correlations, we choose

$$\begin{pmatrix} \hat{J}_1 \\ \hat{J}_2 \end{pmatrix} = \begin{pmatrix} \cos\frac{\theta}{2} & -\sin\frac{\theta}{2} \\ \sin\frac{\theta}{2} & \cos\frac{\theta}{2} \end{pmatrix} \begin{pmatrix} \hat{J}_x \\ \hat{J}_y \end{pmatrix}, \tag{3.41}$$

and apply it to Eq. (3.40). As a result, we arrive with the Bell operator [100] of the form

$$\hat{B}(\theta) = 2N\cos^2\frac{\theta}{2} - 4\left(\hat{J}_x\cos\frac{\theta}{2} - \hat{J}_y\sin\frac{\theta}{2}\right) + 8\sin^2\frac{\theta}{2}\hat{J}_y^2. \tag{3.42}$$

The minimization of $B(\theta)$ with respect to θ gives

$$\cos\left(\frac{\theta_0}{2}\right) = \frac{\nu}{2(1-\xi_\phi^2\nu^2)}. \tag{3.43}$$

Substituting condition from Eq. (3.43) into Eq. (3.42) leads to an inequality that signals Bell correlations when

$$\mathcal{B} \equiv \xi_\phi^2 + \frac{\sqrt{1-\nu^2}-1}{2\nu^2} < 0, \tag{3.44}$$

the result first obtained in [100]. Finally, the relation between parameter $\mathcal{A}$, from Eq. (3.39), and $\mathcal{B}$ can be established by a function of the fringe visibility:

$$\mathcal{B} = \mathcal{A} + f(\nu), \tag{3.45}$$

where $f(\nu) = 1 - \frac{\sqrt{1-\nu^2}+1}{2\nu^2}$. Therefore sensitivity of the estimation procedure based on a fit to a one-body density can signal the presence of the Bell correlations in the system. We will now illustrate the results for the system of the BEC trapped in a double-well potential.

3.5 The Results

Noiseless Case

First we present the noiseless case of the balanced system ($\delta = 0$) given by Hamiltonian (3.12). The analytical expressions for $\mathcal{A}$ and $\mathcal{B}$ can be derived assuming the semi-classical approximation [101, 102] with $N \gg 1$.

In the region of negative nonlinearities – attractive interactions – the system is phase-squeezed when $-(1+\sqrt{5})/2 < \Lambda < 0$ [103]. However, for the semi-classical approximation we need to consider two areas: for $-1 \lesssim \Lambda < 0$, in which the visibility is constant and approximately $\nu \approx 1$; and for $-(1+\sqrt{5})/2 < \Lambda \lesssim -1$, where the visibility drops rapidly and is given with $\nu \approx 1/|\Lambda|$. In the first case, the phase-squeezing parameter is approximated with Eq. (3.29): $\xi_\phi^2 \approx \sqrt{1+\Lambda}$, and, therefore, according to Eqs. (3.39) and (3.45) the parameters $\mathcal{A}$ and $\mathcal{B}$ are:

$$\mathcal{A} \approx \sqrt{1+\Lambda} - 1, \qquad \mathcal{B} \approx \sqrt{1+\Lambda} - 1/2. \tag{3.46}$$

From the above equations we see that the Bell correlations are witnessed ($\mathcal{B} < 0$) when $\xi_\phi^2 < 1/2$ and thus $\Lambda < -3/4$. In the second case, the visibility drops according

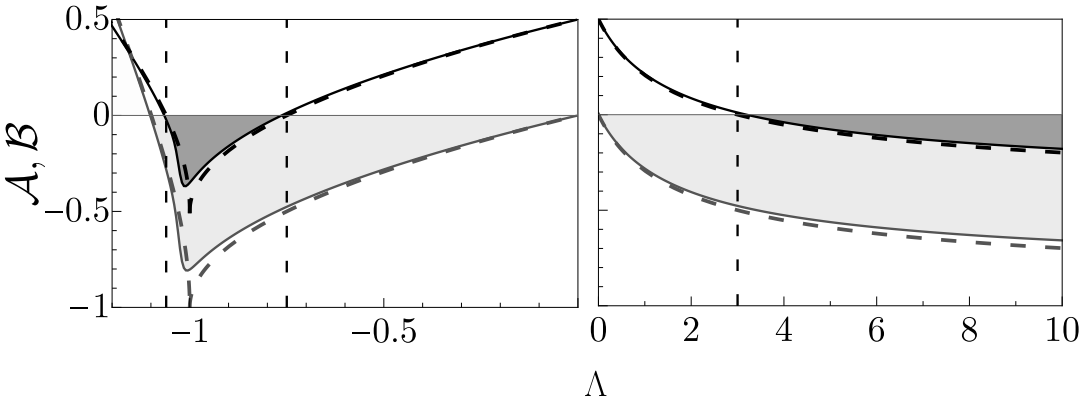

Figure 3.1: Coefficients $\mathcal{A}$ (gray lines) and $\mathcal{B}$ (black lines) as a function of interaction strength Λ for $T = 0$, $\delta = 0$ and $N = 1000$. The dashed and solid lines represent analytical and numerical results, respectively. The shaded regions indicate where $\mathcal{A} < 0$ (lighter) and $\mathcal{B} < 0$ (darker). Additionally, vertical lines for $\Lambda = \frac{-3}{2\sqrt{2}}, -\frac{3}{4}$, and 3 indicate the value of Λ, which is the analytical solution for $\mathcal{B} = 0$.

to $\nu \approx 1/|\Lambda|$ and $\xi_\phi^2 \approx |\Lambda|\sqrt{\Lambda^2 - 1}$ as in Eq. (3.31). We obtain

$$\mathcal{A} \approx 2|\Lambda|\sqrt{\Lambda^2 - 1} - 1, \quad \mathcal{B} \approx \frac{3}{2}|\Lambda|\sqrt{\Lambda^2 - 1} - \frac{\Lambda^2}{2}. \tag{3.47}$$

Here the Bell correlations are present when $\Lambda > -3/(2\sqrt{2})$. The analytic formulas derived in Eqs. (3.46) and (3.47) are accurate in the thermodynamical limit $N \to \infty$ except for the point $\Lambda = -1$, where the effective potential changes [103].

In the regime of repulsive interactions ($0 \leqslant \Lambda \ll N^2$) the ground state of the Hamiltonian (3.12) is number-squeezed: $\xi_N^2 = N(\Delta \hat{J}_z)^2/\langle \hat{J}_x \rangle^2 < 1$ [98, 104, 105]. The additional rotation through $\pi/2$ around the x axis is, consequently, required to transform number-squeezing into phase-squeezing, since the phase estimation from the interference pattern requires phased-squeezed states for sub-shot noise sensitivity, see Eq. (3.38). The realization of such transformation can be obtained, for example, by quench of tunneling for a time $t_{\pi/2}\Omega = \pi/2$ such that $t_{\pi/2}\chi \ll 1$. This transformation does not entangle the atoms and sustains $\nu \approx 1$. As a result, we obtain

$$\mathcal{A} \approx \frac{1}{\sqrt{1 + \Lambda}} - 1, \quad \mathcal{B} \approx \frac{1}{\sqrt{1 + \Lambda}} - \frac{1}{2}. \tag{3.48}$$

The observation of Bell correlations, $\mathcal{B} < 0$, is possible for states where $\xi_\phi^2 < 1/2$ and, from Eq. (3.48), we can see that it is satisfied for $\Lambda > 3$. In Fig. 3.1 we show $\mathcal{A}$ (solid line) and $\mathcal{B}$ (dashed line) as a function of Λ for $N = 1000$. The numerical calculations obtained with the method of exact diagonalization of BJJ Hamiltonian, Eq. (3.19), reproduce well the analytical formulas derived in this chapter. The slight divergence observed for $\Lambda > 3$ is caused by the approximation of the perfect visibility, $\nu = 1$ in Eq. (3.48), and by the finite atom number used in the numerical calculations compared to the thermodynamical limit $N \to \infty$ for analytic formulas.

Please note: in a realistic experiment the final precision will be affected by many factors. Therefore, as we proceed it is important to incorporate such factors into our considerations.

Noisy Case

Energy Imbalance Fluctuations

We now present a case where the wells are not perfectly balanced, i.e. $\delta \neq 0$, which is one of the main sources of noise present in current double-well experiments [106, 107]. In a general experiment, the parameter δ can change from shot to shot, so consequently we model these fluctuations with a Gaussian distribution of width σ_δ. The quantum state in this case will be described with a density matrix

$$\hat{\varrho}_{\sigma_\delta,\Lambda} = \mathcal{N} \int d\delta \, e^{-\frac{\delta^2}{2\sigma_\delta^2}} |\Psi_{\delta,\Lambda}\rangle\langle\Psi_{\delta,\Lambda}|, \tag{3.49}$$

where $\mathcal{N}$ is the normalization constant and $|\Psi_{\delta,\Lambda}\rangle$ is the ground state of Hamiltonian (3.12) for given Λ and δ. Coefficients $\mathcal{A}$ and $\mathcal{B}$ can be calculated numerically. We plot the results in Figs. 3.2(a) and (b). The gray-scaled regions therein correspond to $\mathcal{B} < 0$ signaling presence of the Bell correlations. We observe that the increase of σ_δ shrinks the regions. Moreover, the effect is much greater for $\Lambda < 0$. The sub-shot noise sensitivity regime, $\mathcal{A} < 0$, shrinks proportionally, according to Eq. (3.45).

Thermal Fluctuations

We will now consider the system in a finite temperature. In such a case the system is described with the density matrix at thermal equilibrium for the Hamiltonian (3.12), given as

$$\hat{\varrho}_{\text{th}} = \frac{1}{\mathcal{Z}} \sum_{n=0}^{N} |\Psi_n\rangle\langle\Psi_n| e^{-\beta E_n}, \tag{3.50}$$

where $\mathcal{Z}$ is the partition function, $\hat{H}|\Psi_n\rangle = E_n|\Psi_n\rangle$ and $\beta = E_J/(k_B T)$ (where k_B is the Boltzmann constant). The coefficients $\mathcal{A}$ and $\mathcal{B}$ are calculated using $\hat{\varrho}_{\text{th}}$ for the corresponding spin moments, for example $\left\langle \hat{J}_y^2 \right\rangle_{\text{th}} = \text{Tr}\left[\hat{\varrho}_{\text{th}} \hat{J}_y^2\right] = \sum_{n=0}^{N} \frac{e^{-\beta E_n}}{\mathcal{Z}} \langle\Psi_n|\hat{J}_y^2|\Psi_n\rangle$. Results from the numerical calculations are presented in Figs. 3.2(c) and (d). The dashed lines in these plots stand for the case $\mathcal{B} = 0$ and are obtained from an analytical formula for the spin-squeezing parameter [103], valid for sufficiently large N:

$$\xi_\phi^2(T) = \left\{ \begin{array}{ll} |\Lambda|\sqrt{\Lambda^2 - 1} \coth\left(\frac{\beta\sqrt{\Lambda^2-1}}{2}\right), & \Lambda < -1, \\ \sqrt{1+\Lambda} \coth\left(\frac{\beta\sqrt{1+\Lambda}}{2}\right), & -1 < \Lambda < 0, \\ \frac{1}{\sqrt{1+\Lambda}} \coth\left(\frac{\beta\sqrt{1+\Lambda}}{2}\right), & \Lambda > 0, \end{array} \right\} \tag{3.51}$$

under an assumption that visibility is unaffected by temperature. The thermal noise is responsible for a spread of spin fluctuations in any direction, therefore it is justified to approximate mean spin length $\left\langle \hat{J}_x \right\rangle$ by formulas valid for $T = 0$.

Finite Resolution

Another source of noise that can impact the experiment is the finite resolution in the detection of the atoms. In order to account for this effect in our formulas we convolute the density in Eq. (3.35) with a Gaussian probability of detecting an atom

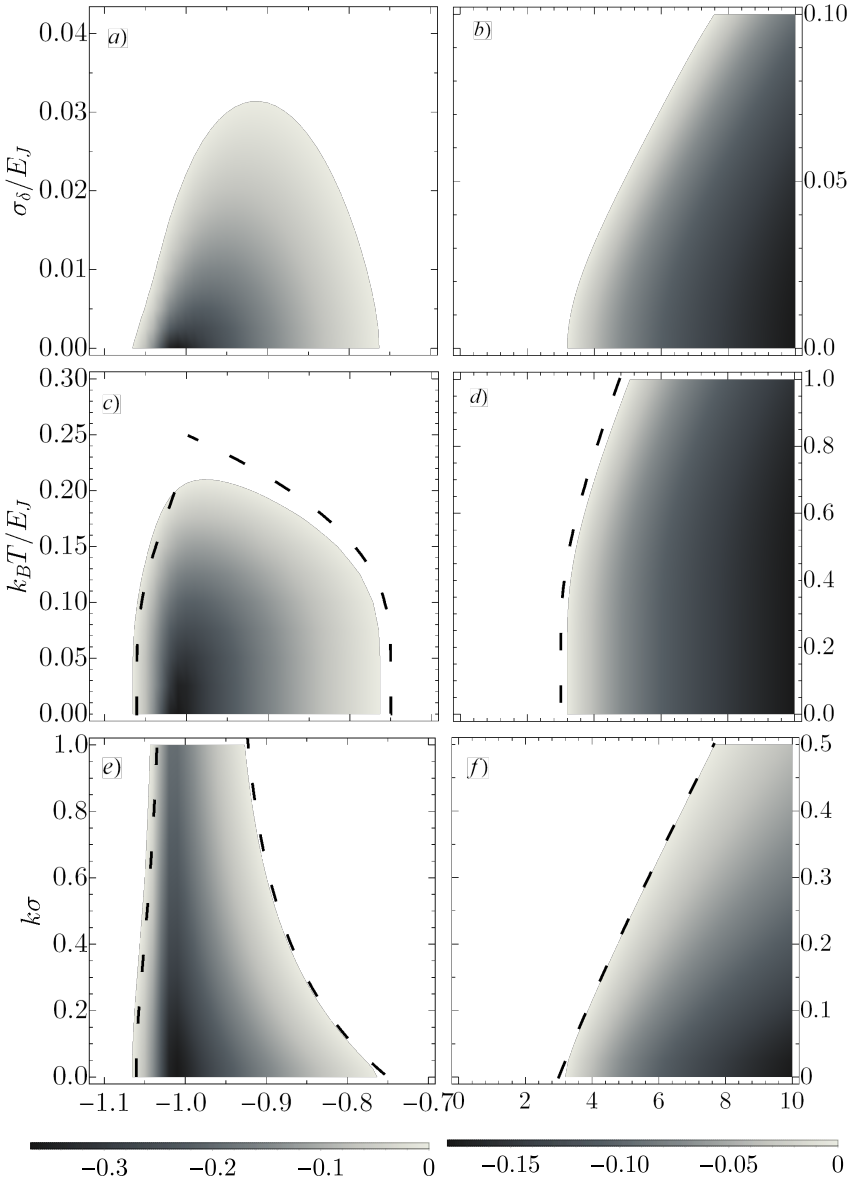

Figure 3.2: Numerical calculations for $N = 1000$ for $\mathcal{B}$ with the shaded regions corresponding to $\mathcal{B} < 0$. The dashed lines in panels $(c) - (f)$ are analytic predictions for $\mathcal{B} = 0$ obtained from Eq. (3.53). Panels (a) and (b) show the effect of the energy imbalance (modeled as a normal distribution with width σ_δ) at $T = 0$; (c) and (d) show the case of finite temperature T, for $\sigma_\delta = 0$; (e) and (f) show the effect of finite resolution σ of spatial detection of the atoms, at $T = 0$ and $\sigma_\delta = 0$.

at position $\mathbf{r}$ instead on its true position $\mathbf{r}'$:

$$\tilde{\varrho}(\mathbf{r}, t_f; \varphi) = \frac{1}{(\sqrt{2\pi}\sigma)^3} \int d\mathbf{r}' \; e^{-\frac{(\mathbf{r}-\mathbf{r}')^2}{2\sigma^2}} \varrho(\mathbf{r}', t_f; \varphi) = \\ = 1 + \tilde{\nu} \cos(\mathbf{k} \cdot \mathbf{r} + \varphi), \tag{3.52}$$

where $\tilde{\nu} = \nu e^{-\frac{1}{2}k^2\sigma^2}$ is blurred visibility. Therefore, using $\tilde{\varrho}(\mathbf{r}, t_f; \varphi)$, we can calculate the sensitivity $\Delta^2\varphi_{\text{est}}$, which is equivalent to replacing ν with $\tilde{\nu}$ in Eq. (3.44) and

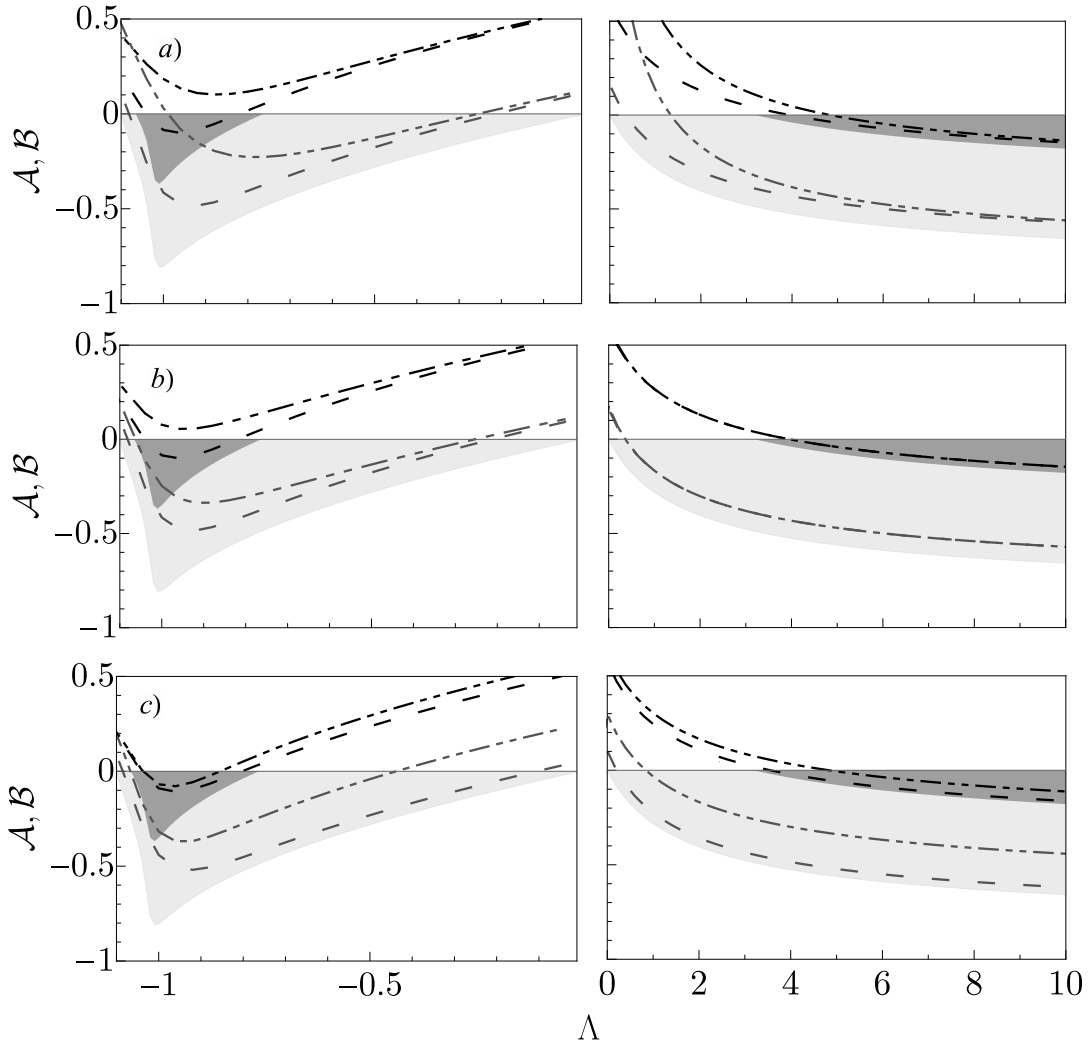

Figure 3.3: Coefficients $\mathcal{A}$ (gray lines) and $\mathcal{B}$ (black lines) in the presence of the accumulated impact of all types of noise in a function of the interaction strength Λ for both negative (left column) and positive (right column) nonlinearity and $N = 500$. *a*): $T = 0.1$, $\sigma = 0.1$, $\sigma_\delta = 0.01$ (dashed line) and $\sigma_\delta = 0.05$ (dash-dotted line) *b*): $\sigma_\delta = 0.01$, $\sigma = 0.1$, $T = 0.1$ (dashed line) and $T = 0.2$ (dash-dotted line) *c*): $\sigma_\delta = 0.01$, $T = 0.1$, $\sigma = 0.05$ (dashed line) and $\sigma = 0.2$ (dash-dotted line). The shaded regions signal the sub-shot noise sensitivity (light gray line) and Bell correlations (dark gray line) present in an ideal noise-free case.

using the temperature dependent phase-squeezing parameter from Eq. (3.51). As a result, we obtain the formula for the Bell witness, i.e.

$$\mathcal{B}(T, \sigma) = \xi_\phi^2(T) + \frac{\sqrt{1 - \tilde{\nu}^2} - 1}{2\tilde{\nu}^2}. \tag{3.53}$$

We plot the results for $T = 0$ on Figs. 3.2(e) and (f) showing $\mathcal{B}(0, \sigma) < 0$ with the shaded regions. The dashed lines correspond to the analytical predictions for $\mathcal{B} = 0$.

In Fig. 3.3 we show the combined effect of all the sources of noise we presented so far, both on $\mathcal{A}$ and $\mathcal{B}$. In the top row a) we show that the increase of Gaussian width σ_δ from 0.01 to 0.05 (i.e., from dashed to dash-dotted lines, with fixed $T = 0.1$ and $\sigma = 0.1$) has great impact, especially on $\mathcal{B}$ in the regime of attractive interactions.

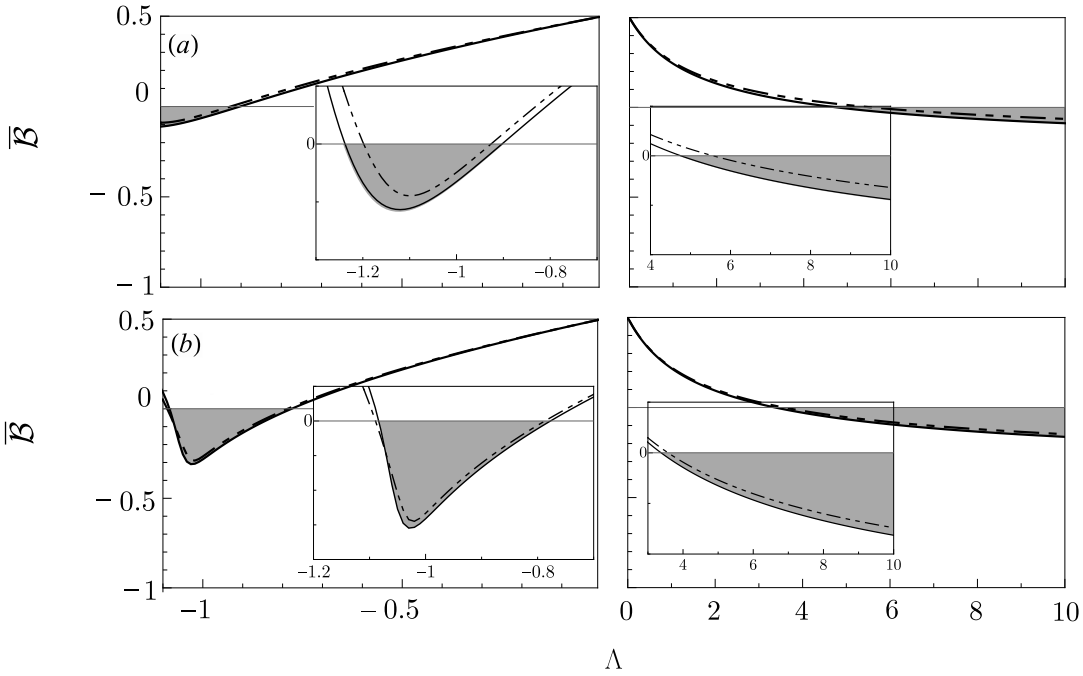

Figure 3.4: The Bell witness $\overline{\mathcal{B}}$ in the presence of atom number fluctuations. (*a*) $\bar{N} = 30$ (top row) with $\sigma_N = \sqrt{\bar{N}}$ (solid line) and $\sigma_N = 20$ (dash-dotted line). (*b*) $\bar{N} = 300$ and $\sigma_N = \sqrt{\bar{N}}$ (solid line) and $\sigma_N = 200$ (dash-dotted line). Gray areas indicate regions where $\mathcal{B}$ detects the Bell correlations, i.e. in the absence of atom number fluctuations.

This can also be seen in the middle row *b*) when the temperature increases from $T = 0.1$ to $T = 0.2$ (with fixed $\sigma = 0.1$ and $\sigma_\delta = 0.01$). However, a loss of resolution from 0.05 to 0.2 with fixed $\sigma_\delta = 0.01$ and $T = 0.2$ does not have a strong effect in any of the regions, as can be observed in the bottom row *c*). These observations can be helpful for designing future experiments with entangled quantum gases.

Atom Number Fluctuations

In the last part of this section we include the atom number fluctuations. We construct a mixture, based on the method in the supplementary materials of Ref. [100], as follows

$$\hat{\varrho}_{\sigma_N,\Lambda} = \sum_{N=0}^{\infty} \mathcal{P}_N |\psi_{N,\Lambda}\rangle\langle\psi_{N,\Lambda}|, \tag{3.54}$$

where $|\psi_{N,\Lambda}\rangle$ is the ground-state of the Hamiltonian (3.12) at $\delta = 0$ and fixed N and Λ, and $\mathcal{P}_N$ is the probability for having N atoms in the system, modeled with a Gaussian function of width σ_N, i.e.

$$\mathcal{P}_N \propto \exp\left[-\frac{(N-\bar{N})^2}{2\sigma_N^2}\right]. \tag{3.55}$$

Here $\bar{N}$ stands for the mean number of atoms in the system and the proportionality stands for the normalization.

The angular momentum operators, $\hat{J}_x, \hat{J}_y, \hat{J}_z$, act within a fixed-$N$ subspace of the total Hilbert space, therefore we divide the Bell operator from Eq. (3.40) by the atom

number operator $\hat{N}$, which results with the witness analogical to that in Eq. (3.42), namely

$$b(\theta) = 2\cos^2\left(\frac{\theta}{2}\right) - 4x\cos\left(\frac{\theta}{2}\right) + 8y^2\sin^2\left(\frac{\theta}{2}\right), \tag{3.56}$$

where we introduce

$$x = \left\langle \frac{\hat{J}_x}{\hat{N}} \right\rangle, \quad y^2 = \left\langle \frac{\hat{J}_y^2}{\hat{N}} \right\rangle \tag{3.57}$$

and the expectation value is calculated on the state given with Eq. (3.54). This expression can be optimized with respect to θ which leads to the inequality

$$\overline{\mathcal{B}} \equiv \frac{y^2}{x^2} + \frac{\sqrt{1-4x^2}-1}{8x^2} < 0 \tag{3.58}$$

signaling the presence of Bell correlations. In Fig. 3.4 we plot $\overline{\mathcal{B}}$ for $\bar{N} = 30$ (top row) with the typical fluctuations expected in the experiment at the shot-noise level, i.e. $\sigma_N = \sqrt{\bar{N}} \simeq 5.5$ (solid line), and to compare, with the much greater value $\sigma_N = 20$ (dash-dotted line). The bottom row presents the results for $\bar{N} = 300$ and analogically: $\sigma_N = \sqrt{\bar{N}} \simeq 17.3$ (solid line) and $\sigma_N = 200$ (dash-dotted line). Additionally, we plotted gray regions indicating Bell correlations for the case with no atom-number fluctuations (i.e., $\sigma_N \to 0$). We observe small changes with the fluctuations at the shot-noise level in both the low-$\bar{N}$ and the high-$\bar{N}$ case, because, in a good approximation, $\mathcal{B}$ is intensive in N (see Eqs. (3.46), (3.47) and (3.48)). In consequence both x and y^2 have weak dependence on N in this regime. Only vast atom number fluctuations shrink the region of Λ, for which the Bell correlations can be detected by Eq. (3.56).

In this chapter we presented a method to detect non-local Bell correlations from the interference pattern formed by atoms released from a double-well potential. We found the relation between the Bell coefficient $\mathcal{B}$ introduced in Refs. [100, 108] with the precision of the phase estimation through a fit of the one-body density to the interference pattern. We showed the influence of the noise effects – energy imbalance between the wells, non-zero temperature, finite resolution and atom number fluctuations. The energy imbalance and finite temperature have a significant impact on the regions where Bell correlations can be detected, especially for attractive interactions. In the current experiments, the remaining two sources seem to be less destructive. In the next chapter we will show that the bosonic Josephson junction can also be achieved in spinor-1 condensates. We will consider a case where the system is not described by the ground state of the Hamiltonian but, instead, is initially prepared in the particular state. Such a state is a subject of unitary evolution which correlates atoms and provides entangled states useful for metrology. In this scenario the quantum Fisher information scales with the Heisenberg limit, although it varies during the time evolution. We will show that the dynamics governed by the BJJ Hamiltonian produce entangled states useful for quantum metrology.

Chapter 4

Entanglement in the System of Ultra-cold Atoms

In this chapter we report on the results of collaboration with dr hab. Emilia Witkowska from the Institute of Physics at The Polish Academy of Sciences [109]. During the past three years we have been exploring spin-1 Bose-Einstein condenstates for application in quantum metrology which resulted with articles published in [110, 111]. Although in the original work we presented a scheme for the dynamical stabilization of entanglement, here we limit our description to analysis of the generation of entangled states useful for ultraprecise interferometry. We start with the general description of the spin-1 systems. We show similarities in the mean-field approximation between spinor (spin-1) and, as described in the previous section, the two-mode condensate in a double-well potential. We derive the optimal interferometer rotation during the entire time evolution and provide an efficient measurement choice in order to obtain precision proportional to Heisenberg scaling.

Contents

Multi-component Bose-Einstein condensates are acknowledged as highly controllable systems which could be used for the generation of entangled states [112–119] for application in atomic interferometry [120, 121]. In this chapter, we focus on Bose condensates with a total spin $F = 1$. The spin-1 condensate consists of three components (modes) distinguished by the quantum magnetic number of internal levels $m_F = 0, \pm 1$ with conserved magnetization of the system $M = N_+ - N_-$, where $N_\pm$ is a number of atoms occupying $m = \pm 1$ level. The many-body Hamiltonian for such a system has a form

$$\hat{H} = \int d\mathbf{r} \hat{\Psi}_i^\dagger(\mathbf{r}) \left(-\frac{\hbar^2 \nabla^2}{2m} + V_{ext}(\mathbf{r}) \right) \hat{\Psi}_i(\mathbf{r}) + \int d\mathbf{r} \hat{\Psi}_i^\dagger(\mathbf{r}) \left(p m_F + q m_F^2 \right) \hat{\Psi}_i(\mathbf{r}) + \quad (4.1)$$
$$+ \frac{c_0}{2} \int d\mathbf{r} \hat{\Psi}_i^\dagger(\mathbf{r}) \hat{\Psi}_j^\dagger(\mathbf{r}) \hat{\Psi}_j(\mathbf{r}) \hat{\Psi}_i(\mathbf{r}) + \frac{c_2}{2} \int d\mathbf{r} \hat{\Psi}_i^\dagger(\mathbf{r}) \hat{\Psi}_j^\dagger(\mathbf{r}) \mathbf{F}_{jk} \cdot \mathbf{F}_{il} \hat{\Psi}_k(\mathbf{r}) \hat{\Psi}_l(\mathbf{r}),$$

with the summation convention going over all three m_F states. The vector $\mathbf{F} = (J_x, J_y, J_z)^T$ consists of spin-1 angular momentum matrices (for details see App. A) and $\hat{\Psi}_j(\mathbf{r})$ is a field operator annihilating an atom at the position $\mathbf{r}$ in the given hyperfine state, satisfying the standard commutation relation $\left[\hat{\Psi}_i(\mathbf{r}), \hat{\Psi}_j^\dagger(\mathbf{r}') \right] = \delta_{ij} \delta(\mathbf{r} - \mathbf{r}')$. The first term is a single-particle kinetic energy with external trapping

potential $V_{ext}(\mathbf{r}) = m(\omega_x x^2 + \omega_y y^2 + \omega_z z^2)/2$. The linear Zeeman effect is included in the parameter $p = g\mu_B B$, where g is the Landé g-factor, B is the strength of the magnetic field and μ_B is the Bohr magneton. The quadratic Zeeman coefficient q has two contributions: from the external magnetic field (q_B) and from the microwave or light field (q_{MW}), leading to $q = q_B + q_{WM}$ [122]. The part depending on the magnetic field is given with $q_B = (\mu_B B)^2/(4\Delta E_{hf})$, where ΔE_{hf} is the hyperfine energy splitting. Both the value and the sign of q_{MW} can be tuned independently of q_B by employing a microwave field that is off-resonant with the other hyperfine state [123]. The parameter p is always positive, while the sign of q depends on ΔE_{hf}. The spin-independent and -dependent coefficients, c_0 and c_2 respectively, describe elastic collisions of the spin-1 atom expressed in terms of the scattering length a_0 (a_2) for two spin-1 atoms in the combined symmetric channel of total spin 0 (2): $c_0 = 4\pi\hbar^2(a_0 + 2a_2)/(3m)$ and $c_2 = 4\pi\hbar^2(a_2 - a_0)/(3m)$.

To simplify the Hamiltonian (4.1) we use the single-mode approximation [124, 125], which assumes that the spatial atomic density distribution is equal for each of the spin components and is not affected by the dynamics of the system. The spatial wave function of each mode can be approximated by $\phi_{m_F}(\mathbf{r}) = \phi(\mathbf{r})$ for $m_F = \{-1, 0, 1\}$, where $\phi(\mathbf{r})$ is a solution of the Gross-Pitaevskii equation with spin-dependent interactions neglected [126]. In consequence the field operators can be decomposed in the following way

$$\hat{\Psi}_j(\mathbf{r}) = \hat{a}_j \phi(\mathbf{r}), \tag{4.2}$$

where the boson operator $\hat{a}_j$ annihilates atom in mode j and satisfies a standard commutation relation $\left[\hat{a}_i, \hat{a}_j^\dagger\right] = \delta_{ij}$. The single mode approximation holds for the case where the spin-independent part of the contact interaction dominates over the spin-dependent part [127, 128]. Thus the Hamiltonian of the system (4.1) can be written in the language of generators of $SU(3)$ algebra (App. A) as follows

$$\hat{H} = \mu\hat{N} - c_0'\hat{N}(\hat{N} - 1) + c_2'(\hat{J}^2 - 2\hat{N}) - p\hat{J}_z + q\hat{N}_s, \tag{4.3}$$

where c_0' and c_2' are modified, dependent on the number of atoms in the system N, coefficients: $2c_i' = c_i \int d\mathbf{r}|\phi(\mathbf{r})|^4$. The operator $\hat{J}^2$ is the total spin operator, $\hat{J}_z = \hat{N}_+ - \hat{N}_-$ is the population imbalance between modes $m_F = +1$ and $m_F = -1$, $\hat{N} = \hat{N}_+ + \hat{N}_0 + \hat{N}_-$ is the total particle number operator and $\hat{N}_s = \hat{N}_1 + \hat{N}_{-1}$. To this end, we will consider a Hamiltonian of the form

$$\frac{\hat{H}}{c_2'} = -\frac{1}{2N}\hat{J}^2 + q\hat{N}_s, \tag{4.4}$$

where the constant terms, including linear Zeeman energy, were dropped and $c_2' = -1$ corresponds to the case of ferromagnetic phase of spinor condensate [122, 129]. This system can be employed in experiments, e.g. in $F = 1$ hyperfine manifold using Rb^{87} atoms [119, 130–133].

In the next section we will present a method of obtaining the phase portrait for both the bosonic Josephson junction (BJJ) presented in the previous chapter and the spinor system, and show their similarities from a certain perspective. We will analyze how the presence of fixed points impacts the evolution of the initial states.

4.1 The Structure of Classical Mean-Field Phase Space

We now turn our attention to two-mode systems. Let us recall the BJJ Hamiltonian considered in the previous chapter:

$$\hat{H}_{2\mathrm{m}} = \hbar\chi\hat{S}_z^2 - \hbar\Omega\hat{S}_x, \tag{4.5}$$

where we set $\delta = 0$ and changed the notation of pseudo-spin operators from $\hat{J}_i$ to $\hat{S}_i$ to distinguish two-mode operators from the ones of the spinor system. We introduce the subscript "2m" to distinguish, in general, objects that concern two-mode system. In the previous chapter we obtained a mean-field approximation by replacing the mode operators with complex numbers; here we will use an alternative method. We calculate an average value of Hamiltonian (4.5) on the spin coherent state given by

$$|\varphi,\theta\rangle_{2\mathrm{m}} = e^{-i\varphi\hat{S}_x}e^{-i\theta\hat{S}_y}|N,0\rangle, \tag{4.6}$$

where $\frac{\hat{a}^{\dagger N}}{\sqrt{N!}}|0,0\rangle = |N,0\rangle$ and $\varphi \in [0,2\pi]$, $\theta \in [0,\pi]$. It can be interpreted as a double rotation of a maximally polarized state (with all atoms in the first mode). The calculations give the following formula

$$H_{2\mathrm{m}} = \frac{\Lambda}{2}z^2 - \sqrt{1-z^2}\cos\varphi, \tag{4.7}$$

where $z \equiv \cos\theta$ and $\Lambda = 2N\chi/2\Omega$, which is the same as in Eq. (3.8). The dynamics of unitary evolution are governed by the Hamiltonian (4.7) set by the equations of motion

$$\dot{z} = -\sqrt{1-z^2}\sin\varphi \tag{4.8a}$$

$$\dot{\varphi} = \Lambda z + \frac{z}{\sqrt{1-z^2}}\cos\varphi. \tag{4.8b}$$

The structure of the phase space consists of fixed points and closed trajectories, lines of constant energy, allowing us to study the dynamics of the system, see Fig. 4.1. The distinctive features of the phase portrait are the fixed points at which the velocity field $(\dot{z},\dot{\varphi})$ vanishes. Their position can be found by solving a set of equations ($\dot{z}=0$, $\dot{\varphi}=0$), while the stability can be determined from a stability matrix [134]. We distinguish two important types of fixed points in our system, namely: a stable center fixed point and an unstable saddle fixed point. In the former case all the trajectories near the stable center fixed point are circular. In the latter case the trajectories along one direction move toward and eventually converge at the critical point, while the trajectories in the other direction start at the critical point and diverge away. Every other trajectory moves toward but never converges at the critical point, before changing direction and diverging away. The unitary evolution of the state can be represented using Q-function (or Husimi function) by calculating $Q_{2\mathrm{m}}(\varphi,\theta) = |\langle\Psi(t)|\varphi,\theta\rangle_{2\mathrm{m}}|^2$ for a given time. $|\Psi(t)\rangle$ is the state evolved with the Hamiltonian (4.5) according to

$$|\Psi(t)\rangle_{2\mathrm{m}} = e^{-\frac{i\hat{H}_{2\mathrm{m}}t}{\hbar}}|\Psi_0\rangle_{2\mathrm{m}}, \tag{4.9}$$

where $|\Psi_0\rangle_{2\mathrm{m}}$ is the initial state, see Fig. 4.1.

As previously mentioned, for $\Lambda > 0$ we can distinguish three regimes depending on the value of Λ, which from the perspective of phase space can be characterized by a different number and positions of fixed points [85, 90]. For $\Lambda \ll 1$ (Rabi regime) the

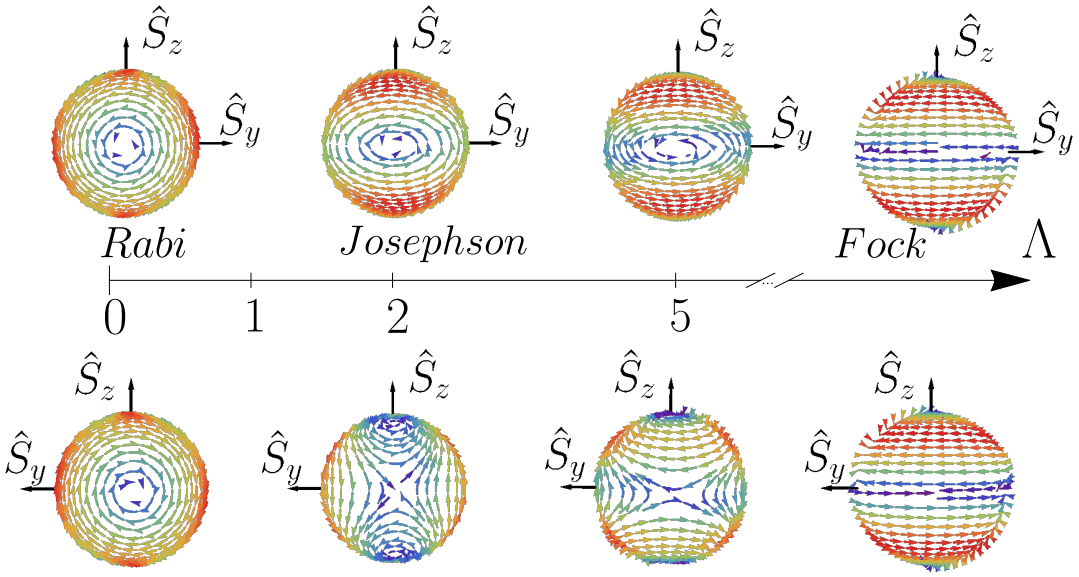

Figure 4.1: The classical mean-field phase space for the bimodal system for different values of Λ. The upper panels show the view from the positive side of x-axis, while the bottom panels show the view from the negative side. The three regimes are distinguished as discussed in the main text. Here we consider a case of $\Lambda = 2$ with the initial state located around an unstable fixed point at the negative side of x-axis.

linear term in Hamiltonian (4.5) dominates and, in the limit of $\Lambda \to 0$, the evolution is similar to resonant Rabi oscillations with N independent particles. The localization of the two stable center fixed points is given by points $(z, \varphi) = (0, 0)$ and $(z, \varphi) = (0, \pi)$. In the Josephson regime, at the bifurcation point $\Lambda = 1$, the fixed point localized at $(z, \varphi) = (0, \pi)$ becomes unstable and additionally we observe formation of two new stable fixed points at $(z, \varphi) = (\pm\sqrt{1 - \frac{1}{\Lambda^2}}, \pi)$. In the mean-field phase space, the bifurcation point is defined by the moment when the characteristic "∞" shape of trajectories centered around an unstable fixed point at $(z, \varphi) = (0, \pi)$ appears, see Fig. 4.1. For the Fock regime ($\Lambda \gg N^2$) the equations of motion reproduce the structure of the one-axis twisting (OAT) model [89], with two stable fixed points at $(z, \varphi) = (\pm 1, \varphi)$, and an unstable one at $(z, \varphi) = (0, \varphi)$.

The presence of the unstable saddle fixed point is characteristic for twisting evolution, such as given with the Hamiltonian (4.5). The saddle point is given at $(z, \varphi) = (0, \pi)$ and has great significance for our system. For example, if the initial coherent state is localized around the instability (Fig. 4.2(a)), it is therefore given by $|\phi, \theta\rangle_{2\mathrm{m}}$ with $\phi = \pi$ and $z = 0$, then the saddle fixed point squeezes the variance of the initial state of the spin component in the z-direction (Fig. 4.2(b)). The squeezed states are useful for quantum metrology as they allow us to overcome classical limits on sensitivity [88, 135]. Further evolution produces an over-squeezed state (as demonstrated in Fig. 4.2(c)), which on the phase portrait is represented by an elongated shape turning around the stable center fixed points. At this point, the state provides the highest sensitivity for an optimum interferometric protocol as we will prove later with numerical calculations. If the evolution continues beyond this point, the density function on the phase portrait breaks in half and the further evolution is represented by a superposition of two elongated shapes following the lines around stable points (Fig. 4.2(d)), until the moment when they merge again at the unstable fixed point. Although the sensitivity remains beyond the standard quantum limit, it diminishes

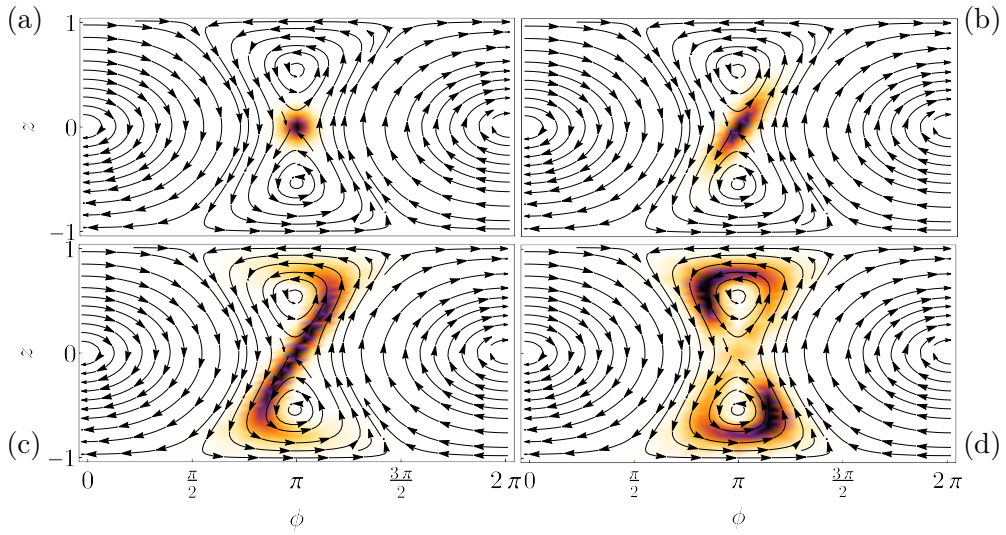

Figure 4.2: The classical mean-field phase space for the bimodal system (trajectories with arrows) with the Husimi function (colored areas) for the state in Eq. (4.9), calculated for $\Lambda = 1.5$ and $N = 100$. a) initial state localized at the unstable point $(z, \varphi) = (0, \pi)$ represented by $|\phi, \theta\rangle_{\mathrm{BI}}$ with $\phi = \pi$ and θ. b) the unitary evolution squeezes the state along z axis, and c) generates over-squeezed states curved around stable fixed points. d) further evolution brakes the Husimi function in half, and the two remaining parts merge later in the unstable fixed point.

over time.

We now shift from the two- to the three-mode case and note that a similar structure of the phase portrait can also be found in the spin-1 Bose-Einstein condensates. To demonstrate this, we introduce the symmetric and anti-symmetric bosonic annihilation operators [136], $\hat{g}_s = (\hat{a}_1 + \hat{a}_{-1})/\sqrt{2}$ and $\hat{g}_a = (\hat{a}_1 - \hat{a}_{-1})/\sqrt{2}$, and the corresponding pseudo-spin operators

$$\hat{J}_{x,\sigma} = \hat{a}_0^\dagger \hat{g}_\sigma + \hat{a}_0 \hat{g}_\sigma^\dagger, \tag{4.10a}$$

$$\hat{J}_{y,\sigma} = i(\hat{a}_0^\dagger \hat{g}_\sigma - \hat{a}_0 \hat{g}_\sigma^\dagger), \tag{4.10b}$$

$$\hat{J}_{z,\sigma} = \hat{g}_\sigma^\dagger \hat{g}_\sigma - \hat{a}_0^\dagger \hat{a}_0, \tag{4.10c}$$

where $\sigma = s$ and $\sigma = a$ refer to symmetric and anti-symmetric subspace, respectively. New operators have the following commutation relations, e.g. $[\hat{J}_{x,\sigma}, \hat{J}_{y,\sigma}] = 2i\hat{J}_{z,\sigma}$. We note that the symmetric subspace is spanned by the three operators

$$\{\hat{J}_{x,s}, \hat{J}_{y,s}, \hat{J}_{z,s}\} = \{\hat{J}_x, \hat{Q}_{yz}, \frac{1}{2}(\sqrt{3}\hat{Y} + \hat{D}_{xy})\}, \tag{4.11}$$

while the anti-symmetric subspace is spanned by the operators

$$\{\hat{J}_{x,a}, \hat{J}_{y,a}, \hat{J}_{z,a}\} = \{\hat{Q}_{zx}, \hat{J}_y, \frac{1}{2}(\sqrt{3}\hat{Y} - \hat{D}_{xy})\}. \tag{4.12}$$

The Hamiltonian (4.4) can be rewritten in terms of symmetric and anti-symmetric operators [136, 137] as

$$\begin{aligned}\frac{\hat{H}_{3\mathrm{m}}}{|c_2'|} &= -\frac{1}{2N}\hat{J}_{x,s}^2 + \frac{q}{3}\hat{J}_{z,s} - \frac{1}{2N}\hat{J}_{y,a}^2 + \frac{q}{3}\hat{J}_{z,a} + \\ &- \frac{1}{2N}\left(\hat{g}_s^\dagger\hat{g}_a + \hat{g}_a^\dagger\hat{g}_s\right)^2 \end{aligned} \tag{4.13}$$

up to the constant terms. The subscript "3m" denotes a three-mode system in this instance. The above Hamiltonian consists of two, non-commuting bimodal Hamiltonians for symmetric and anti-symmetric space, as in Eq. (3.19), rotated in respect to each other, with an extra mixing term coming from the $\hat{J}_z^2$ operator. Therefore, we expect that the mean-field phase space of the spinor system in each subspace is similar to the one in the BJJ condensate in Eq. (3.8). In the case of the spinor condensate, the mean-field phase space was already considered in [130]; nevertheless, here we are proposing a different approach.

We focus on the symmetric subspace spanned by the symmetric pseudo-spin operators $\hat{J}_{x,s}, \hat{J}_{y,s}, \hat{J}_{z,s}$. (For the anti-symmetric mean-field subspace, see App. A.) In order to obtain the structure of mean-field phase space we calculate the expectation value of Hamiltonian (4.4) on the spin coherent state defined for the symmetric subspace as

$$|\varphi,\theta\rangle_{3\mathrm{m}} = e^{-i\varphi\hat{J}_{z,s}/2}e^{-i\theta\hat{J}_{y,s}/2}|N0\rangle_s \tag{4.14}$$

where $|N0\rangle_s = \frac{\hat{g}_s^{\dagger N}}{\sqrt{N!}}|000\rangle$ and $\varphi \in (0, 2\pi)$, $\theta \in (0, \pi)$. This state is obtained by using a similar pattern to the one in the bimodal system given by Eq. (4.6). The spin coherent state in Eq. (4.14) can be rewritten as a double-rotated, maximally polarized state $|N0\rangle_s$ in the symmetric subspace, corresponding to the situation when all atoms are in the symmetric mode. The state $|N0\rangle_s$ is an eigenstate of $\hat{J}_{z,s}$, i.e. $\hat{J}_{z,s}|N0\rangle_s = N|N0\rangle_s$; on the Bloch sphere spanned by the symmetric subspace, it is located on the north pole. In terms of spin-1 operators the state reads $|N0\rangle_s \equiv e^{-i\pi/4\hat{Q}_{xy}}|N00\rangle$. On the south pole of the same Bloch sphere lies the state with N atoms in the $m_F = 0$ mode, $\frac{\hat{a}_0^{\dagger N}}{\sqrt{N!}}|000\rangle = |0N0\rangle$. Moreover, one can easily show that

$$|\varphi,\theta\rangle_{3\mathrm{m}} = \frac{1}{\sqrt{N!}}\left[\hat{g}_s^\dagger\cos\frac{\theta}{2} + \hat{a}_0^\dagger\sin\frac{\theta}{2}e^{i\varphi}\right]^N|000\rangle, \tag{4.15}$$

up to the phase factor. The state in Eq. (4.15) is a coherent spin state in symmetric subspace, similar to that defined in Eq. (3.20). The above expression can be used to illustrate an arbitrary state $|\Psi(t)\rangle$ on the Bloch sphere in the symmetric subspace using Q-function $Q_{3\mathrm{m}}(\varphi,\theta) = |\langle\Psi(t)|\varphi,\theta\rangle_{3\mathrm{m}}|^2$.

Following the pattern used for two-mode system, we calculate an average value of the Hamiltonian (4.4) on the spin coherent state given in Eq. (4.14). We obtain

$$H_{3\mathrm{m}} = \frac{\Lambda}{2}(1-z^2)\cos^2\varphi + z + 1, \tag{4.16}$$

where $z \equiv \cos\theta$ and $\Lambda = -2/q$. The equations of motion for conjugate variables (z, φ) are

$$\dot{\varphi} = -\Lambda z\cos^2\varphi + 1, \tag{4.17a}$$

$$\dot{z} = 2\Lambda(1-z^2)\cos\varphi\sin\varphi. \tag{4.17b}$$

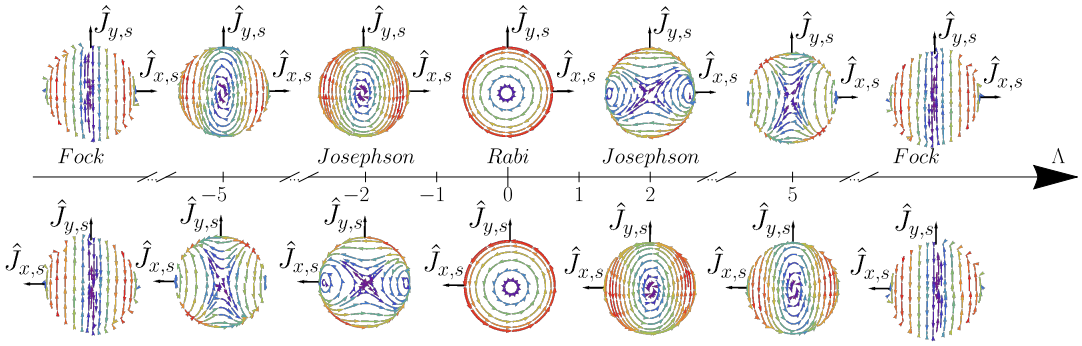

Figure 4.3: The structure of phase portraits of the spinor system versus Λ in the symmetric subspace. The upper panels show a view of the north poles of the Bloch sphere, while the bottom panels show a view of south poles. The structure is the same as the one for two-mode system, provided that the latter is rotated by $\pi/2$ around the y-axis. The three different regimes appear as well and are indicated above the Λ axis. In this chapter, we focus on $\Lambda = -2$ and the initial state located around the unstable saddle fixed point on the south pole of the Bloch sphere.

The position of fixed points can be found by solving $(\dot{z}, \dot{\varphi}) = (0, 0)$ and their stability can be determined, once again, from the stability matrix. To this end, we consider $\Lambda \geqslant 0$ without loss of generality. The positive value of parameter Λ recovers the same mean-field structure as in two-mode system, but rotated by $\pi/2$ around the $\hat{J}_{y,s}$ and $\hat{J}_{z,s}$ axes (see Fig. 4.3). Therefore, similarly to the BJJ, we can also distinguish three different regimes, depending on the value of Λ. In the Rabi regime ($\Lambda \to 0$) the evolution is dictated by the linear term, so two stable center fixed points are located at both poles of the Bloch sphere, i.e. $z = \pm 1$. This is true up to the point $\Lambda = -1$, where the bifurcation occurs. There, the point at $z = -1$ becomes unstable and two additional stable center fixed points appear at $(z, \varphi) = (-1/\Lambda, 0)$ and $(z, \varphi) = (-1/\Lambda, \pi)$. We observe the same "$\infty$" shape as in the two-mode counterpart. The Fock regime can be distinguished in the situation when the interaction term in Hamiltonian (4.4) dominates. We find two stable center fixed points at $(z, \varphi) = (0, \pi/2)$ and $(z, \varphi) = (0, 3\pi/2)$ and an unstable point along a meridian of the Bloch sphere at $\varphi = 0, \pi$.

In the next section we will quantify entanglement using quantum Fisher information (QFI), therefore we will focus on the Josephson regime for $\Lambda = \pm 2$, with the sign "$+$" for bimodal (two-mode) system and "$-$" for spinor (three-mode) system. The reason for this choice is the position of the unstable saddle fixed point, corresponding to the position of the initial states of interest to us.

4.2 Quantification of Entanglement

In this section we will quantify entanglement using the QFI in the interferometric protocol consisting of three steps: unitary evolution, phase imprinting and read-out measurement. In Chapter 2 we showed that the QFI is a witness for entanglement useful for quantum interferometry [138], so we will analyze the systems considered in this chapter from the same perspective.

The scheme starts with the unitary evolution of the initially prepared state

$$|\Psi(t)\rangle_k = \hat{U}_k(t)|\Psi_0\rangle_k, \text{ for } k = 2\text{m}, 3\text{m} \tag{4.18}$$

where $|\Psi_0\rangle_k$ is the initial state and the unitary evolution is given by $\hat{U}_{2\mathrm{m}}(t) = e^{-\frac{it\hat{H}_{2\mathrm{m}}}{\hbar}}$ for bimodal system and by $\hat{U}_{3\mathrm{m}}(t) = e^{-\frac{it\hat{H}_{3\mathrm{m}}}{\hbar}}$ for spin-1 system. The initial states for both systems are the spin coherent states in Eqs. (4.6) and (4.14) located around the unstable saddle fixed point and have the following form for two- and three-mode systems

$$|\Psi_0\rangle_{2\mathrm{m}} = |0, \pi/2\rangle_{2\mathrm{m}} \tag{4.19a}$$
$$|\Psi_0\rangle_{3\mathrm{m}} = |0, \pi\rangle_{3\mathrm{m}}. \tag{4.19b}$$

In the former case we have a coherent spin state given by Eq. (3.21). In the latter case, the state is equivalent to $|0, N, 0\rangle$, easily obtainable in the experiments, located on the south pole of the symmetric Bloch sphere.

In the next step the phase θ is imprinted on the system by a generic linear interferometric transformation $e^{-i\theta\hat{\Lambda}_{\mathbf{n}}}$, with $\hat{\Lambda}_{\mathbf{n}} = \mathbf{n} \cdot \hat{\mathbf{\Lambda}}$, where $\hat{\mathbf{\Lambda}}$ is a vector of generators spanning the bosonic $SU(2)$ Lie algebra for two-mode system: $\hat{\mathbf{\Lambda}}_{2\mathrm{m}} = \{\hat{S}_x, \hat{S}_y, \hat{S}_y\}$; or $SU(3)$ Lie algebra for the system of spinors: $\hat{\mathbf{\Lambda}}_{3\mathrm{m}} = \{\hat{J}_x, \hat{Q}_{yz}, \hat{J}_y, \hat{Q}_{zx}, \hat{D}_{xy}, \hat{Q}_{xy}, \hat{Y}, \hat{J}_z\}$ (see App. A). The unit vector $\mathbf{n}$ defines the direction of rotation axis. This interferometric transformation corresponds to the rotation on the generalized Bloch sphere and does not entangle the atoms. The output state of such transformation is then

$$|\Psi(\theta)\rangle_k = e^{-i\theta\hat{\Lambda}_{\mathbf{n},k}}|\Psi(t)\rangle_k, \text{ for } k = 2\mathrm{m}, 3\mathrm{m}. \tag{4.20}$$

The QFI sets the limit of the maximal possible precision of estimating the parameter θ in quantum interferometry [64] and is given by the quantum Cramér-Rao bound from Eq. (2.47):

$$\Delta\theta \geqslant 1/\sqrt{F_Q[|\Psi(\theta)\rangle, \hat{\Lambda}_{\mathbf{n}}]}. \tag{4.21}$$

In this case, the QFI value depends on the input state and generator of an interferometric rotation $\hat{\Lambda}_{\mathbf{n}}$ and for pure states is given by the variance of the generator

$$F_Q = 4\Delta^2\hat{\Lambda}_{\mathbf{n}}. \tag{4.22}$$

We recall two characteristic limits for the QFI value: the standard quantum limit (SQL) and the Heisenberg limit (HL). The SQL sets maximal precision for fully separable states, such as coherent states and is equal to N for spin-1/2 system and to $4N$ for spin-1 system [67]. In general, the QFI is limited by the variance of the generator of the interferometric transformation $F_Q \leqslant 4\Delta^2\hat{\Lambda}_{\mathbf{n}}$, which for separable states can be rewritten as $F_Q \leqslant N(h_{max} - h_{min})^2$, where h_{max} and h_{min} are the maximum and minimum eigenvalues of $\hat{\Lambda}_{\mathbf{n}}$, respectively. For qubits, and thus for any generator from $SU(2)$, $(h_{max} - h_{min}) = 1$, while in the case of qutrits (equivalent of qubits in spin-1 system) $(h_{max} - h_{min}) = 2$, hence the gain in the SQL for three-mode system. If the QFI value is greater than the SQL, then the state is entangled [139]. The latter limit bounds the QFI from above and, in the systems we consider here, is equal to N^2 for bimodal system and $4N^2$ for spinor system [67], where $4N^2$ is again a consequence of $F_Q \leqslant N^2(h_{max} - h_{min})^2$.

In order to maximize the QFI we have to optimize the rotation direction $\mathbf{n}$ of the generator $\hat{\Lambda}_{\mathbf{n}}$. Thus, we recall another definition of the QFI from Chapter 2, namely

$$F_Q[\hat{\rho}, \hat{\Lambda}_{\mathbf{n}}] = 4\mathbf{n}^T \cdot \Gamma[\hat{\rho}] \cdot \mathbf{n}, \tag{4.23}$$

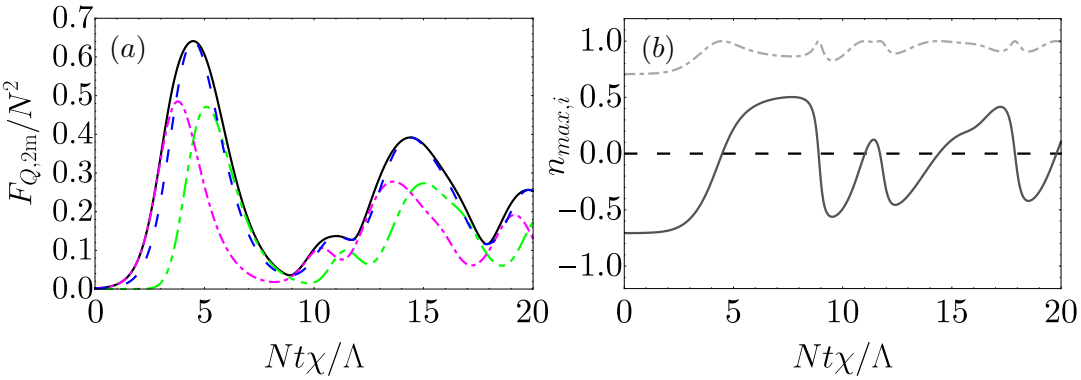

Figure 4.4: (*a*) The QFI (black solid line) calculated with Eq. (4.25) for $N = 600$. Color lines correspond to variance multiplied by 4 of the following generators: $\hat{\Lambda}_{\mathbf{n}} = (\hat{S}_z - \hat{S}_y)/\sqrt{2}$ (purple dash-dotted line), $\hat{\Lambda}_{\mathbf{n}} = (\hat{S}_z + \hat{S}_y)/\sqrt{2}$ (green dash-double-dotted line) and $\hat{\Lambda}_{\mathbf{n}} = \hat{S}_z$ (blue dashed line). (*b*) Plots of the optimal direction of interferometric rotation $\mathbf{n}_{max}$, i.e. i-th component of the eigenvector of the covariance matrix in Eq. (4.24) corresponding to $\lambda_{\mathrm{max,2m}}$. The x component is presented with the black dashed line, y with the dark gray solid line and z with the light gray dash-dotted line.

with the covariance matrix $\Gamma[\hat{\rho}]$ defined as

$$\Gamma_{i,j}[\hat{\rho}] = \frac{1}{2}\sum_{k,l}\frac{(v_k - v_l)^2}{v_k + v_l} Re\left[\langle k|\hat{\Lambda}_i|l\rangle\langle l|\hat{\Lambda}_j|k\rangle\right], \tag{4.24}$$

where we used the eigenvalues and the eigenvectors of the input density matrix $\hat{\rho} = \sum_k v_k|k\rangle\langle k|$. The optimal direction of the interferometric transformation can be found by diagonalization of the covariance matrix. It corresponds to the eigenvector of the largest eigenvalue λ_{max}, which at the same time maximizes the QFI as $F_Q = 4\lambda_{max}$.

For bimodal system the covariance matrix has 9 elements built from the operators in vector $\hat{\mathbf{\Lambda}}_{\mathrm{2m}}$. The QFI corresponding to two-mode system is then

$$F_{Q,\mathrm{2m}} = 4\lambda_{\mathrm{max,2m}}, \tag{4.25}$$

where by λ_{max} we denote the largest eigenvalue of the covariance matrix. The eigenvalue and thus the generator of the interferometric rotation can be found analytically for the Hamiltonian (4.5) without coupling ($\Omega = 0$) [140, 141]. Otherwise, we have to perform numerical analysis. In Fig. 4.4(*a*) we plot the QFI (black solid line) given by Eq. (4.25), and the variance of different linear generators multiplied by 4: $\hat{\Lambda}_{\mathbf{n}} = (\hat{S}_z - \hat{S}_y)/\sqrt{2}$ (purple dash-dotted line), $\hat{\Lambda}_{\mathbf{n}} = (\hat{S}_z + \hat{S}_y)/\sqrt{2}$ (green dash-double-dotted line) and $\hat{\Lambda}_{\mathbf{n}} = \hat{S}_z$ (blue dashed line). Initially the optimal generator is given by linear combination of $\hat{\Lambda}_{\mathbf{n}} = (\hat{S}_z - \hat{S}_y)/\sqrt{2}$ indicated by the purple dash-dotted line, which corresponds to the direction of twisting in the mean-field phase portrait. When the state is over-squeezed, the variance of this generator no longer corresponds to the maximal value of the QFI as the direction of optimal generator changes, see Fig. 4.4(*b*). In the real experiment such an optimization in time may be difficult, if not impossible. Consequently, one may look for a simple, efficient generator for which the variance does not necessarily saturate the maximized QFI. In this case $\hat{\Lambda}_{\mathbf{n}} = \hat{S}_z$ can be considered a good generator as its variance is slightly lower than the variance of the optimal generator. Moreover, for the maximal value of the QFI we see that the variance of $\hat{\Lambda}_{\mathbf{n}} = \hat{S}_z$ saturates the QFI, i.e. $F_Q = 4\Delta^2\hat{S}_z$.

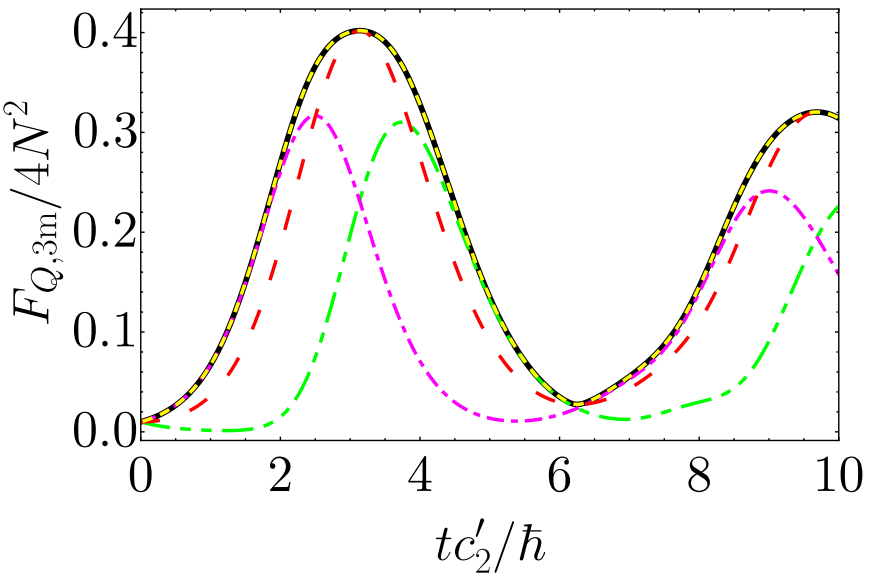

Figure 4.5: Optimal generators of interferometric rotation $\hat{\Lambda}_{S,ij}$ for spinor system with fixed magnetization calculated for $N = 100$ atoms. Black solid line represents the QFI optimalized over all directions $\mathbf{n}$. The corresponding values of the QFI for a given generator derived in the main text are given with: $F_{Q,3m} = 4\Delta^2\hat{\Lambda}_{\mathbf{n},s}$ (which equals to $4\hat{\Lambda}_{\mathbf{n},a}$) (yellow dashed line), $F_{Q,3m} = 4\Delta^2\hat{\Lambda}_{\mathbf{n},5}$ (brown thin dashed line) and $F_{Q,3m} = 4\Delta^2\hat{\Lambda}_{\mathbf{n},7}$ (thin blue line). Additionally we plot QFI for generators: $\hat{\Lambda}_{\mathbf{n}} = \hat{J}_x$ (red dashed line), $\hat{\Lambda}_{\mathbf{n}} = \frac{1}{\sqrt{2}}(\hat{J}_{x,s} - \hat{J}_{y,s})$ and $\hat{\Lambda}_{\mathbf{n}} = \frac{1}{\sqrt{2}}(\hat{J}_{xa} + \hat{J}_{ya})$ (purple dash-dotted and green dash-double-dotted lines, respectively). We note that the QFI value for short-time evolution is saturated by $4\Delta^2\left(\frac{\hat{J}_{xs}-\hat{J}_{ys}}{\sqrt{2}}\right)$.

For spinors, vector $\hat{\mathbf{\Lambda}}_{3m}$ has 8 elements, and therefore the optimal direction of the interferometric rotation is determined from the 8×8 covariance matrix – the largest eigenvalue $\lambda_{\max,3m}$ of which corresponds to the QFI

$$F_{Q,3m} = 4\lambda_{\max,3m}. \tag{4.26}$$

Although there are 64 elements in the covariance matrix, only a few of them are non-zero. This is because of the constant magnetization, which introduces the symmetry of the covariance matrix and simplifies its form to a diagonal structure:

$$\Gamma = \Gamma_s \oplus \Gamma_a \oplus [\Gamma_{55}] \oplus [\Gamma_{55}] \oplus [\Gamma_{77}] \oplus [0], \tag{4.27}$$

where

$$\Gamma_s = \begin{pmatrix} \Gamma_{11} & \Gamma_{12} \\ \Gamma_{12} & \Gamma_{22} \end{pmatrix}, \quad \Gamma_a = \begin{pmatrix} \Gamma_{11} & -\Gamma_{12} \\ -\Gamma_{12} & \Gamma_{22} \end{pmatrix}. \tag{4.28}$$

As a result, the possible generators can be found analytically:

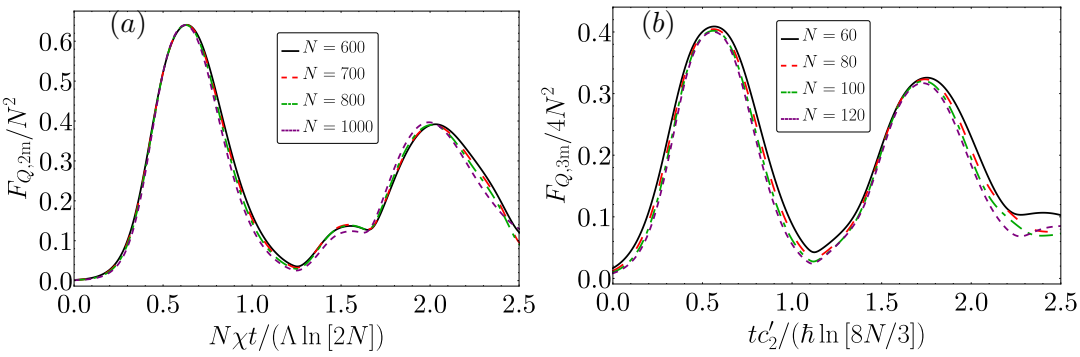

Figure 4.6: The scaling of the QFI with N as a function of time for bimodal (a) and spinor (b) systems with $|\Lambda| = 2$. The values of N are given in the legend.

$$\hat{\Lambda}_{\mathbf{n},s} = \frac{\hat{J}_x - \gamma_{12}\hat{Q}_{yz}}{\sqrt{1+\gamma_{12}^2}}, \tag{4.29}$$

$$\hat{\Lambda}_{\mathbf{n},a} = \frac{\hat{Q}_{zx} + \gamma_{34}\hat{J}_y}{\sqrt{1+\gamma_{34}^2}}, \tag{4.30}$$

$$\hat{\Lambda}_{\mathbf{n},5} = \hat{D}_{xy}, \tag{4.31}$$

$$\hat{\Lambda}_{\mathbf{n},7} = \hat{Y}, \tag{4.32}$$

where $\gamma_{ij} = (\Gamma_{jj} - \Gamma_{ii} - \sqrt{(\Gamma_{ii}-\Gamma_{jj})^2 + 4\Gamma_{ij}})/(2\Gamma_{ij})$ and the subscripts $s, a, 5$ and 7 denote generators set by eigenvectors of the largest eigenvalue in blocks $\Gamma_s, \Gamma_a, \Gamma_{55}$ and Γ_{77}, respectively. The numerical calculations of the variances of these generators [109], compared to the QFI, are plotted in Fig. 4.5. We observe that the optimal generator is the one given by $\hat{\Lambda}_{\mathbf{n},s}$ or $\hat{\Lambda}_{\mathbf{n},a}$, as both correspond to equal eigenvalues. We also plot variance multiplied by 4 of generators such as: $\hat{\Lambda}_{\mathbf{n}} = \frac{\hat{J}_{x,s}-\hat{J}_{y,s}}{\sqrt{2}}$ (purple dash-dotted line) which saturates the QFI for short-time evolution, $\hat{\Lambda}_{\mathbf{n}} = \hat{J}_{x,s}$ (red dashed line) which saturates the QFI at its maximum and $\hat{\Lambda}_{\mathbf{n}} = \frac{\hat{J}_{x,a}-\hat{J}_{y,a}}{\sqrt{2}}$ (green dashed-double-dotted line) which saturates the QFI after the first maximum. We observe an analogy to the two-mode system, where $\hat{S}_z$, here $\hat{J}_x$, is a simple, efficient generator providing high value of the QFI close to the maximum. The direction of both generators, $\hat{S}_z$ and $\hat{J}_x$, is perpendicular to the direction along which the unstable saddle fixed point is localized. In addition, for both systems, the linear combination of generators, $\frac{1}{\sqrt{2}}(\hat{S}_x - \hat{S}_y)$ for spin-1/2 and $\frac{1}{\sqrt{2}}(\hat{J}_{x,s} - \hat{J}_{y,s})$ for spin-1 system, maximize the QFI for short-time evolution.

4.2.1 Scaling of the QFI

Comparing the maximized QFI for both two-mode and three-mode systems, we observe the initial growth of the QFI up to the point where the system is over-squeezed. The QFI in this region exhibits scaling with a number of particles, provided that the time axis is properly re-scaled as $Nt/\ln(2N)$ for bimodal system (Fig. 4.6(a)), and as $t/\ln(8N/3)$ for spinor system (Fig. 4.6(b)) corresponding to the time scaling of the first maximum. (We prove this in the remaining part of this section.) On both plots the QFI is calculated for the case of Josephson regime, $|\Lambda| = 2$, the reason being that for two-mode system the presence of the linear coupling in the Hamiltonian (4.5)

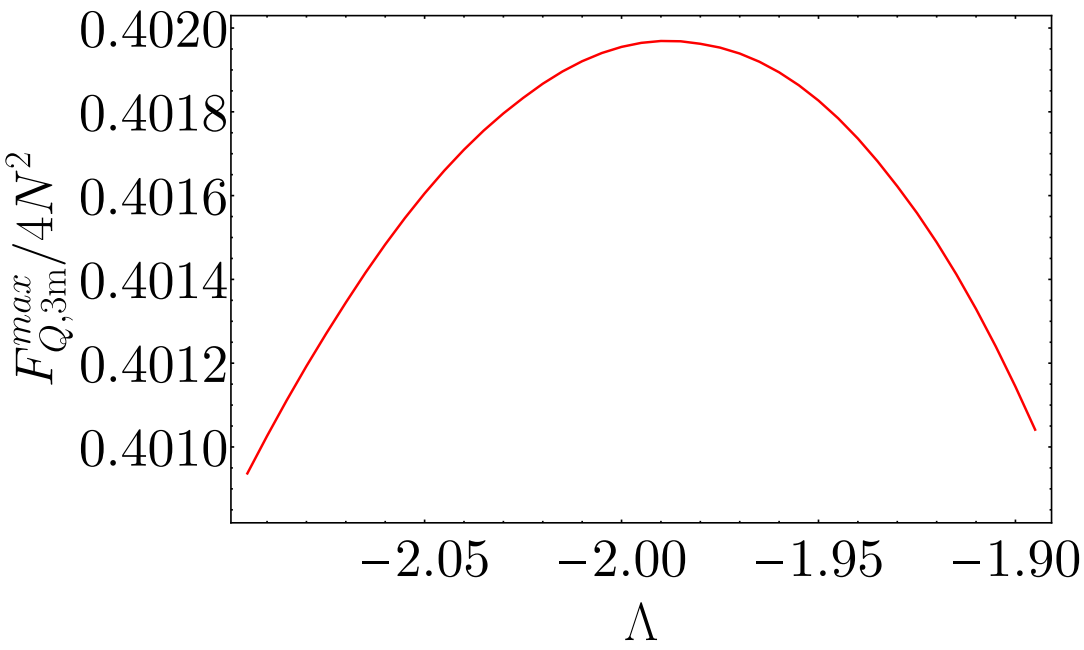

Figure 4.7: The maximized QFI for spinor system $F^{max}_{\mathrm{Q,3m}}$ as a function of Λ for $N = 100$. We demonstrate that the maximal entanglement is generated for $\Lambda \simeq -2$.

accelerates creation of atom entanglement in respect to the OAT model (where coupling is not present). It has been shown that the optimal evolution is obtained for $|\Lambda| = 2$ [142] due to the fact that the angle between in- and out-going constant energy lines in the mean-field phase space is equal to $\pi/4$ [142, 143]. Therefore, based on the similarities of the mean-field phase portrait in three-mode system, we expect that this also holds true for spinor condensates. In Fig. 4.7 we see that indeed the maximal QFI is obtained for entangled states generated for $\Lambda \approx -2$.

The initial states considered here are located around an unstable fixed point. The scaling of the QFI for short-time evolution can be explained using a theory developed in [144, 145]. We start with the two-mode system. In the first step we rotate the Hamiltonian (4.5) around the x-axis of the Bloch sphere through $\pi/4$, since the angle between the outgoing constant energy lines in the saddle fixed point and z-axis for $\Lambda = 2$ is close to $\pi/4$. The transformation corresponds to the same rotation of the mean field phase portrait, and as a result the outgoing trajectories lie along the y-axis. Therefore, the largest fluctuations (that determine the QFI value) are located along the y-axis. Next, we introduce a small parameter $\varepsilon = 1/N$ and with its use we transform the spin components as follows: $\hat{h}_j = \sqrt{\varepsilon}\hat{S}_j$. The commutation relations now read $[\hat{h}_i, \hat{h}_j] = i\sqrt{\varepsilon}\hat{h}_k\epsilon_{ijk}$ and the rotated Hamiltonian (4.5) in the language of the transformed spin components now reads

$$\hat{\tilde{H}}_{2\mathrm{m}} = \frac{1}{\sqrt{\varepsilon}}\left(\hat{h}_z^2 + \hat{h}_y^2 + \hat{h}_z\hat{h}_y + \hat{h}_y\hat{h}_z - a\hat{h}_x\right), \tag{4.33}$$

where $a = 2\varepsilon\Omega/\chi$, the energy unit is set to $\hbar\chi/(2\sqrt{\varepsilon})$ and so the dimensionless time is given by $\tau = \chi t/(2\sqrt{\varepsilon})$. We calculate the Heisenberg equation of motion for the operators of spin components, i.e. $i\partial_t\hat{h}_i = [\hat{h}_i, \tilde{H}_{2\mathrm{m}}]$. The expectation values of the first-order operator involve the terms of the first-order $\left\langle \hat{h}_i \right\rangle$ and the second-order moments $\left\langle \hat{h}_i\hat{h}_j \right\rangle$, while the time evolution of the second-order moments is governed

by the second-order and the third-order moments $\left\langle \hat{h}_i\hat{h}_j\hat{k} \right\rangle$, and so on. This is the Bogoliubov-Born-Green-Kirkwood-Yvon (BBGKY) hierarchy of equations of motion for the expectation values of the products of operators [146]. To solve the set of equations of motions, the hierarchy needs to be truncated in order to obtain a closed set of equations. We keep the first-order and the second-order moments and truncate the BBGKY hierarchy by using the following approximation for the third-order moments:

$$\begin{aligned}\langle \hat{h}_i\hat{h}_j\hat{h}_k\rangle \simeq \langle \hat{h}_i\hat{h}_j\rangle\langle \hat{h}_k\rangle + \langle \hat{h}_j\hat{h}_k\rangle\langle \hat{h}_i\rangle + \langle \hat{h}_k\hat{h}_i\rangle\langle \hat{h}_j\rangle \\ - 2\langle \hat{h}_i\rangle\langle \hat{h}_j\rangle\langle \hat{h}_k\rangle. \end{aligned} \tag{4.34}$$

With this approximation we obtain the equations of motion for expectation values $s_j = \langle \hat{h}_j\rangle$ and for the second-order moments $\delta_{jk} = \langle \hat{h}_j\hat{h}_k + \hat{h}_k\hat{h}_j\rangle - 2\langle \hat{h}_j\rangle\langle \hat{h}_k\rangle$, as follows:

$$\dot{s}_x = (\delta_{zz} - \delta_{yy}), \tag{4.35}$$

$$\dot{\delta}_{zz} = -4\delta_{zz}s_x - 2a\delta_{yz}, \tag{4.36}$$

$$\dot{\delta}_{yy} = 4\delta_{yy}s_x + 2a\delta_{yz}. \tag{4.37}$$

The initial conditions can be obtained by calculating averages for the spin coherent state $|0, \pi/2\rangle_{2\mathrm{m}}$ at $\tau = 0$. We obtain: $s_x(0) = 1/(2\sqrt{\varepsilon})$ and $\delta_{zz}(0) = \delta_{yy}(0) = 1/2$.

Eq. (4.36) is a non-homogeneous differential equation for which the solution of the homogeneous part ($a \to 0$) is $\delta_{zz}(\tau) = \delta_{zz}(0)e^{-f(\tau)}$ with $f(\tau) = 4\int_0^\tau s_x(t)dt$. The analysis of the full equation can be performed assuming $\delta_{zz}(\tau) = C(\tau)e^{-f(\tau)}$ with $C(\tau) = C(0) - a\int_0^\tau \delta_{yz}(t)e^{f(t)}dt = \delta_{zz}(0) + \Phi(\tau)$. The time dependent part of the amplitude $\Phi(\tau)$ can be neglected for two reasons. Firstly, $\Phi(\tau)$ is of the order of the parameter ε. Secondly, for the short-time expansion we have $\Phi(\tau) \simeq \Phi(0) + \dot{\Phi}(0)\tau = 0$ since $\delta_{yz}(0) = 0$. Therefore, for the short times of evolution, the solution of Eq. (4.36) can be well approximated by the homogeneous solution. Analogical reasoning can be applied to the analysis of Eq. (4.37). As a result we obtain $\delta_{yy}(\tau) = \delta_{yy}(0)e^{f(\tau)}$. Finally, Eq. (4.35) takes the form

$$\dot{s}_x(\tau) = -\sinh\left[f(\tau)\right]. \tag{4.38}$$

It has an analytical solution when the function $f(\tau)$ is expanded into the Taylor series up to the first order: $f(\tau) \simeq f(0) + \dot{f}(0)\tau$. The self-consistency condition gives $f(0) = 0$ and $\dot{f}(0) = 4s_x(0)$. Therefore, the approximated solution of Eq. (4.38) takes the form [143]

$$s_x(\tau) = s_x(0) - \frac{\cosh(4s_x(0)\tau) - 1}{4s_x(0)}. \tag{4.39}$$

As a result δ_{zz}, and thus using the same pattern for δ_{yy}, can be calculated

$$\delta_{yy} = \delta_{yy}(0)e^{4s_x(0)\tau - \frac{\sinh(4s_x(0)\tau) - 4s_x(0)\tau}{[4s_x(0)]^2}}. \tag{4.40}$$

Since $s_y(0) = 0$ for a given initial state, the maximum of the QFI in the language of transformed spin operators is given by

$$F_{Q,2\mathrm{m}}(\tau) \simeq 4\Delta^2\hat{S}_y \simeq \frac{2}{\varepsilon}\delta_{yy}(\tau). \tag{4.41}$$

The maxima of Eq. (4.41) can be found at $\chi t_{max} \simeq \ln(2N)/N$. Thus, we can calculate the value of the QFI at t_{max} and obtain that $F^{max}_{Q,2\mathrm{m}} \simeq \frac{2}{e}\frac{1}{\varepsilon^2} \approx 0.7N^2$ which corresponds

to the maximum observed in Fig. 4.6(a).

The same analysis can be applied to the spinor system. First, we rotate the spin-1 Hamiltonian (4.4) around the $\hat{J}_{z,s}$ by $\pi/8$ angle. The reason is to locate the constant energy lines along the $\hat{J}_{y,s}$ axis of the Bloch sphere in the symmetric subspace; however, the angle is half of the angle in the bimodal case because of the factor 2 in the commutation relations, i.e. $[\hat{J}_{i,s}, \hat{J}_{j,s}] = i2\hat{J}_{k,s}\epsilon_{ijk}$. Then, following the pattern from the two-mode system, we introduce the small parameter $\varepsilon = 1/N$ which transforms the spin components into $\hat{h}_j = \sqrt{\varepsilon}\hat{J}_j$ and $\hat{q}_j = \sqrt{\varepsilon}\hat{Q}_j$. The rotated and re-scaled Hamiltonian is given with

$$\hat{\tilde{H}}_{3\mathrm{m}} = -\frac{1}{\sqrt{\varepsilon}}\left[\frac{1}{2}\left(\hat{h}_{x,s}+\hat{h}_{y,s}\right)^2 + \left(\hat{h}_{y,a}\cos\frac{\pi}{8} + \hat{h}_{z,a}\sin\frac{\pi}{8}\right)^2 + \left(\hat{h}_z\cos\frac{\pi}{8} + \hat{q}_{xy}\sin\frac{\pi}{8}\right)^2 + a\hat{n}_0 - a\hat{n}\right], \tag{4.42}$$

where $\hat{n}_0 = \sqrt{\varepsilon}\hat{N}_0$, $\hat{n} = \sqrt{\varepsilon}\hat{N}$, $a = 2q/\varepsilon$. The energy unit in this case is $\sqrt{\varepsilon}|c_2'|/2$ and the dimensionless time $\tau = \sqrt{\varepsilon}t|c_2'|/2\hbar$.

The Heisenberg equations of motion of the spin components in Hamiltonian (4.42), truncated at the third order according to Eq. (4.34) and setting $s_j = \left\langle \hat{h}_j \right\rangle$, have the following form

$$\dot{s}_{zs} = -(\delta_{ys,ys} - \delta_{xs,xs}) - \frac{\sqrt{2}}{4}(\delta_{ya,ya} - \delta_{xa,xa}), \tag{4.43a}$$

$$\dot{\delta}_{xs,xs} = -2\delta_{xs,xs}s_{zs} - a\delta_{xs,ys}, \tag{4.43b}$$

$$\dot{\delta}_{ys,ys} = 2\delta_{ys,ys}s_{zs} + a\delta_{xs,ys}, \tag{4.43c}$$

for symmetric operators, and

$$\dot{s}_{za} = -\frac{1}{2}(\delta_{ys,ys} - \delta_{xs,xs}) - \frac{\sqrt{2}}{2}(\delta_{ya,ya} - \delta_{xa,xa}), \tag{4.44a}$$

$$\dot{\delta}_{xa,xa} = -\sqrt{2}\delta_{xa,xa}s_{za} - a\delta_{xa,ya}, \tag{4.44b}$$

$$\dot{\delta}_{ya,ya} = \sqrt{2}\delta_{ya,ya}s_{za} + a\delta_{xa,ya}, \tag{4.44c}$$

for anti-symmetric operators. (The commutation relations between any of the $SU(3)$ operators can be found in Table A.1 in Appendix A.) The initial conditions for the above sets of equations can be calculated on the spin coherent state $|0,\pi\rangle_{3\mathrm{m}}$ giving: $s_{z\sigma}(0) = -1/\sqrt{\varepsilon}$ and $\delta_{x\sigma,x\sigma}(0) = \delta_{y\sigma,y\sigma}(0) = 1$ for $\sigma = s, a$. We neglected some terms in the Eqs. (4.43) and (4.44), such as $\delta_{z,z}$ and $\delta^q_{xy,xy}$, since their initial average values are 0, and remain insignificant in latter times. The equations for symmetric and anti-symmetric operators are similar to those in the bimodal case. However, there are two differences: (i) $s_{z\sigma}$ (with $\sigma = s, a$) in Eqs. (4.43a) and (4.44a) play the role of s_x in Eq. (4.35) and (ii) symmetric and anti-symmetric subspaces are coupled to each other in Eqs. (4.43a) and (4.44a). By following the analysis from the two-mode

system we obtain

$$s_{zs}(\tau) = s_{zs}(0) - \\ - \frac{\cosh(2s_{zs}(0)\tau) - 1}{2s_{zs}(0)} - \frac{\sqrt{2}}{4}\frac{\cosh(\sqrt{2}s_{za}(0)\tau) - 1}{\sqrt{2}s_{za}(0)}, \tag{4.45}$$

$$s_{za}(\tau) = s_{za}(0) - \\ - \frac{1}{2}\frac{\cosh(2s_{zs}(0)\tau) - 1}{2s_{zs}(0)} - \frac{\sqrt{2}}{2}\frac{\cosh(\sqrt{2}s_{za}(0)\tau) - 1}{\sqrt{2}s_{za}(0)}. \tag{4.46}$$

Please note: the coupling of the symmetric and anti-symmetric subspaces persists and has to be taken into account while explaining the scaling of $\delta_{x\sigma,x\sigma}$; thus, we need to calculate time derivatives of both variances in order to express the relation between cosh functions with different arguments. As a result, we find that the maximum of the QFI can be approximated by

$$F_{Q,3\mathrm{m}} \simeq 4\Delta^2 \hat{J}_{xs} \approx \frac{1}{\varepsilon}\delta_{xs,xs}(\tau). \tag{4.47}$$

Once again, we search for the extremum of the expression (4.47) and find that the maximum of the QFI occurs when $|c_2'|t_{max}/\hbar = \ln(8N/3)$. The value of the QFI calculated for t_{max} gives $F_{Q,3\mathrm{m}} \simeq \frac{16}{3}e^{-2/3}N^2 \approx 2.8N^2$. Although the results for spinor condensate do not exactly agree with numerical calculations, the results recover the time scaling and Heisenberg scaling of the QFI. The discrepancy may be an effect of neglecting some terms in the Eqs. (4.43) and (4.44) that would impact the relation between the "cosh" functions.

In the next section we will provide an efficient measurement that can be used to obtain phase estimation at the level of the optimal generator $\hat{\Lambda}_{\mathbf{n}}$.

4.3 Efficient Measurement

The uncertainty of estimation of the parameter θ can be obtained using the signal-to-noise ratio from the method of moments in Eq. (2.36) as

$$\Delta\theta^2 = \frac{\Delta^2\hat{\mathcal{S}}}{|\partial_\theta \left\langle \hat{\mathcal{S}} \right\rangle|^2} \tag{4.48}$$

where $\Delta^2\hat{\mathcal{S}} = \left\langle \hat{\mathcal{S}}^2 \right\rangle - \left\langle \hat{\mathcal{S}} \right\rangle^2$ is the variance of the signal $\hat{\mathcal{S}}$ representing the choice of measurement. In general, the precision of the estimation of parameter θ is limited by the quantum Cramér-Rao bound:

$$\frac{1}{\Delta\theta^2} \leq F_Q. \tag{4.49}$$

Although the QFI gives the maximal possible precision, its measure requires complete tomography of the state [147]. The inverse of the signal-to-noise ratio is less sensitive to the change of the parameter θ; nevertheless, this method requires measurement of the first and second moments of the observable $\hat{\mathcal{S}}$, which in some special cases can saturate Eq. (4.49). In general, a recipe for finding a good measurement $\hat{\mathcal{S}}$ does not exist. Nevertheless, in some cases optimal $\hat{\mathcal{S}}$ is known, like the parity operator for the Greenberger-Horne-Zeilinger (GHZ) state [148, 149] or $\hat{J}_z^2$ for the spinor system [110]. Also, the nonlinear squeezing parameter was recently proposed [150] to

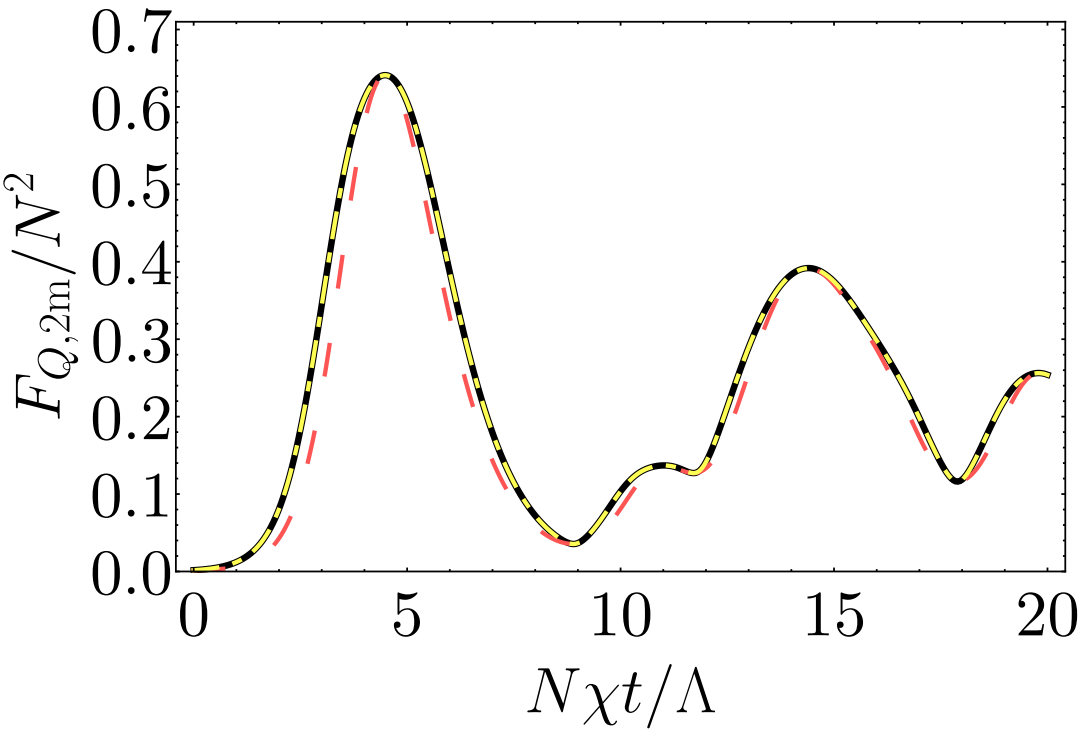

Figure 4.8: The QFI (black solid line) calculated using maximal eigenvalue of the covariance matrix from Eq. (4.24) in bimodal system. The inverse of the signal-to-noise ratio of the parity measurement $\hat{\mathcal{S}} = \hat{\mathcal{P}}_{2\mathrm{m}} = (-1)^{N/2-\hat{S}_x}$, with generator $\hat{\Lambda}_{\mathbf{n}_{max}}$ given by: the eigenvector corresponding to $\lambda_{max,2\mathrm{m}}(t)$ (yellow dash-dotted line) and $\hat{S}_z$ (red dashed line). Numerical calculations performed for $N = 600$.

saturate the QFI for short-time evolution for bimodal condensates. However, it requires the measurements of higher order moments and correlations. In the systems we are considering here, we will show that the parity operator provides sensitivity with Heisenberg scaling. The parity is a well-defined observable in quantum mechanics and its measurement is useful for quantum metrology [147, 151] in both the optical and atomic domains for non-Gaussian quantum states. It remains an experimental challenge due to the requirement of a single atom resolution, nevertheless it has been partially demonstrated experimentally [152–159].

We start by considering the two-mode system. We consider a parity operator of a form $\hat{\mathcal{P}}_{2\mathrm{m}} = (-1)^{S-\hat{S}_x} = (-1)^{N/2-\hat{S}_x}$ used in [150] as an optimal measurement for non-Guassian states, which commutes with the Hamiltonian (4.5), $\left[\hat{\mathcal{P}}_{2\mathrm{m}}, \hat{H}_{2\mathrm{m}}\right] = 0$. The initial state given in Eq. (4.19a) is the eigenstate of $\hat{\mathcal{P}}_{2\mathrm{m}}$, i.e. $\hat{\mathcal{P}}_{2\mathrm{m}}|\Psi_0\rangle_{2\mathrm{m}} = |\Psi_0\rangle_{2\mathrm{m}}$, and consequently $\hat{\mathcal{P}}_{2\mathrm{m}}|\Psi(t)\rangle_{2\mathrm{m}} = |\Psi(t)\rangle_{2\mathrm{m}}$. Additionally, we have $\hat{\Lambda}_{\mathbf{n}_{max}}\hat{\mathcal{P}}_{2\mathrm{m}} = -\hat{\mathcal{P}}_{2\mathrm{m}}\hat{\Lambda}_{\mathbf{n}_{max}}$, where $\hat{\Lambda}_{\mathbf{n}_{max}}$ is the $SU(2)$ generator maximizing the QFI. This relation also holds for the general generators of the form $\hat{\Lambda}_{\mathbf{n}} = a\hat{S}_z + b\hat{S}_y$, where $a^2 + b^2 = 1$.

Considering these properties we can calculate precision of the phase estimation given with Eq. (4.48). Firstly, we expand the expectation value of the parity operator on the state with the accumulated phase, $|\psi(\theta)\rangle_{2\mathrm{m}}$, up to the leading terms in θ

$$ {}_{2\mathrm{m}}\langle\psi(\theta)|\hat{\mathcal{P}}_{2\mathrm{m}}|\psi(\theta)\rangle_{2\mathrm{m}} = 1 - 2\theta^2\,{}_{2\mathrm{m}}\langle\psi(t)|\hat{\Lambda}^2_{\mathbf{n}_{max}}|\psi(t)\rangle_{2\mathrm{m}} + 0(\theta^3), \tag{4.50} $$

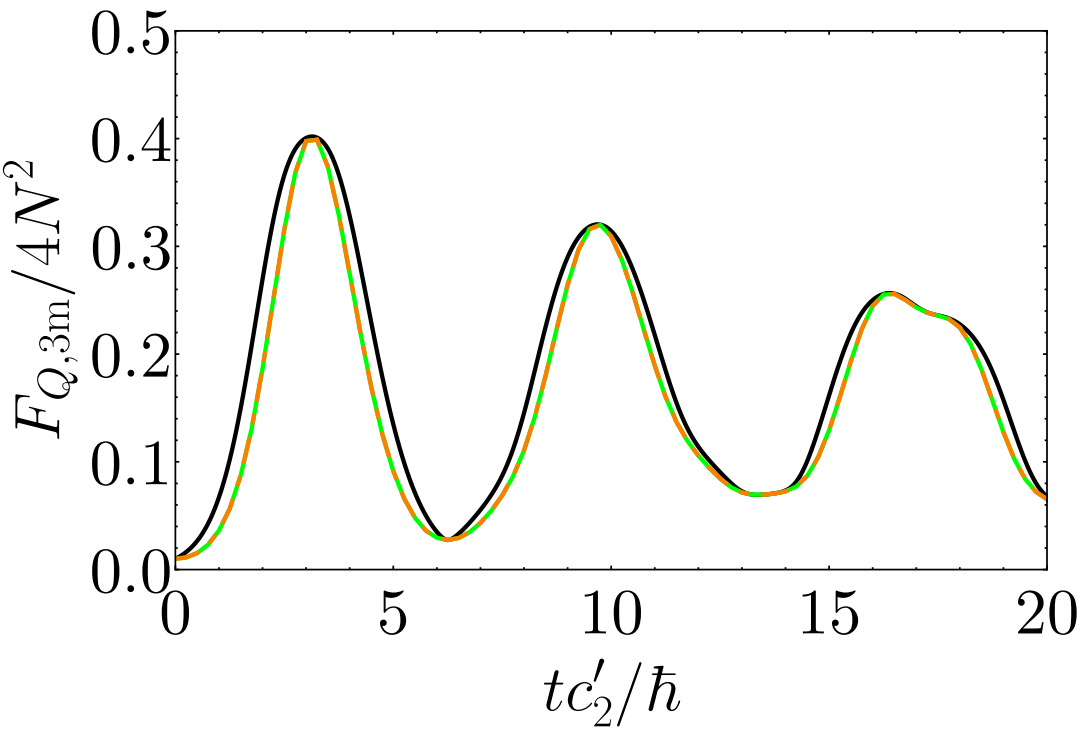

Figure 4.9: The QFI (black solid line) calculated using maximal eigenvalue of the covariance matrix from Eq. (4.24) in spinor system. The inverse of the signal-to-noise ratio of the parity measurement $\hat{\mathcal{S}} = \hat{\mathcal{P}}_{3m} = (-1)^{N-\hat{J}_{z,s}}$ (green double-dotted line) and $\hat{J}_z^2$ (orange dashed line), with $\hat{\Lambda}_{\mathbf{n}} = \hat{J}_x$. Numerical calculations performed for $N = 100$.

and thus the variance can be expressed as

$$\Delta^2\hat{\mathcal{P}}_{2m} = 4\theta^2\langle\hat{\Lambda}^2_{\mathbf{n}_{max}}\rangle + 0(\theta^3), \tag{4.51}$$

since $\langle\hat{\mathcal{P}}^2_{2m}\rangle = 1$. Then, we perform the same expansion of the derivative, namely

$$\partial_\theta\langle\hat{\mathcal{P}}_{2m}\rangle = -4\theta\langle\hat{\Lambda}^2_{\mathbf{n}_{max}}\rangle + 0(\theta^2). \tag{4.52}$$

Finally, using Eqs. (4.51) and (4.52) in the precision given by Eq. (4.48), we arrive with a formula

$$\Delta\theta^{-2}|_{\theta=0} = 4\Delta^2\hat{\Lambda}_{\mathbf{n}_{max}}, \tag{4.53}$$

which saturates the QFI due to the fact that $\left\langle\hat{\Lambda}_{\mathbf{n}_{max}}\right\rangle = 0$.

We plot the results in Fig. 4.8 choosing the optimal generator $\hat{\Lambda}_{\mathbf{n}_{max}}$ numerically as the eigenvector of the highest eigenvalue of the state at given moment t (yellow dash-dotted line) and simpler one given by $\hat{\Lambda}_{\mathbf{n}} = \hat{S}_z$ (red dashed line). Indeed, we observe that the parity operator is the optimal choice to saturate the QFI.

The same procedure can be performed for the spin-1 system with the parity operator chosen as $\hat{\mathcal{P}}_{3m} = (-1)^{J-\hat{J}_{z,s}} = (-1)^{N-\hat{J}_{z,s}}$. Here, as well, parity commutes with the spinor Hamiltonian, $\left[\hat{\mathcal{P}}_{3m}, \hat{H}_{3m}\right] = 0$ and the state produced by the unitary evolution is the eigenstate of the parity operator $\mathcal{P}_{3m}|\Psi(t)\rangle_{3m} = |\Psi(t)\rangle_{3m}$ at any time t. Considering the optimal generator of interferometric transformation for spinor system of the form $\hat{\Lambda}_{\mathbf{n}_{max}} = a\hat{J}_{x,s} + b\hat{J}_{y,s}$ with $a^2 + b^2 = 1$ and following the same steps we used for the two-mode system we obtain $\Delta\theta^{-2}|_{\theta=0} = 4\Delta^2\hat{\Lambda}_{\mathbf{n}_{max}}$, which saturates

the variance of the optimal generator. We plot the results in Fig. 4.9 for a generator given by $\hat{\Lambda}_{\mathbf{n}} = \hat{J}_x$ where the double dotted line represents the inverse of Eq. (4.48) for $\hat{\mathcal{S}} = \hat{\mathcal{P}}_{3\mathrm{m}}$. Additionally, we can show that in this case the measurement $\hat{\mathcal{S}} = \hat{J}_z^2$ also saturates the QFI (see Fig. 4.9 (dashed green line)). This choice of the measurement is effective because the magnetization is a constant of motion for the spinor system considered here. Therefore, saturation of the QFI for this measurement can be proved analytically as well.

In this chapter we showed that the structure of the mean-field phase portrait in the system of spin-1 condensate is similar to that of the BJJ system. In both cases, the unstable saddle fixed point squeezes the state entangling the atoms, providing useful states for quantum metrology. We presented an analysis of the best generators of the interferometric transformation, enabling us to obtain precision with Heisenberg scaling. With both analytical and numerical calculations, we showed that for short-time evolution the QFI scales with the number of atoms. Additionally, we proved that parity is an optimal measurement which saturates the QFI. In our calculations, we neglected any source of noise; nevertheless in the context of parity measurement we would like to address the problem of detection noise. For the signal-to-noise ratio in Eq. (4.48), the effect of detection noise is included by replacing $\hat{\mathcal{S}}$ with $\hat{\tilde{\mathcal{S}}} = \hat{\mathcal{S}} + \hat{\delta}_{\mathcal{S}}$. An independent Gaussian operator $\hat{\delta}_{\mathcal{S}}$ satisfies $\left\langle \hat{\delta}_{\mathcal{S}} \right\rangle = 0$ and $\left\langle \hat{\delta}_{\mathcal{S}}^2 \right\rangle = \sigma^2$ [160]. Therefore, in order to preserve high precision for measurement, single-atom detection resolution is required ($\sigma^2 \lesssim 1$). Recently, the single atom imaging resolution was presented for single trapped atoms and optical lattices using fluorescence imaging [161, 162], and also in the context of mesoscopic ensembles in a cavity, where the number of atoms is estimated from the shift in the cavity frequency [163]. Moreover, in bimodal and spinor systems, the detection resolution near a single-atom level has been obtained [164, 165] with the possibility of further enhancement. Therefore, our measurement scheme can be realized with current state-of-art. In the next chapter we will present a new method for detecting entanglement and Bell correlations in many-body systems, and then apply our results to the systems of one-dimensional spin chains.

Chapter 5

Quantum Correlations in Spin Chains

In this chapter we introduce a class of Bell inequalities, which allows for a systematic analysis of correlations with no assumptions on how the local outcomes are bounded [166–168]. We start in Section 5.1 with the construction of the correlator for N qubits and analyze how the information about many-body entanglement and nonlocality can be extracted from the single element of the density matrix. We illustrate our results with spin chain systems of an experimentally accessible quantum Ising model [169–172] in Section 5.2, and an XXZ spin chain [173, 174] and a Majumdar-Ghosh model [175, 176] in Section 5.3. The method presented here allows one to differentiate between the cases where the correlations in the state extend over all spins [138, 177] and the cases where fewer spins are entangled/nonlocally correlated. The experimental application of our protocol is reachable with the current state-of-art [162, 178]. Please note: this method can be applied to any multi-qubit state, such as many-photon configurations [179, 180] or Bose-Einstein condensates [47, 181], which is demonstrated in the last chapter of this thesis.

Contents

Ensembles of qubits are ideally suited for the studies of quantum phase transitions [182], many-body entanglement [71] or nonlocality [99]. States of correlated qubits are essential in quantum-enhanced metrology [71, 147], quantum-information processing [183] and tests of quantum mechanics. The precise control of the quantum many-body states is possible in the field of quantum simulators [184], including the systems of ultra-cold atoms [112–114, 185–189], trapped ions [11, 190–195] and super-conducting qubits [196–198]. With growing interest in quantum correlations, the precise characterization of many-qubit systems is relevant from the experimental point of view. For example, measures of entanglement, e.g. the entanglement entropy [199–206] or negativity [207–209], require a precisely reconstructed density matrix which makes experimental measurements very demanding [210, 211]. Here we show that even a single element of the density matrix – associated with the formation probability [212–215] – is sufficient to extract precise information about many-body

entanglement [25] and Bell nonlocality [3, 4, 216]. In the first section we will introduce an N-qubit correlator carrying information about a multitude of quantum features.

5.1 The Bell Inequality for N Qubits

Let us adapt Bell's gedanken experiment from Chapter 1 to a system of N parts. A measurement on each party yields two binary results, $\sigma_x^{(k)} = \pm 1$ and $\sigma_y^{(k)} = \pm 1$, where the superscript $k \in \{1, 2..., N\}$ labels the k-th body. We take a correlator

$$\mathcal{C}_N = \left\langle \sigma_\pm^{(1)} \cdot \ldots \sigma_\pm^{(N)} \right\rangle, \tag{5.1}$$

where $\sigma_\pm^{(k)} = \frac{1}{2}(\sigma_x^{(k)} \pm i\sigma_y^{(k)})$ and the "$\pm$" sign can be chosen independently for each party. According to Bell's original argument, see Eq. (1.9), the correlator is consistent with the local hidden-variable theory (LHV) if $\mathcal{C}_N$ can be expressed in terms of a probability distribution $p(\lambda)$ of some random (hidden) variable λ, i.e.

$$\mathcal{C}_N = \int d\lambda\, p(\lambda)\sigma^{(1)}(\lambda) \cdot \ldots \cdot \sigma^{(N)}(\lambda). \tag{5.2}$$

Using a Cauchy-Schwarz inequality, see Eq. (2.14), for $\mathcal{E}_N = |\mathcal{C}_N|^2$ we obtain the Bell inequality [166, 217] in the following form

$$\mathcal{E}_N \leqslant \int d\lambda\, p(\lambda)|\sigma^{(1)}(\lambda)|^2 \cdot \ldots \cdot |\sigma^{(N)}(\lambda)|^2. \tag{5.3}$$

Since $\left|\sigma^{(k)}(\lambda)\right|^2 = \frac{1}{2}$, we have

$$\mathcal{E}_N \leqslant 2^{-N}, \tag{5.4}$$

which holds true for all systems consistent with a local hidden variable theory. For quantum systems each $\sigma_\pm^{(k)}(\lambda)$ is replaced by the Pauli rising/lowering operator for k-th qubit, giving the Bell inequality in the form

$$\mathcal{E}_N = \left| \left\langle \bigotimes_{k=1}^{N} \hat{\sigma}_\pm^{(k)} \right\rangle \right|^2 \leqslant 2^{-N}. \tag{5.5}$$

Violation of the above inequality signals that the system is nonlocal. The correlator in Eq. (5.1) can also detect entanglement. To show this, we consider a separable system, i.e. a system described with the density matrix

$$\hat{\varrho}_N = \int d\lambda\, p(\lambda) \bigotimes_{k=1}^{N} \hat{\varrho}^{(k)}(\lambda). \tag{5.6}$$

Using the relation $\mathrm{Tr}\left[\hat{\varrho}^{(k)}(\lambda)\hat{\sigma}_+^{(k)}\right] = \left|\left\langle \hat{\sigma}_+^{(k)} \right\rangle\right|_\lambda^2 \leqslant \frac{1}{4}$ we obtain a bound for the class of separable states

$$\mathcal{E}_N \leqslant \int d\lambda\, p(\lambda) \prod_{k=1}^{N} \left|\left\langle \hat{\sigma}_+^{(k)} \right\rangle\right|_\lambda^2 \leqslant 2^{-2N}. \tag{5.7}$$

Violation of inequality (5.7) signals the presence of entanglement in the system [168]. Since the following results are illustrated with the spin ensembles, from this point we refer to qubit as a single spin-1/2 state for which the two levels can be taken as "spin-up" $|\uparrow\rangle$ and "spin-down" $|\downarrow\rangle$.

The correlator in Eq. (5.5) can be expressed with a single element of the density matrix. For example, if we choose the "+" sign for each operator therein, then, since $\hat{\sigma}_+^{(k)}|\downarrow_k\rangle = |\uparrow_k\rangle$, the correlator couples $|\psi_a\rangle \equiv |\downarrow_1,\ldots,\downarrow_N\rangle$ with $|\psi_b\rangle \equiv |\uparrow_1,\ldots,\uparrow_N\rangle$.

Therefore we have $\mathcal{E}_N = |\varrho_{a,b}|^2$, where $\varrho_{a,b}$ is the matrix element corresponding to $|\psi_a\rangle\langle\psi_b|$, proving that information about entanglement and nonlocality can be extracted from a single element of the density matrix. The correlator $\mathcal{E}_N$ has a size-independent upper bound

$$\mathcal{E}_N = |\varrho_{a,b}|^2 \leqslant \varrho_{a,a}\varrho_{b,b} \leqslant \frac{1}{4}. \tag{5.8}$$

As a consequence, while the inequality (5.7) can be violated starting from $N = 2$, the inequality (5.4) requires at least $N = 3$. Note that this correlator is maximal, $\mathcal{E}_N = \frac{1}{4}$, for the Greenberger-Horne-Zeilinger (GHZ) state

$$|\psi\rangle = \frac{1}{\sqrt{2}}\left(|\uparrow\rangle^{\otimes N} + |\downarrow\rangle^{\otimes N}\right). \tag{5.9}$$

We showed how the single element of density matrix can be used to determine correlations in the system. In the next section we provide a few examples of quantum states to demonstrate that $\mathcal{E}_N$ provides detailed information on multiparticle entanglement and nonlocality.

5.1.1 Many-body Entanglement and Nonlocality

Consider a system where only two spins are entangled, while the other $N-2$ are separable, i.e.

$$\hat{\varrho}_N = \int d\lambda\, p(\lambda) \left(\bigotimes_{k=1}^{N-2} \hat{\varrho}^{(k)}(\lambda)\right) \otimes \hat{\varrho}_2(\lambda). \tag{5.10}$$

The number in the subscript of the density matrix stands for the number of spins it describes, while the superscript (k) marks a single k-th spin. In this case, the CSI bounds the correlator $\mathcal{E}_N$ in the following way

$$\mathcal{E}_N \leqslant \int d\lambda\, p(\lambda)\, \mathcal{E}_{N-2}(\lambda) \int d\lambda\, p(\lambda)\, \mathcal{E}_2(\lambda) \leqslant 4^{-(N-1)}. \tag{5.11}$$

The correlator $\mathcal{E}_{N-2}(\lambda)$ is calculated with the product state of $\bigotimes_{k=1}^{N-2} \hat{\varrho}^{(k)}(\lambda)$, while $\mathcal{E}_2(\lambda)$ with the density matrix of the remaining two entangled spins $\hat{\varrho}_2(\lambda)$. The upper bound $4^{-(N-1)}$ is based on Eq. (5.8). Inequality (5.11) is saturated by a product of a two-spin GHZ state, see Eq. (5.9), and $N-2$ states of a form

$$|\psi_k\rangle = \frac{1}{\sqrt{2}}\left(|\uparrow_k\rangle + e^{i\varphi_k}|\downarrow_k\rangle\right), \tag{5.12}$$

with φ_k as an arbitrary phase. If the bound in Eq. (5.11) is violated, it signals that either more pairs than just one are entangled or the entanglement extends for more than two spins. However, if we consider a state with an even number of spins N for

which all atoms are pairwise entangled, i.e.

$$\hat{\varrho}_N = \int d\lambda\, p(\lambda) \bigotimes_{k=1}^{\frac{N}{2}} \hat{\varrho}_2^{(k)}(\lambda), \tag{5.13}$$

where $\hat{\varrho}_2^{(k)}(\lambda)$ is a density operator of the k-th pair, then the violation of inequality $\mathcal{E}_N \leqslant 4^{-\frac{N}{2}}$ signals that at least three spins are entangled.

For the systems with entanglement extended over all-but-one spin given with

$$\hat{\varrho}_N = \int d\lambda\, p(\lambda)\, \hat{\varrho}_{N-1}(\lambda) \otimes \hat{\varrho}^{(N)}(\lambda), \tag{5.14}$$

the correlator will take values from the range $]\frac{1}{32}, \frac{1}{16}]$. If $\mathcal{E}_N > \frac{1}{16}$ then all the particles would be entangled.

Analogically, from the value of $\mathcal{E}_N$ we can also extract information about the extent of nonlocal correlations in the spin system. For instance, when the LHV theory cannot explain correlations among more than three spins, then the inequality reads

$$\mathcal{E}_N \leqslant \int d\lambda\, p(\lambda)\, \mathcal{E}_{N-3}(\lambda) \int d\lambda\, p(\lambda)\, \mathcal{E}_3(\lambda) \leqslant 2^{-(N-1)}. \tag{5.15}$$

The bound of the above inequality is calculated based on the fact that for the locally correlated $N-3$ spins $\mathcal{E}_{N-3}(\lambda) \leqslant 2^{-(N-3)}$, while $\mathcal{E}_3(\lambda) \leqslant 2^{-2}$. The violation of the inequality (5.15) and $\mathcal{E}_N \in]\frac{1}{16}, \frac{1}{8}]$ implies that $N-1$ spins are nonlocally correlated. The correlator takes value from the range $\mathcal{E}_N \in]\frac{1}{8}, \frac{1}{4}]$ only for systems where the nonlocality extends over all the spins.

In the following sections we will present these considerations in the context of spin-chain systems, for which the correlator $\mathcal{E}_m$ takes the form

$$\mathcal{E}_m = \left| \left\langle \hat{\sigma}_\pm^{(1)} \otimes \hat{\sigma}_\pm^{(2)} \otimes \hat{\sigma}_\pm^{(3)} \ldots \otimes \hat{\sigma}_\pm^{(m)} \right\rangle \right|^2, \tag{5.16}$$

where the average value is calculated on a ground state of some Hamiltonian. The correlator in Eq. (5.16) can be optimized by the proper choice of signs based on the expected structure of correlations in a given state. This can be done, for example, by looking at the largest off-diagonal element of the density matrix in the local spin basis. The correlators given by Eq. (5.16) are known as formation probabilities and have been studied in the thermodynamically large systems of spin-chains [212–215, 218–223].

We consider finite systems and provide detailed insight into the structure of entanglement and nonlocality in the ground states of experimentally relevant Hamiltonians. In the next section we show our result in the context of a one-dimentional Ising Hamiltonian.

5.2 Ising Hamiltonian

Let us consider a one-dimensional Ising Hamiltonian

$$\hat{H} = -J \sum_{j=1}^{N-1} \hat{\sigma}_z^{(j)} \hat{\sigma}_z^{(j+1)} - h \sum_{j=1}^{N} \hat{\sigma}_x^{(j)}, \tag{5.17}$$

where J represents the energy interaction between nearest neighbors, the parameter h is the magnitude of the external magnetic field in the x-direction and $\sigma_i^{(k)}$ is i-th Pauli operators acting on k-th spin. For $J \propto h$ the model experiences a phase transition between an ordered and a disordered regime. The signs in this Hamiltonian are conventional, and for the choice in Eq. (5.17), $J < 0$ corresponds to antiferromagnetic interactions, while $J > 0$ to ferromagnetic interactions. The upper limit in the sum of the interaction term implies open boundary conditions.

In the case of strong antiferromagnetic interactions, $J \to -\infty$, the ground state of the Hamiltonian (5.17) is two-fold degenerated and exhibits antiferromagnetic ordering. It is given by a superposition of two antiferromagnetic states called the Néel state [224, 225]

$$|\psi\rangle = \frac{1}{\sqrt{2}} \left(|\uparrow\downarrow\uparrow\downarrow \ldots\rangle + |\downarrow\uparrow\downarrow\uparrow \ldots\rangle \right). \tag{5.18}$$

For $J \to \infty$ the ground state is also degenerated. Ferromagnetic interactions favor all spins aligned in the same direction and as a result it is given by the GHZ state

$$|\psi\rangle = \frac{1}{\sqrt{2}} \left(|\uparrow\uparrow \ldots \uparrow\rangle + |\downarrow\downarrow \ldots \downarrow\rangle \right). \tag{5.19}$$

In the remainder of this section we focus on the antiferromagnetic Ising Hamiltonian of a form

$$\hat{H} = \sum_{j=1}^{N-1} \hat{\sigma}_z^{(j)} \hat{\sigma}_z^{(j+1)} + g \sum_{j=1}^{N} \hat{\sigma}_x^{(j)}, \tag{5.20}$$

where $g = h/J$ is now the control parameter. The system exhibits a phase transition at $|g| = 1$, between ordered ($|g| < 1$) phase and disordered ($|g| > 1$) phase.

We find the ground state of the Ising model by performing a numerical diagonalization of the Hamiltonian (5.20) for $N = 6$. Based on the expected structure of the eigenstate corresponding to the lowest eigenenergy for strong interactions ($g \to 0$), we choose a correlator in the form of rising and lowering operators alternating from site to site

$$\mathcal{E}_m = \left| \left\langle \hat{\sigma}_+^{(1)} \otimes \hat{\sigma}_-^{(2)} \otimes \hat{\sigma}_+^{(3)} \ldots \otimes \hat{\sigma}_\pm^{(m)} \right\rangle \right|^2, \tag{5.21}$$

where $m \in [2, 6]$. We plot correlators $\mathcal{E}_2$ to $\mathcal{E}_5$ as a function of g in Fig. 5.1 in relation to entanglement (4^{-m}) and nonlocality (2^{-m}) bounds. While the lowest order of correlator ($m = 2$) implies entanglement in the system, the Bell correlations are witnessed only with $m = 5$. The zero value of the correlator at $g \to 0$ is a consequence of the structure of the ground state in a vanishing magnetic field – the Néel state, see Eq. (5.18). Thus tracing out the sixth spin results with a classical mixture

$$\hat{\rho} = \frac{1}{2} \left(|\uparrow\downarrow\uparrow\downarrow\uparrow\rangle\langle\uparrow\downarrow\uparrow\downarrow\uparrow| + |\downarrow\uparrow\downarrow\uparrow\downarrow\rangle\langle\downarrow\uparrow\downarrow\uparrow\downarrow| \right) \tag{5.22}$$

and the information in the off-diagonal elements is lost. With $g \gg 1$ the interactions are negligible and so the ground state resembles that of noninteracting spins, and therefore the value of the correlators tends to 4^{-m} in the limit of $g \to \infty$. The Bell correlations are observed for $m = 5$ around the critical point $g = 1$ of the quantum phase transition and, moreover, the lower order correlators reach their maximal value. In this region the correlation length is large (in the thermodynamic limit it approaches

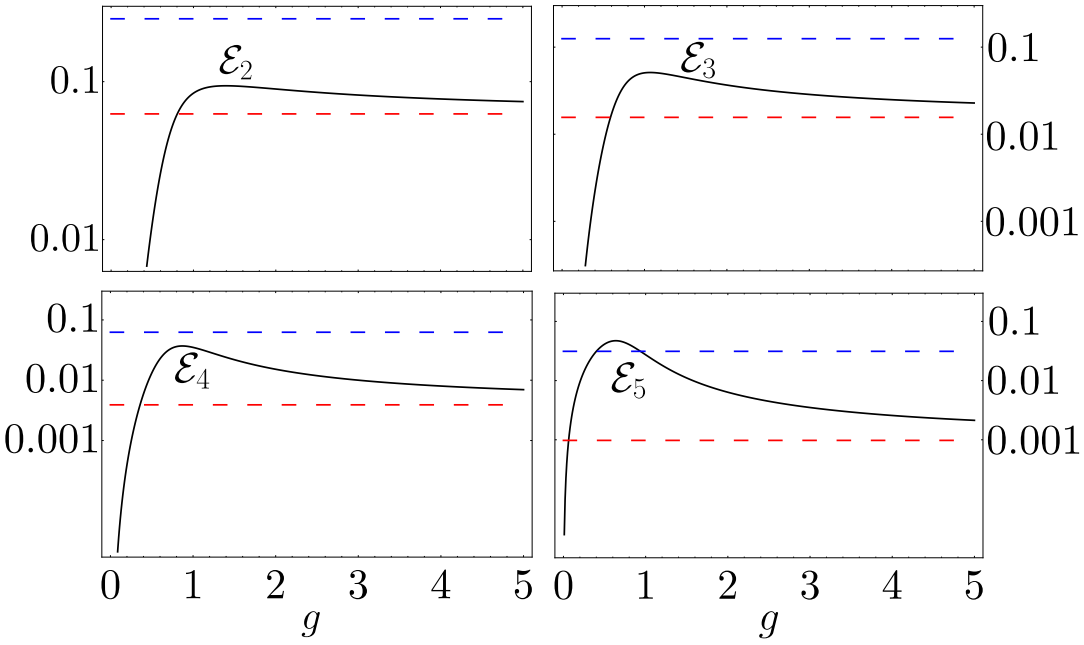

Figure 5.1: Correlators $\mathcal{E}_m$ for $m = 2 \ldots 5$ as a function of g calculated with the ground state of the Ising Hamiltonian (5.20) for $N = 6$. The horizontal dashed lines denote the entanglement bound 4^{-m} (red) and the nonlocality bound 2^{-m} (blue).

infinity) and so a partial trace of a single spin does not completely destroy correlations. As a result, the value of the lower order correlators $\mathcal{E}_m$ remains sufficiently large suggesting that the hierarchy of correlators $\mathcal{E}_m$ is a useful tool for exploring quantum correlations.

The full correlator for $m = 6$ is plotted separately in Fig. 5.2. The maximum value of $\mathcal{E}_6$ is obtained in the region of strong interactions ($g = 0$) as the ground state is given by a maximally entangled state given in Eq. (5.18). The plot presents all the bounds derived from our previous discussion, introduced in Eqs. (5.10) and (5.15). Whenever $\mathcal{E}_6 < 4^{-6}$ the state is not entangled and the correlation can be reproduced with a separable state of 6 spins. This is illustrated on the RHS bottom with six unboxed arrows. If $\mathcal{E}_6 \in]4^{-6}, 4^{-5}[$, then the correlation can be reproduced with a system of two entangled spins and the other four forming a separable state, i.e. described with the density matrix given in Eq. (5.10). The corresponding pictograph represents two spins in a box, while the other four remain unboxed. The states with two and three entangled pairs of spins explain correlations when $\mathcal{E}_6 \in]4^{-5}, 4^{-4}[$ (2x2x1x1) and $\mathcal{E}_6 \in]4^{-4}, 4^{-3}[$ (2x2x2), respectively. Analogically, the Bell correlations can be explained on the basis of a full LHV theory when $\mathcal{E}_6 < 2^{-6}$. Breaking this inequality signals that some of the spins are nonlocally correlated, depending on the value of $\mathcal{E}_6$. All the other cases are shown in Fig. (5.2) where boxed spins represent correlations between the spins – either entanglement on the RHS or nonlocality on the LHS.

5.2.1 Long-range Interactions

We will now consider a case where long-range interactions are present in the system of the Ising model. This can be done by adding a term connecting every spin with

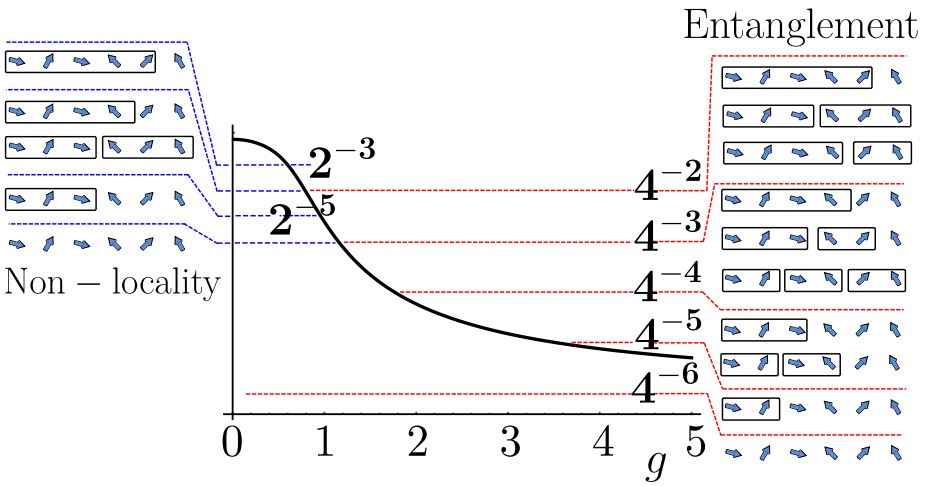

Figure 5.2: The full six-spin correlator $\mathcal{E}_6$ (solid black line) calculated with the ground state of the Hamiltonian (5.20) as a function of g. The horizontal red (entanglement) and blue (nonlocality) dashed lines separate regions, where $\mathcal{E}_6$ can be reproduced by a spin system with a specific multiparticle correlation; see the main text for an explanation.

the next-to-adjacent one to the Hamiltonian (5.20) as follows

$$\hat{H} = \sum_{j=1}^{N-1} \hat{\sigma}_z^{(j)} \hat{\sigma}_z^{(j+1)} + g \sum_{j=1}^{N} \hat{\sigma}_x^{(j)} + K \sum_{j=1}^{N-2} \hat{\sigma}_z^{(j)} \hat{\sigma}_z^{(j+2)}. \tag{5.23}$$

The ferromagnetic long-range interactions ($K < 0$) will favor a setting where odd and even spins are oriented in the same direction. Thus, the correlations in the ordered phase ($g < 1$) will be strengthened. However, the antiferromagnetic long-range interractions ($K > 0$) will cause frustration in the spin chain due to competition between long- and short-range interactions, manifested by the appearance of the pairs of adjacent spins oriented in the same direction. Therefore, the structure of the ground

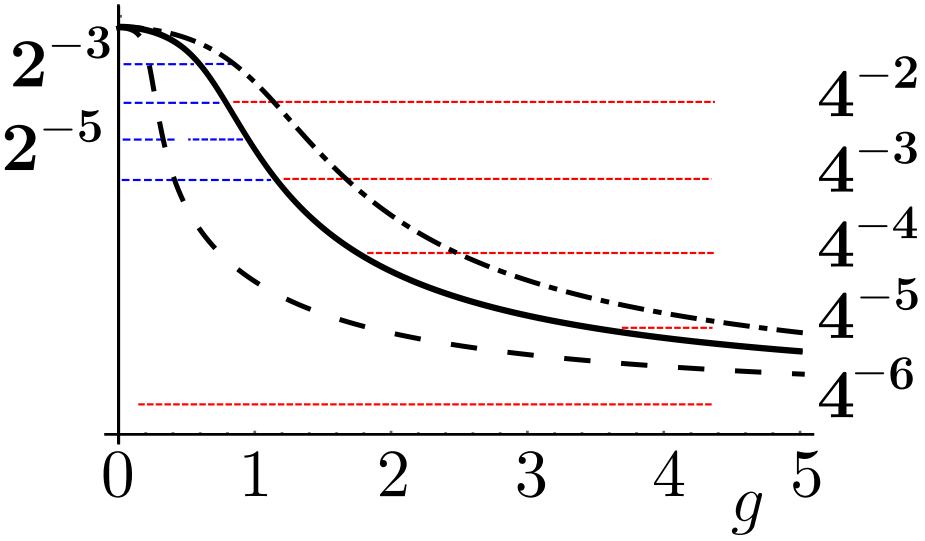

Figure 5.3: The correlator $\mathcal{E}_6$ calculated with the Hamiltonian (5.23) for $K = 0$ (solid black line), $K = 0.4$ (dashed line) and $K = -0.4$ (dash-dotted line).

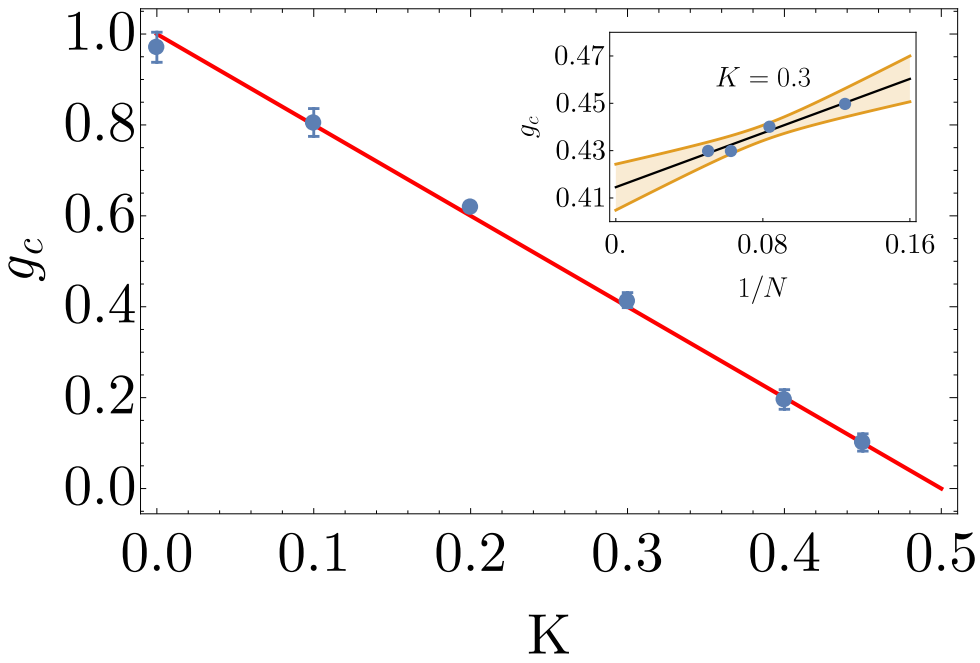

Figure 5.4: Blue dots represent results of finite size scaling of the position of the maximum of $\mathcal{E}_{N/2}$ using $N = 8, 12, 16, 20$ (an inset shows an example of scaling for $K = 0.3$). The red line denotes the quantum phase transition separating the antiferromagnetic phase from the paramagnetic phase [226–228]. The error bars come from the linear fit estimation of the finite size scaling. The shaded region in the inset represents the 0.9 confidence interval.

state is disturbed and the value of the correlators will be diminished. In Fig. 5.3 we compare the $\mathcal{E}_6$ for $K = 0$ and $K = \pm 0.4$, showing that indeed the spin chains behave as expected. Including the long-range interactions in the Hamiltonian (5.23) enables us to examine the relation between the hierarchy of the correlations and the quantum phase transition. In the case of a competing interaction ($K > 0$), the position of the critical point for $K < 0.5$ is given by $g_c = 1 - 2K$ [226–228]. The plot presented in Fig. 5.1 suggests that the critical point at $g_c = 1$ for a short-range Ising model (see Eq. (5.20)) may be related to the maximal value of the correlator $\mathcal{E}_3$. Consequently, we perform the finite-size scaling of the position of the maximum of $\mathcal{E}_{N/2}$ for chains of length $N = 8, 12, 16, 20$ for different values of K. Fig. 5.4 confirms that the maximal value of the correlator $\mathcal{E}_{N/2}$ corresponds to the position of the quantum phase transition. However, $\mathcal{E}_{N/2}$ is not a standard order parameter [182] since it does not exhibit a singularity at the critical point.

The results presented in this section demonstrate that the hierarchy of the correlations does not only provide detailed tomography of quantum correlations, but also helps to understand the quantum properties of the many-body systems such as quantum phase transitions. In the next section we will examine the XXZ spin chain model. We will derive analytical formulas for the correlators and then express them using the Bethe ansatz solution. Additionally, we will show the impact of temperature on the hierarchy.

5.3 One-dimensional Heisenberg Model

The Heisenberg model describes spins interacting with nearest-neighbors. In a one-dimensional case such system forms a chain or, if the periodic boundaries are considered, a ring. In the most general case, the Heisenberg's Hamiltonian is

$$H_{XYZ} = \sum_{i=1}^{N} (J_x \hat{S}_x^{(i)} \hat{S}_x^{(i+1)} + J_y \hat{S}_y^{(i)} \hat{S}_y^{(i+1)} + J_z \hat{S}_z^{(i)} \hat{S}_z^{(i+1)}) - h_z \sum_{i=1}^{N} \hat{S}_z^{(i)}, \tag{5.24}$$

where N is the number of spins, $J_{x,y,z}$ are coupling constants corresponding to spin projection operators $\hat{S}_\alpha^{(i)}$ in $\alpha \in \{x, y, z\}$ direction acting on i-th site. Assuming periodic boundary conditions the identity $\hat{S}_\alpha^{N+1} = \hat{S}_\alpha^1$ holds. The effect of the external magnetic field along z-axis is included with the last term in Eq. (5.24), where h_z is the field strength.

In this chapter we focus on the spin-1/2 systems, although, in general, the Heisenberg Hamiltonian can be solved for an arbitrary spin [229, 230]. In this case operators $\hat{S}$ can be represented by Pauli matrices $\hat{S}_\alpha^{(i)} = \frac{\hbar}{2}\hat{\sigma}_\alpha^{(i)}$, where $\hat{\sigma}_\alpha^{(i)} \equiv \hat{\mathbb{1}}^{\otimes(i-1)} \otimes \sigma_\alpha \otimes \hat{\mathbb{1}}^{\otimes(N-i)}$.

If all coupling constants are different, the model is called the XYZ Heisenberg model, introduced by T. Bill Sutherland [231]. If $J_x = J_y$, then it is the XXZ Heisenberg model. For the isotropic interactions, namely $J_x = J_y = J_z$, we have the XXX Heisenberg model, initially solved by Hans Bethe [232]. Whenever $J_z = 0$ we have either the XY model [233] when $J_x \neq J_y$, or XX model when $J_x = J_y$ [234]. To this end, we focus on the XXZ Heisenberg spin chain in the zero external field, $h_z = 0$, which has the following form ($\hbar = 1$):

$$H_{XXZ} = \frac{J}{4} \sum_{j=1}^{N} \left(\hat{\sigma}_x^{(i)} \hat{\sigma}_x^{(i+1)} + \hat{\sigma}_y^{(i)} \hat{\sigma}_y^{(i+1)} + \Delta \hat{\sigma}_z^{(i)} \hat{\sigma}_z^{(i+1)} \right), \tag{5.25}$$

where $\Delta \cdot J = J_z$ and Δ is an order parameter that specifies the different phases of the model itself. When $J > 0$ the system is in the ferromagnetic phase for $\Delta \leq -1$, in the antiferromagnetic quantum critical phase for $-1 < \Delta < 1$, and in the antiferromagnetic phase for $1 \leq \Delta$. For $\Delta \to \pm\infty$ we obtain a simple Ising model. In the case of $\Delta \ll -1$, the z-component increases the energy for each pair of antiparallel spins and so as $\Delta \to -\infty$ the ground state is a type of NOON state as shown in Eq. (5.19). When $\Delta \gg 1$, we have the opposite situation – adjacent antiparallel spins are favored with respect to the energy. The ground state is then an antiferromagnet with the non-trivial form that depends on Δ and parity of N. Nevertheless with the $\Delta \to -\infty$ and even number of spins N, the ground state is represented by the Néel state (see Eq. (5.18)). For $\Delta = 1$ we get the isotropic XXX Heisenberg spin chain. We will now present the exact solution for the chain of length $N = 4$.

5.3.1 Exact Solution for $N = 4$

The XXZ Hamiltonian can be solved analytically for any N using the Bethe ansatz method. Nevertheless, a particularly simple solution exists for $N = 4$ given with

$$\hat{H} = \frac{1}{4} \left(\sum_{j=1}^{N=4} \hat{\sigma}_x^{(j)} \hat{\sigma}_x^{(j+1)} + \hat{\sigma}_y^{(j)} \hat{\sigma}_y^{(j+1)} + \Delta \hat{\sigma_z}^{(j)} \hat{\sigma_z}^{(j+1)} \right) \tag{5.26}$$

with a periodic boundary condition $\hat{\vec{\sigma}}^{(5)} \equiv \hat{\vec{\sigma}}^{(1)}$. For $\Delta \leq -1$ the energy of the ground state is doubly degenerated $E_g = \Delta$ and the state is represented by the superposition shown in Eq. (5.19). When $\Delta > -1$, the lowest energy is $E_g = \frac{1}{2}\left(-\Delta - \sqrt{8+\Delta^2}\right)$ and the ground state in the local spin basis is given with

$$|E_g\rangle = \mathcal{N}\left(\frac{\Delta - \sqrt{8+\Delta^2}}{2\sqrt{2}}|AF_2\rangle + |AF\rangle\right), \tag{5.27}$$

where $\mathcal{N}$ is the normalization factor

$$\mathcal{N} = \sqrt{\frac{1}{4+2E_g^2}} \tag{5.28}$$

and

$$|AF_2\rangle = \frac{1}{2}\left(|\uparrow\uparrow\downarrow\downarrow\rangle + |\downarrow\uparrow\uparrow\downarrow\rangle + |\downarrow\downarrow\uparrow\uparrow\rangle + |\uparrow\downarrow\downarrow\uparrow\rangle\right), \tag{5.29}$$

$$|AF\rangle = \frac{1}{\sqrt{2}}\left(|\uparrow\downarrow\uparrow\downarrow\rangle + |\downarrow\uparrow\downarrow\uparrow\rangle\right). \tag{5.30}$$

To this end we will consider the case where $\Delta > -1$. Therefore, we will use a correlator of the form

$$\mathcal{E}_4 = \left|\langle E_g|\hat{\sigma}_+^{(1)}\hat{\sigma}_-^{(2)}\hat{\sigma}_+^{(3)}\hat{\sigma}_-^{(4)}|E_g\rangle\right|. \tag{5.31}$$

The average of the correlator in Eq. (5.31) in zero temperature is calculated using the ground state given by Eq. (5.27) and has the following form

$$\mathcal{E}_4 = \frac{1}{16}\left(1 + \frac{\Delta}{\sqrt{8+\Delta^2}}\right)^2. \tag{5.32}$$

To include the nonzero temperature effects we have to consider a system described by the thermal density matrix

$$\hat{\varrho}_T = \frac{1}{\mathcal{Z}}\sum_n e^{-\beta E_n}|\psi^{(n)}\rangle\langle\psi^{(n)}|, \tag{5.33}$$

where the sum is performed over the eigenvalues E_n of the 4-spin Hamiltonian (5.26) ($\hat{H}|\psi^{(n)}\rangle = E_n|\psi^{(n)}\rangle$),$\beta = (k_B T)^{-1}$, with T standing for the temperature, k_B the Boltzmann constant and $\mathcal{Z}$ is the statistical sum. The dimension of a Hilbert space for $N = 4$ is equal to 2^4, but for the correlator in Eq. (5.31) only 3 eigenstates have nonzero expectation values

$$\left|\langle E_\pm|\hat{\sigma}_+^{(1)}\hat{\sigma}_-^{(2)}\hat{\sigma}_+^{(3)}\hat{\sigma}_-^{(4)}|E_\pm\rangle\right| = \frac{1}{4}\left|1 \mp \frac{\Delta}{\sqrt{8+\Delta^2}}\right|, \tag{5.34a}$$

$$\left|\langle E_\Delta|\hat{\sigma}_+^{(1)}\hat{\sigma}_-^{(2)}\hat{\sigma}_+^{(3)}\hat{\sigma}_-^{(4)}|E_\Delta\rangle\right| = -\frac{1}{2}, \tag{5.34b}$$

where $\hat{H}|E_\pm\rangle = E_\pm|E_\pm\rangle$ and $\hat{H}|E_\Delta\rangle = -\Delta|E_\Delta\rangle$ with

$$E_\pm = \frac{1}{2}\left(-\Delta \pm \sqrt{8+\Delta^2}\right). \tag{5.35}$$

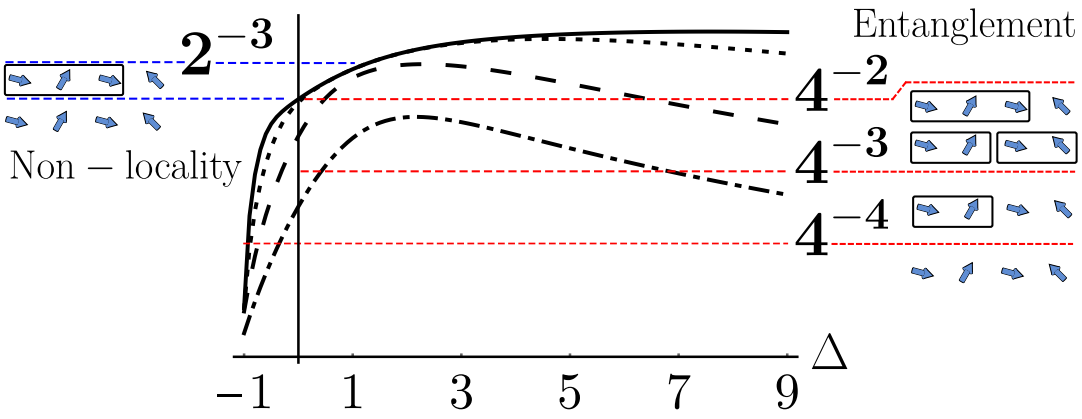

Figure 5.5: $\mathcal{E}_4$ from Eq. (5.31) as a function of Δ for $\beta = 10$ (solid line), $\beta = 5$ (dotted line), $\beta = 2$ (dashed line) and $\beta = 1$ (dash-dotted line).

These states have the following form

$$|E_\pm\rangle = \mathcal{N}_\pm \left(\frac{\Delta \pm \sqrt{8+\Delta^2}}{2\sqrt{2}} |AF_2\rangle + |AF\rangle \right), \tag{5.36}$$

$$|E_\Delta\rangle = \frac{1}{\sqrt{2}} \left(|\uparrow\downarrow\uparrow\downarrow\rangle - |\downarrow\uparrow\downarrow\uparrow\rangle \right) \tag{5.37}$$

with $\mathcal{N}_\pm = \sqrt{1/(4+E_\pm^2)}$ standing for the normalization factors. Therefore, we calculate the partition function

$$\mathcal{E}_4 = \frac{1}{\mathcal{Z}^2} \left[-\frac{e^{-\beta(\Delta+\sqrt{8+\Delta^2})}}{2} + \frac{1}{4}\left(1 + \frac{\Delta}{\sqrt{8+\Delta^2}}\right) + \frac{1}{4}\left(1 - \frac{\Delta}{\sqrt{8+\Delta^2}}\right) e^{-2\beta\sqrt{8+\Delta^2}} \right]^2, \tag{5.38a}$$

$$\mathcal{Z} = 1 + e^{-\beta(E_+ - E_-)} + e^{-\beta(-\Delta - E_-)} + 2e^{-\beta(-1-E_-)} + 7e^{\beta E_-} + 2e^{-\beta(1-E_-)} + 2e^{-\beta(\Delta - E_-)}, \tag{5.38b}$$

for the antiferromagnetic correlator given in Eq. (5.31). The results for $\beta = \{10, 5, 2, 1\}$ are plotted in Fig. 5.5 as a function of the parameter Δ. The Bell correlations seem to vanish for $\beta \lesssim \Delta$ as the energy scale is given by Δ. Nevertheless, even for $\beta = 2$ we observe that the two-particle entangled state cannot reproduce the correlations in the proximity of $\Delta = 1$. In the limit of $T \to 0$ ($\beta \to \infty$) the partition function gives the formula in Eq. (5.32). Its value breaks the LHV limit (2^{-4}) whenever Δ is positive and, additionally, when $\Delta > 2\sqrt{\sqrt{2}-1}$, then $\mathcal{E}_4 > 2^{-3}$, signaling that system is not only four-spin entangled, but also nonlocally correlated.

5.3.2 Bethe Ansatz Solution

The Bethe ansatz can be applied to solve the XXZ spin chain as well. We will focus on the case of $-1 < \Delta \leqslant 1$, where the Hamiltonian spectrum is gapless. We start with the reference state of all spins up $|0\rangle_+$

$$|0\rangle_+ \equiv |\uparrow\uparrow \ldots \uparrow\rangle \tag{5.39}$$

with the maximum magnetization of $N/2$. Therefore, any state can be produced by flipping a proper number of spins. Let's, for example, look at the subspace of $M = 1$ flipped states. In order to account for the translational invariance of the spin chain, we assume that the eigenstate $|\Psi_1\rangle$ is a superposition of all N states with one flipped state:

$$|\Psi_1\rangle = \sum_{m=1}^{N} \chi(m)\hat{\sigma}_-^{(m)}|0\rangle_+ = \sum_{m=1}^{N} \chi(m)|m\rangle. \tag{5.40}$$

We project the Schrödinger equation $\hat{H}|\Psi_1\rangle = E_1|\Psi_1\rangle$ on the bra state $\langle m| = {}_+\langle 0|\hat{\sigma}_+^{(m)}$ and obtain

$$E_1\chi(m_j) = \frac{1}{2}\left(\chi(m_j - 1) + \chi(m_j + 1)\right) - \frac{\Delta}{4}\chi(m_j), \text{ for } 1 < \text{j} < \text{N}. \tag{5.41}$$

Therefore, if $|\Psi_1\rangle$ is an eigenstate then its amplitude has to satisfy Eq. (5.41) as well as the periodic boundary condition $\chi(1) = \chi(N + 1)$. The solution for Eq. (5.41) is found if we take a plane wave ansatz $\chi(m) = e^{ikm}$, where we set lattice spacing to unity. Therefore the eigenenergy is $E_1 = \cos k - \frac{1}{4}\Delta$. Moreover, from the boundary condition we obtain a condition for (quasi-)momentum k

$$e^{(ikN)} = 1 \Rightarrow k_{\bar{I}} = \frac{2\pi\bar{I}}{N}, \tag{5.42}$$

where the quantum number $\bar{I} \in \{0, 1, ..., N-1\}$. From Eq. (5.42) we see that N distinct momenta $k_{\bar{I}}$ lead to a linearly independent eigenstate $|\Psi_1\rangle = \sum_{m=1}^{N} e^{ik_{\bar{I}}m}|m\rangle$.

We move now to the case where two spins are flipped. We start with a superposition of all states with two flipped spins as follows:

$$|\Psi_2\rangle = \sum_{m_1<m_2}^{N} \chi(m_1, m_2)\hat{\sigma}_-^{(m_1)}\hat{\sigma}_-^{(m_2)}|0\rangle_+ = \sum_{j=1}^{N} \chi(m_1, m_2)|m_1, m_2\rangle. \tag{5.43}$$

In this case, when projecting the Schrödinger equation onto the bra $\langle m_1, m_2|$ we have to consider two scenarios: either the two flipped spins occupy adjacent sites or they are separated. In the first case we obtain

$$(E_2 + \Delta)\chi(m_1, m_2) = \frac{1}{2}\left(\chi(m_1 - 1, m_2) + \chi(m_1, m_2 + 1)\right), \tag{5.44}$$

for $2 < m_1 + 1 = m_2 < N$, while in the latter

$$\begin{aligned}(E_2 + 2\Delta)\chi(m_1, m_2) = \frac{1}{2}[&\chi(m_1 - 1, m_2) + \chi(m_1, m_2 - 1) + \\ &+ \chi(m_1 + 1, m_2) + \chi(m_1, m_2 + 1)],\end{aligned} \tag{5.45}$$

for $2 < m_1 + 1 < m_2 < N$. This is solved by a wave function of a form:

$$\chi(m_1, m_2) = A_{12}e^{ik_1m_1+ik_2m_2} + A_{21}e^{ik_2m_1+ik_1m_2}, \tag{5.46}$$

for $1 \leqslant m_1 < m_2 \leqslant N$. Using the above plane wave ansatz in Eq. (5.45) leads to $E_2 = \cos k_1 + \cos k_2 - 2\Delta$ and substituting it into Eq. (5.44) with this energy expression

we get a relation for amplitudes A_{12} and A_{21} as follows

$$\frac{A_{12}}{A_{21}} = -\frac{1+e^{ik_1+ik_2}-2\Delta e^{ik_1}}{1+e^{ik_1+ik_2}-2\Delta e^{ik_2}} \equiv -e^{-i\Phi(k_1,k_2)}, \tag{5.47}$$

where $\Phi(k_1,k_2)$ is the scattering phase shift. The quasi-momenta k_1 and k_2 appearing in the Bethe ansatz wave function can be determined from the periodic boundary conditions: $\chi(m_1,m_2)=\chi(m_2,m_1+N)$. As a result, we obtain

$$k_1 = \frac{2\pi I_1}{N} + \frac{1}{N}\Phi(k_1,k_2) \tag{5.48a}$$

$$k_2 = \frac{2\pi I_2}{N} - \frac{1}{N}\Phi(k_1,k_2), \tag{5.48b}$$

where $I_j \in \{0,1,...,N-1\}$ are integer quantum numbers.

Finally we can generalize the ansatz to arbitrary M, nevertheless due to symmetry we will consider $M \leqslant N/2$. For an arbitrary M, the eigenstate is given by

$$|\Psi_M\rangle = \sum_{m_1<\cdots<m_M} \chi(\mathbf{m}_M)|\mathbf{m}_M\rangle, \tag{5.49}$$

where the bold symbol denotes set $\mathbf{m}_M = \{m_j\}_{j=1}^M$. The wave function for arbitrary M is then

$$\chi(\mathbf{m}_M) = \prod_{1\leqslant a\leq b\leqslant M} \mathrm{sgn}(m_a-m_b) \sum_{\sigma\in\mathcal{P}_M} (-1)^{|\sigma|} \exp\left(i\sum_{a=1}^M m_a k_{\sigma_a}\right)$$
$$\times \exp\left(\frac{i}{2}\sum_{b>a}\mathrm{sgn}(m_a-m_b)\Phi(k_{\sigma_a},k_{\sigma_b})\right), \tag{5.50}$$

where $\mathrm{sgn}(\cdot)=\pm 1$. From the periodic boundary conditions $\chi(m_1,m_2,...,m_M) = \chi(m_2,m_3,...,m_M,m_{N+1})$ for every index, we obtain M Bethe equations in logarithmic form:

$$k_a = \frac{2\pi \bar{I}_a}{N} - \sum_{b\neq a}\frac{1}{N}\Phi(k_a,k_b), \tag{5.51}$$

where $a=1,...,M$. Every set of M momenta k_a satysfying these equations gives an eigenstate of the system. The eigenenergy is given by $E_M = \sum_{a=1}^M \cos k_a - \Delta$.

The two-body scattering phase $\Psi(k_1,k_2)$ is not a translational invariant for shifts of the momenta and, therefore, it is convenient to introduce rapidities $\tilde{\lambda}_a$ to parametrize the quasi-momenta k_a:

$$e^{ik_a} = \frac{\sin(\eta(\tilde{\lambda}+i))}{\sin(\eta(\tilde{\lambda}-i))}, \tag{5.52}$$

where η is determined in a way that the scattering phase is a function of the rapidity difference only, which results with

$$\Delta = \cos 2\eta \qquad \pi > \eta \geq 0. \tag{5.53}$$

Therefore, the Bethe equations can be parametrized by the rapidities as follows

$$\tilde{\theta}_1(\tilde{\lambda}_a) = \frac{2\pi I_a}{N} - \frac{1}{N}\sum_{b\neq a}^{M} \tilde{\theta}_2(\tilde{\lambda}_a - \tilde{\lambda}_b), \quad a = 1, \ldots, M, \tag{5.54}$$

with $\tilde{\theta}_n(\tilde{\lambda}) \equiv 2\arctan\left[\coth\frac{n\eta}{2}\tan\frac{\eta\tilde{\lambda}}{2}\right]$. The phase $\tilde{\theta}_1(\tilde{\lambda}_a)$ is actually the original momentum k_a:

$$p(\tilde{\lambda}_j) \equiv \tilde{\theta}_1(\tilde{\lambda}_a) = k_a. \tag{5.55}$$

The amplitudes in Eq. (5.50) can be also parametrized by rapidities $\lambda = \eta\tilde{\lambda}$ [235] as follows

$$\chi(\mathbf{m}_M|\boldsymbol{\lambda}_M) = \frac{1}{|\mathcal{N}_M|}\sum_{\sigma\in\mathcal{P}_M}(-1)^{|\sigma|}\exp\left(-i\sum_{j=1}^{M} m_j p(\lambda_{\sigma_j})\right) \times \exp\left(-\frac{i}{2}\sum_{k>j}\theta(\lambda_{\sigma_k} - \lambda_{\sigma_j})\right), \tag{5.56}$$

where $\chi(\mathbf{m}_M|\boldsymbol{\lambda}_M)$ indicates amplitude in the language of rapidities. Momentum $p(\lambda)$ and the two-body scattering phase shift $\theta(\lambda)$ are now

$$p(\lambda) = i\log\frac{\cosh(\lambda - i\eta)}{\cosh(\lambda + i\eta)}, \tag{5.57}$$

$$\theta(\lambda) = i\log\frac{\sinh(2i\eta + \lambda)}{\sinh(2i\eta - \lambda)}. \tag{5.58}$$

The normalization $\mathcal{N}_M$ in Eq. (5.56) is given with

$$|\mathcal{N}_M|^2 = \frac{\det G_M}{\prod_{j=1}^{M} K_1(\lambda_j)}, \tag{5.59}$$

and guarantees that $\langle\Psi_M|\Psi_M\rangle = 1$. The factors appearing in the normalization are the Gaudin matrix

$$G_{jk} = \delta_{jk}\left(NK_1(\theta_j) - \sum_{m=1}^{M} K_2(\lambda_j - \lambda_m)\right) + K_2(\lambda_j - \lambda_k) \tag{5.60}$$

and functions

$$K_1(\lambda) = \partial_\lambda p(\lambda) = \frac{\sin 2\eta}{\cosh(\lambda - i\eta)\cosh(\lambda + i\eta)}, \tag{5.61}$$

$$K_2(\lambda) = \partial_\lambda\theta(\lambda) = \frac{\sin 4\eta}{\sinh(\lambda - 2i\eta)\sinh(\lambda + 2i\eta)}. \tag{5.62}$$

This representation is especially convenient for computation of the correlator $\mathcal{E}_N$ in the ground state $|GS\rangle$:

$$\mathcal{E}_N = |\mathrm{Tr}\left[|GS\rangle\langle GS|\cdot|\uparrow\downarrow\uparrow\ldots\rangle\langle\downarrow\uparrow\downarrow\ldots|\right]|^2 = |\langle\mathrm{GS}|\downarrow\uparrow\downarrow\ldots\rangle|^2\cdot|\langle\uparrow\downarrow\uparrow\ldots|\mathrm{GS}\rangle|^2, \tag{5.63}$$

where the overlaps $\langle\mathrm{GS}|\downarrow\uparrow\downarrow\ldots\rangle$ and $\langle\uparrow\downarrow\uparrow\ldots|\mathrm{GS}\rangle$ are known exactly for arbitrary N and Δ, and are given by the corresponding antiferromagnetic components of the

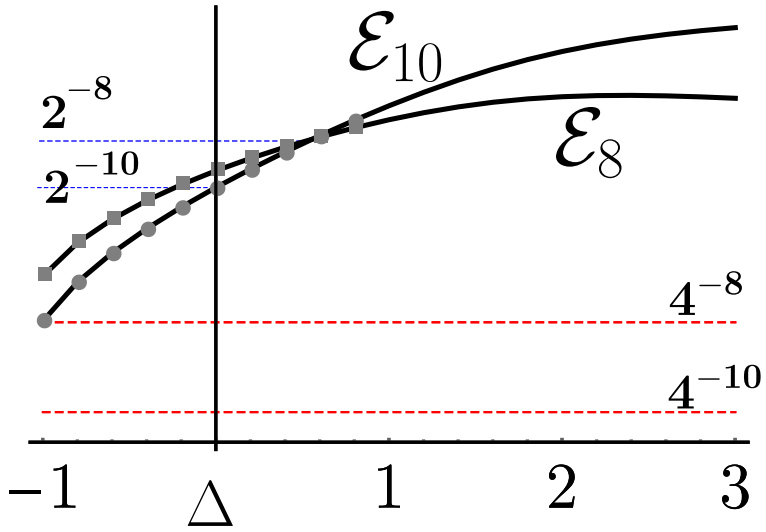

Figure 5.6: The ground state correlators $\mathcal{E}_{10}$ and $\mathcal{E}_8$ for the XXZ spin chain of length $N = 10$ as a function of the anisotropy Δ. We show the analytic results (gray points) of Bethe ansatz (5.63) and the results of numerical diagonalization (black solid line) of the XXZ Hamiltonian (5.25). In the limit $\Delta \to \infty$ the correlators approach those of the Ising model with $g = 0$.

ground state calculated according to Eq. (5.49) with amplitudes from Eq. (5.56):

$$\langle \mathrm{GS}|{\downarrow}{\uparrow}{\downarrow}\ldots\rangle = \chi(\mathbf{O}_\mathrm{N}|\boldsymbol{\lambda}_\mathrm{M}), \tag{5.64}$$

$$\langle {\uparrow}{\downarrow}{\uparrow}\ldots|\mathrm{GS}\rangle = \chi(\mathbf{E}_\mathrm{N}|\boldsymbol{\lambda}_\mathrm{M}), \tag{5.65}$$

where $\mathbf{E}_m = \{m_2, m_4, \ldots, m_M\}$ denotes odd spins and $\mathbf{O}_m = \{m_1, m_3, \ldots, m_{M-1}\}$ even spins flipped. The amplitudes $\chi(\mathbf{m}_M|\boldsymbol{\lambda}_M)$ allow us to access the lower order correlation functions, e.g.

$$\begin{aligned}\mathcal{E}_{N-2} = \Big|&\chi^*(\mathbf{O}_{N-2}, N|\boldsymbol{\lambda}_M)\chi(\mathbf{E}_{N-2}, N|\boldsymbol{\lambda}_M)\\ &+ \chi^*(\mathbf{O}_{N-2}, N-1|\boldsymbol{\lambda}_M)\chi(\mathbf{E}_{N-2}, N-1|\boldsymbol{\lambda}_M)\Big|^2.\end{aligned} \tag{5.66}$$

Figure 5.6 shows the analytic results for $N = 10$ compared to the numerical solution of the exact diagonalization of the Hamiltonian (5.25) for the regime between two isotropic points $\Delta = \pm 1$. The correlators are much larger for the isotropic antiferromagnet because of the structure of their ground state. In the case of $\Delta = 1$, the ground state is best understood as an entangled state of many magnons, whereas for $\Delta = -1$ it corresponds to a structureless vacuum [225].

5.3.3 Majumdar-Ghosh Model

We will now discuss the Majumdar-Ghosh model [175, 176] with periodic boundary conditions, described by the Hamiltonian

$$\hat{H} = \sum_{j=1}^{N} \hat{\vec{\sigma}}^{(j)}\hat{\vec{\sigma}}^{(j+1)} + \frac{1}{2}\sum_{j=1}^{N} \hat{\vec{\sigma}}^{(j)}\hat{\vec{\sigma}}^{(j+2)}, \tag{5.67}$$

where $\hat{\vec{\sigma}}$ is Pauli vector. It is straightforward to see that it is an isotropic XXX Heisenberg spin chain with long-range interactions. The ground state of the above Hamiltonian is known exactly for the arbitrary length of the chain. Therefore, we are able to derive an expression in a closed form for correlators $\mathcal{E}_m$. Furthermore, the valence bound structure of the ground state of the Hamiltonian (5.67) helps to understand when we should expect strong correlations in the system.

The form of the ground state of the Hamiltonian (5.67)

$$|\psi\rangle = \mathcal{N}^{-1}\left(|\psi_1\rangle + |\psi_2\rangle\right) \tag{5.68}$$

is a superposition of two products of singlet states

$$|\psi_1\rangle = \bigotimes_{j=0}^{\frac{N}{2}-1} \frac{|\uparrow_{2j+1},\downarrow_{2j+2}\rangle - |\downarrow_{2j+1},\uparrow_{2j+2}\rangle}{\sqrt{2}} \tag{5.69a}$$

$$|\psi_2\rangle = \bigotimes_{j=0}^{\frac{N}{2}-1} \frac{|\uparrow_{2j+2},\downarrow_{2j+3}\rangle - |\downarrow_{2j+2},\uparrow_{2j+3}\rangle}{\sqrt{2}}, \tag{5.69b}$$

where $\mathcal{N}$ is the normalization factor

$$\mathcal{N}^2 = 2^{-N/2+2}\left(1 + 2^{N/2-1}\right). \tag{5.70}$$

The expectation values of the antiferromagnetic correlator for even m

$$\hat{\mathcal{A}}_m = \hat{\sigma}_+^{(1)}\hat{\sigma}_-^{(2)}\cdots\hat{\sigma}_+^{(m-1)}\hat{\sigma}_-^{(m)}, \tag{5.71}$$

calculated on given states, yield the following values

$$\langle\psi_{1,2}|\hat{\mathcal{A}}_N|\psi_{1,2}\rangle = \left(-\frac{1}{2}\right)^{N/2}, \tag{5.72a}$$

$$\langle\psi_{2,1}|\hat{\mathcal{A}}_N|\psi_{1,2}\rangle = \left(\frac{1}{2}\right)^{N/2}. \tag{5.72b}$$

Therefore, we obtain

$$\langle\psi|\hat{\mathcal{A}}_N|\psi\rangle = \frac{1+(-1)^{N/2}}{2}\frac{1}{1+2^{N/2-1}}. \tag{5.73}$$

For even vlaues of $N/2$ we obtain

$$\mathcal{E}_N = \frac{1}{(1+2^{N/2-1})^2}, \tag{5.74}$$

which violates the limit given by the Bell inequality 2^{-N} (and therefore the entanglement limit 2^{-2N}). The lower order correlations are also accessible, e.g. we will

calculate $\mathcal{E}_{N-2}$ (as $\mathcal{E}_{N-1} = 0$). We observe that

$$\langle\psi_1|\hat{\mathcal{A}}_{N-2}|\psi_1\rangle = \left(-\frac{1}{2}\right)^{N/2-1}, \tag{5.75a}$$

$$\langle\psi_2|\hat{\mathcal{A}}_{N-2}|\psi_1\rangle = -\left(\frac{1}{2}\right)^{N/2}, \tag{5.75b}$$

$$\langle\psi_2|\hat{\mathcal{A}}_{N-2}|\psi_2\rangle = 0 \tag{5.75c}$$

and in consequence

$$\langle\psi|\hat{\mathcal{A}}_{N-2}|\psi\rangle = -\frac{1}{2}\frac{1}{1+2^{N/2-1}}. \tag{5.76}$$

Therefore, we obtain that

$$\mathcal{E}_{N-2} = \frac{1}{4}\mathcal{E}_N. \tag{5.77}$$

The Bell inequality is violated because of the presence of the superposition in the ground state of $|\psi_1\rangle$ and $|\psi_2\rangle$ states. The value of $\mathcal{E}_m$ correlator on $|\psi_1\rangle$ alone is 2^{-m}. It is the addition of $|\psi_2\rangle$ that allows us to break the Bell limit. The ground state of the Majumdar-Ghosh model is a simple example of a state for which the hierarchy of the correlators breaks the Bell limit.

It this chapter we have shown that a single element of the density matrix possesses information about the correlation in many-body systems. Its value allows one to track how entanglement and Bell correlations expand over a large distance and number of spins in the system. This method may be applied to the many-body systems used in quantum computing, ultraprecise metrology and tests of foundations of quantum mechanics. Moreover, the formation probability is reachable experimentally with the current state-of-art in the field of quantum simulators. Additionally, a preliminary analysis of data of some experimentally reconstructed density matrices [236–238] indicates the presence of quantum correlations. We have also shown that the critical value point corresponding to a quantum phase transition is correlated with the maxima of the lower order correlators. The question of whether $\mathcal{E}_m$ can be used to construct a proper order parameter exhibiting singularity at the phase transition remains open. Nevertheless our findings may bring a new motivation into the study of the Bethe ansatz models as it relates to the methods of computation of the formation probabilities. In the next chapter we will show that the correlator $\mathcal{E}_N$, introduced in this chapter, can be used to bound the QFI and therefore we will prove that many-body nonlocality is a resource for quantum metrology.

Chapter 6

Many-body Nonlocality as a Resource for Quantum-Enhanced Metrology

Entanglement is a resource for quantum-enhanced metrology allowing for sensitivity beyond the standard quantum limit (SQL) [62, 71]. Recently, it has been shown that quantum correlations stronger than entanglement, namely EPR-steering, can be a resource for quantum-enhanced precision measurements [239]. Also, nonlocality in some particular configurations has been considered as a resource for sub shot-noise sensitivity, using the quantum Fisher information (QFI), see Eq. (2.55) [240]. In Chapter 5 we showed that a single element of the density matrix can be used to extract information about the nature of the correlations in a system. Moreover, we proved that the formation probability can also be used to track how Bell correlations and entanglement expand over a system. In this chapter we derive a lower bound of the QFI, expressed in terms of Bell correlators introduced in Chapter 5. Therefore, we establish a link between metrology and many-body nonlocality. Finally, as an illustration we apply this formalism to a one-dimensional Ising model and a Bose-Einstein condensate in a double-well potential, showing the relation between the fundamental and application-oriented aspects of nonlocality.

Contents

We begin by recalling the correlator introduced in Chapter 5:

$$\mathcal{E}_{\vec{n}_+,\vec{n}_-} = \left| \left\langle \bigotimes_{k=1}^{N} \sigma_{\pm}^{(k)} \right\rangle \right|^2 , \tag{6.1}$$

where $\sigma_{\pm}^{(k)} = \frac{1}{2}(\sigma_1^{(k)} \pm i\sigma_2^{(k)})$ and $\sigma_{1,2}^{(k)} = \pm 1$ are the outcomes of measurements for a k-th qubit. The sign "$\pm$" can be chosen independently for each party, as we did previously. This time, in the subscript of the correlator, we put labels $\vec{n}_+$ and $\vec{n}_+$, i.e. vectors consisting of the information about the order of the "$+$" and "$-$" signs in Eq. (6.1). For example, if we take $\mathcal{E}_{\vec{n}_+,\vec{n}_-}$ for the $N = 4$ body system of the form

$$\mathcal{E}_{\vec{n}_+,\vec{n}_-} = \left| \left\langle \sigma_+^{(1)} \sigma_-^{(2)} \sigma_+^{(3)} \sigma_+^{(4)} \right\rangle \right|^2 , \tag{6.2}$$

then vectors will have the following forms $\vec{n}_+ = (1, 0, 1, 1)$ and $\vec{n}_- = (0, 1, 0, 0)$, with 1 at a node where σ_+ for $\vec{n}_+$, or σ_- for $\vec{n}_-$, is present. In addition, we introduce two

scalars n_+ and n_- defined as $n_\pm = ||\vec{n}_\pm||^2$, where $||\cdot||^2$ is the square of the vector's length and $n_\pm = N - n_\mp$. If the correlator in Eq. (6.1) can be reproduced by a probability distribution $p(\lambda)$ of some hidden variable λ, then it is consistent with a local hidden-variable theory and the following inequality holds true

$$\mathcal{E}_{\vec{n}_+,\vec{n}_-} = \left| \int d\lambda\, p(\lambda) \prod_{k=1}^{N} \sigma_\pm^{(k)}(\lambda) \right|^2 \leqslant \int d\lambda\, p(\lambda) \prod_{k=1}^{N} \left| \sigma_\pm^{(k)}(\lambda) \right|^2 = 2^{-N}. \tag{6.3}$$

In the second line of Eq. (6.3) we used the Cauchy-Schwarz inequality (see Eq. (2.14)) to derive the upper bound for the correlator, $\mathcal{E}_{\vec{n}_+,\vec{n}_-} \leqslant 2^{-N}$, which is the many-body Bell inequality used to detect Bell correlations in multi-qubit systems [166–168]. We showed previously that correlator from Eq. (6.1) is associated with a single element of the density matrix, which is bounded by $|\varrho_{nm}|^2 \leqslant \frac{1}{4}$, and thus $\mathcal{E}_{\vec{n}_+,\vec{n}_-} \leqslant \frac{1}{4}$. Moreover, $\mathcal{E}_{\vec{n}_+,\vec{n}_-}$ possesses information about the depth of nonlocality or entanglement. Therefore, if $\mathcal{E}_{\vec{n}_+,\vec{n}_-} \in]\frac{1}{2^N}, \frac{1}{2^{N-1}}]$, then three out of N qubits are non-locally correlated. For $\mathcal{E}_{\vec{n}_+,\vec{n}_-} \in]\frac{1}{2^{N-1}}, \frac{1}{2^{N-2}}]$, four qubits are Bell correlated and if $\mathcal{E}_{\vec{n}_+,\vec{n}_-} \in]\frac{1}{8}, \frac{1}{4}]$, then nonlocality extends over all qubits.

In the next section we will derive a lower bound for the QFI based on the density matrix elements, and in consequence on correlators $\mathcal{E}_{\vec{n}_+,\vec{n}_-}$.

6.1 Lower Bound for the QFI

Consider a quantum system in a spectral form:

$$\hat{\varrho} = \sum_j p_j |\psi_j\rangle\langle\psi_j|, \tag{6.4}$$

where $\sum_j p_j = 1$, on which the parameter θ is imprinted, for example during the interferometric transformation described by generator $\hat{h}$. The Cramér-Rao lower bound sets a limit for the precision of the estimation process as follows [64]

$$\Delta\theta \geqslant \frac{1}{\sqrt{F_q}}, \tag{6.5}$$

where F_q is the QFI given with Eq. (2.49), namely

$$F_q(\hat{\varrho}_\theta) = \sum_{i,j} \frac{2}{p_i + p_j} |\langle\psi_i| \frac{\partial \hat{\varrho}_\theta}{\partial\theta} |\psi_j\rangle|^2, \tag{6.6}$$

with $p_i + p_j \neq 0$. The evolution of such a system under the generator $\hat{h}$ is given by

$$i\partial_\theta \hat{\varrho}_\theta = [\hat{h}, \hat{\varrho}_\theta]. \tag{6.7}$$

Therefore, Eq. (6.6) can be rewritten in the following way

$$F_q(\hat{\varrho}_\theta) = \sum_{i,j} \frac{2}{p_i + p_j} |\langle\psi_i| [\hat{\varrho}_\theta, \hat{h}] |\psi_j\rangle|^2. \tag{6.8}$$

Since all the probabilities p_i are non-negative, and for any i and j the condition $p_i + p_j \leqslant 1$ holds, we can bound the QFI from below by

$$F_q \geqslant 2 \sum_{i,j} |\langle\psi_i|[\hat{\varrho}_\theta, \hat{h}]|\psi_j\rangle|^2. \tag{6.9}$$

As a consequence, the sum over j can be performed instantly and the commutator can be expanded in the following way

$$\begin{aligned} 2\sum_{i,j}\langle\psi_i|[\hat{\varrho}_\theta, \hat{h}]|\psi_j\rangle\langle\psi_j|[\hat{\varrho}_\theta, \hat{h}]^\dagger|\psi_i\rangle &= 2\sum_i\langle\psi_i|[\hat{\varrho}_\theta, \hat{h}][\hat{\varrho}_\theta, \hat{h}]^\dagger|\psi_i\rangle = \\ &= 2\sum_i\langle\psi_i|(\hat{\varrho}_\theta\hat{h}^2\hat{\varrho}_\theta + \hat{h}\hat{\varrho}_\theta^2\hat{h} - \hat{\varrho}_\theta\hat{h}\hat{\varrho}_\theta\hat{h} - \hat{h}\hat{\varrho}_\theta\hat{h}\hat{\varrho}_\theta)|\psi_i\rangle. \end{aligned} \tag{6.10}$$

Each of the terms in the last expression of Eq. (6.10) can be calculated independently as follows

$$\sum_i\langle\psi_i|\hat{\varrho}_\theta\hat{h}^2\hat{\varrho}_\theta|\psi_i\rangle = \sum_i p_i^2\langle\psi_i|\hat{h}^2|\psi_i\rangle = \mathrm{Tr}\left[\hat{\varrho}_\theta^2\hat{h}^2\right], \tag{6.11a}$$

$$\sum_i\langle\psi_i|\hat{h}\hat{\varrho}_\theta^2\hat{h}|\psi_i\rangle = \sum_i\langle\psi_i|\hat{h}\sum_j p_j^2|\psi_j\rangle\langle\psi_j|\hat{h}|\psi_i\rangle = \sum_j p_j^2\langle\psi_j|\hat{h}^2|\psi_j\rangle = \mathrm{Tr}\left[\hat{\varrho}_\theta^2\hat{h}^2\right], \tag{6.11b}$$

$$\sum_i\langle\psi_i|\hat{\varrho}_\theta\hat{h}\hat{\varrho}_\theta\hat{h}|\psi_i\rangle = \mathrm{Tr}\left[(\hat{\varrho}_\theta\hat{h})^2\right], \tag{6.11c}$$

$$\sum_i\langle\psi_i|\hat{h}\hat{\varrho}_\theta\hat{h}\hat{\varrho}_\theta|\psi_i\rangle = \mathrm{Tr}\left[\hat{h}\hat{\varrho}_\theta\hat{h}\hat{\varrho}_\theta\right] = \mathrm{Tr}\left[\hat{\varrho}_\theta\hat{h}\hat{\varrho}_\theta\hat{h}\right] = \mathrm{Tr}\left[(\hat{\varrho}_\theta\hat{h})^2\right]. \tag{6.11d}$$

Therefore, the lower bound given in Eq. (6.9) now reads

$$F_q \geqslant 4\left(\mathrm{Tr}\left[\hat{\varrho}_\theta^2\hat{h}^2\right] - \mathrm{Tr}\left[(\hat{\varrho}_\theta\hat{h})^2\right]\right). \tag{6.12}$$

Since the elements of the density matrix can be expressed in the language of the correlators $\mathcal{E}_{\vec{n}_+,\vec{n}_-}$, therefore the link between QFI and $\mathcal{E}_{\vec{n}_+,\vec{n}_-}$ can also be established.

In the next section we will rewrite the bound in the inequality (6.12) using $\mathcal{E}_{\vec{n}_+,\vec{n}_-}$ introduced at the beginning of this chapter.

6.2 Link Between Sensitivity and Nonlocality

A variety of interferometric transformations are generated by the following operator:

$$\hat{h} = \frac{1}{2}\sum_{k=1}^{N}\hat{\sigma}_\xi^{(k)}, \tag{6.13}$$

where $\hat{\sigma}_\xi^{(k)}$ is a Pauli matrix of the k-th qubit oriented along the axis $\vec{\xi} = (\xi_x, \xi_y, \xi_z)$, namely

$$\hat{\sigma}_\xi^{(k)} = \xi_x\hat{\sigma}_x^{(k)} + \xi_y\hat{\sigma}_y^{(k)} + \xi_z\hat{\sigma}_z^{(k)}, \quad |\vec{\xi}|^2 = 1. \tag{6.14}$$

The direction $\xi = y$, in the generator in Eq. (6.13), represents the Mach-Zehnder interferometer or a Ramsey interferometric sequence employed in atomic clocks, while

$\xi = z$ corresponds to a phase shift. The eigenstates of a single-qubit operator from Eq. (6.14) are

$$\hat{\sigma}_{\xi}^{(k)} | \uparrow / \downarrow \rangle_k = \pm 1 | \uparrow / \downarrow \rangle_k, \tag{6.15}$$

therefore the density matrix can be rewritten in a basis of N-qubit states $|n\rangle$

$$\hat{\varrho}_\theta = \sum_{n,m=0}^{2^N} \varrho_{nm} |n\rangle\langle m|, \tag{6.16}$$

where $|n\rangle$ is the product of the eigenstates given by Eq. (6.15) and $\varrho_{nm} \equiv \varrho_{nm}(\theta)$. The summation indices, n and m, go over all the combinations of $\uparrow$ and $\downarrow$ independently for each qubit. Moreover, $|n\rangle$ is an eigenstate of $\hat{h}$, i.e.

$$\hat{h}|n\rangle = \left(n_\uparrow - \frac{N}{2} \right) |n\rangle, \tag{6.17}$$

where $n_\uparrow$ is the number of $|\uparrow\rangle$ qubits in $|n\rangle$ and, as a consequence of the collective character of the generator $\hat{h}$ given in Eq. (6.13), each eigenstate is $\binom{N}{n_\uparrow}$ times degenerated. Therefore, the first term in the inequality (6.12) can be rewritten in a basis of $|n\rangle$ as follows:

$$\begin{aligned} \mathrm{Tr}\left[\hat{\varrho}^2 \hat{h}^2\right] &= \mathrm{Tr}\left[\sum_{n,k,m} \left(n_\uparrow - \frac{N}{2} \right) \left(m_\uparrow - \frac{N}{2} \right) \varrho_{nk} \varrho_{km} |n\rangle\langle m| \right] = \\ &= \sum_{n,m} \left(n_\uparrow - \frac{N}{2} \right)^2 |\varrho_{nm}|^2, \end{aligned} \tag{6.18}$$

where we used the cyclic property of trace operation, i.e. $\mathrm{Tr}\left[\hat{\varrho}^2 \hat{h}^2\right] = \mathrm{Tr}\left[\hat{h}\hat{\varrho}^2\hat{h}\right]$. Following the same pattern for the second term, i.e. $\mathrm{Tr}\left[(\hat{\varrho}\hat{h})^2\right] = \mathrm{Tr}\left[\hat{h}\hat{\varrho}\hat{h}\hat{\varrho}\right]$, we obtain

$$\begin{aligned} \mathrm{Tr}\left[(\hat{\varrho}\hat{h})^2\right] &= \mathrm{Tr}\left[\sum_{n,m} \left(n_\uparrow - \frac{N}{2} \right) \left(m_\uparrow - \frac{N}{2} \right) \varrho_{nm} |n\rangle\langle m| \sum_{k,l} \varrho_{kl} |k\rangle\langle l| \right] = \\ &= \sum_{n,m} \left(n_\uparrow - \frac{N}{2} \right) \left(m_\uparrow - \frac{N}{2} \right) |\varrho_{nm}|^2. \end{aligned} \tag{6.19}$$

Finally, linking both expressions leads to the following result

$$\begin{aligned} F_q \geqslant 4 \sum_{n,m} \left[\left(n_\uparrow - \frac{N}{2} \right)^2 - \left(n_\uparrow - \frac{N}{2} \right) \left(m_\uparrow - \frac{N}{2} \right) \right] |\varrho_{nm}|^2 = \\ = 4 \sum_{n,m} \left(n_\uparrow - \frac{N}{2} \right) (n_\uparrow - m_\uparrow) |\varrho_{nm}|^2. \end{aligned} \tag{6.20}$$

We split the sum into two equal parts and then, after exchanging the indices $n \leftrightarrow m$ in one of them, we obtain

$$F_q \geqslant 2\sum_{n,m}\left(n_\uparrow - \frac{N}{2}\right)(n_\uparrow - m_\uparrow)|\varrho_{nm}|^2 + 2\sum_{n,m}\left(m_\uparrow - \frac{N}{2}\right)(m_\uparrow - n_\uparrow)|\varrho_{mn}|^2. \quad (6.21)$$

For any density matrix we have $|\varrho_{mn}|^2 = |\varrho_{nm}|^2$; therefore, the expression we obtain in the final expression (6.21) simplifies significantly to

$$F_q \geqslant 2\sum_{n,m}(n_\uparrow - m_\uparrow)^2|\varrho_{nm}|^2. \quad (6.22)$$

Please note: for a single term in this sum any $|m\rangle$ can be obtained from any state $|n\rangle$ by using a proper combination of n_+ number of rising operators and n_- number of lowering operators

$$|m\rangle = \hat{\mathcal{R}}_{\vec{n}_+}\hat{\mathcal{L}}_{\vec{n}_-}|n\rangle. \quad (6.23)$$

The operators $\hat{\mathcal{R}}$ and $\hat{\mathcal{L}}$ are products of rising and lowering operators, respectively, given by

$$\hat{\mathcal{R}}_{\vec{n}_+} = \hat{\sigma}_+^{(i_1)}\ldots\hat{\sigma}_+^{(i_{n_+})}, \quad (6.24a)$$

$$\hat{\mathcal{L}}_{\vec{n}_-} = \hat{\sigma}_-^{(j_1)}\ldots\hat{\sigma}_-^{(j_{n_-})}, \quad (6.24b)$$

where, for two directions orthogonal to $\vec{\xi}$, $\vec{\xi}_1$ and $\vec{\xi}_2$, we have

$$\hat{\sigma}_\pm^{(k)} = \frac{1}{2}(\hat{\sigma}_{\xi_1}^{(k)} \pm i\hat{\sigma}_{\xi_2}^{(k)}). \quad (6.25)$$

Therefore, since $m_\uparrow = n_\uparrow + n_+ - n_-$, we obtain

$$\varrho_{nm} = \langle n|\hat{\varrho}\hat{\mathcal{R}}_{\vec{n}_+}\hat{\mathcal{L}}_{\vec{n}_-}|n\rangle. \quad (6.26)$$

Now we pick a set of the states $\mathcal{A}_{\vec{n}_+,\vec{n}_-}$, denoting all the basis states $|n\rangle$ that can be transformed into $|m\rangle$, and vice versa, by lowering n_- and/or rising n_+ qubits. Moreover, such an operation will produce a prefactor $(n_\uparrow - m_\uparrow)^2 = (n_+ - n_-)^2$, which will be common for $2^{N-(n_+-n_-)}$ due to the fact that one $|n\rangle$ can be produced from multiple $|m\rangle$ using the same number of rising and lowering operations, but in different permutations.

In order to derive the final bound, we need to introduce one more relation, namely

$$\sum_{i=1}^{n}|a_i|^2 \geqslant \frac{1}{2^n}\left|\sum_{i=1}^{n}a_i\right|^2, \quad (6.27)$$

which holds true for any set of 2^n complex numbers (see Appendix B). Therefore, we can sum up the modulus square of the density matrix element, namely

$$\sum_{n,m\in\mathcal{A}_{\vec{n}_+,\vec{n}_-}}|\varrho_{nm}|^2 \geqslant \frac{1}{2^{N-(n_++n_-)}}\left|\mathrm{Tr}\left[\hat{\varrho}\hat{\mathcal{R}}_{\vec{n}_+}\hat{\mathcal{L}}_{\vec{n}_-}\right]\right|^2, \quad (6.28)$$

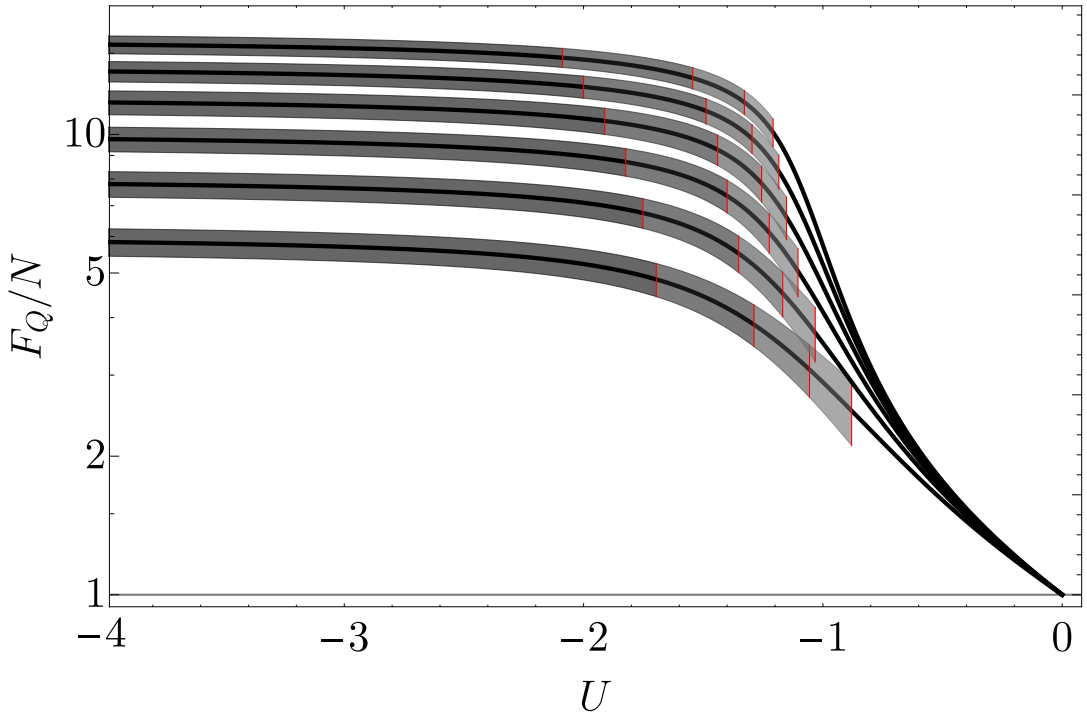

Figure 6.1: The QFI (black solid lines) normalized to standard quantum limit (gray solid line) for the Ising model as a function of U for $N = 6, 8, 10, 12, 14, 16$ (starting from the bottom line for $N = 6$). Regions where the correlator $\mathcal{E}_{N,0}$ detects at least k-partite nonlocality are marked on top of each curve, with the darkest patch corresponding to the maximally nonlocal state. The brightest region corresponds to the case where at least $N - 3$ qubits are Bell-correlated. The red lines separate regimes with different strengths of nonlocality. The plot shows that the F_q grows monotonously with the increase of the number of nonlocally correlated qubits.

as

$$\sum_{n,m\in\mathcal{A}_{\vec{n}_+,\vec{n}_-}} \varrho_{nm} = \mathrm{Tr}\left[\hat{\varrho}\hat{\mathcal{R}}_{\vec{n}_+}\hat{\mathcal{L}}_{\vec{n}_-}\right]. \tag{6.29}$$

Since the above expression corresponds to the average of the correlator in Eq. (6.1) we can define $\mathcal{E}_{\vec{n}_+,\vec{n}_-}$ as follows:

$$\mathcal{E}_{\vec{n}_+,\vec{n}_-} := \left|\mathrm{Tr}\left[\hat{\varrho}\hat{\mathcal{R}}_{\vec{n}_+}\hat{\mathcal{L}}_{\vec{n}_-}\right]\right|^2. \tag{6.30}$$

We put the inequality (6.28) in the expression for the lower bound of the QFI from Eq. (6.22) with the proper sum order: first all possible permutations of $\vec{n}_+$ and $\vec{n}_-$ for their fixed lengths, and then over n_+ and n_-. As a result, we obtain the central expression of this chapter:

$$F_q \geqslant 2\sum_{n_+=0}^{N}\sum_{n_-=0}^{N-n_+}\frac{(n_+-n_-)^2}{2^{N-(n_++n_-)}}\sum_{\vec{n}_+,\vec{n}_-}\mathcal{E}_{\vec{n}_+,\vec{n}_-}. \tag{6.31}$$

Therefore, we showed that the QFI and hence the metrological sensitivity is lower-bounded by a combination of correlators of all orders $\mathcal{E}_{\vec{n}_+,\vec{n}_-}$ with non-negative coefficients.

Let us now analyze this expression for some particular states. First we take a pure coherent spin state of N qubits of a form

$$|\psi\rangle = \bigotimes_{k=1}^{N} \frac{1}{\sqrt{2}} \left(|\uparrow\rangle_k + |\downarrow\rangle_k \right). \tag{6.32}$$

In this case the correlator is $\mathcal{E}_{\vec{n}_+,\vec{n}_-} = \left(\frac{1}{4}\right)^{n_+ + n_-}$ for all $\vec{n}_+$ and $\vec{n}_-$, which is a consequence of the spin-permutation symmetry. The inequality (6.27) is therefore saturated and the sums in the inequality (6.31) can be calculated. The QFI for the coherent spin state in Eq. (6.32) reaches the upper bound for any system of N classically correlated spins, the standard quantum limit, as $F_q = N$. In order to obtain sub-shot noise sensitivity, any one of the correlators $\mathcal{E}_{\vec{n}_+,\vec{n}_-}$ has to grow minimally from the entanglement-threshold value $\mathcal{E}_{\vec{n}_+,\vec{n}_-} = \left(\frac{1}{4}\right)^{n_+ + n_-}$ [167, 241], but not necessarily above the Bell limit $\mathcal{E}_{\vec{n}_+,\vec{n}_-} = \left(\frac{1}{2}\right)^{n_+ + n_-}$. Nevertheless, the many-body nonlocality can be a resource for high sensitivity. For example, if $\mathcal{E}_{N,0} > \frac{1}{4}\frac{1}{2^{m+1}}$, therefor the minimum of $N - m$ qubits are correlated nonlocally, and the QFI inequality (6.31) gives

$$F_q \geqslant \frac{N^2}{2^{m+1}}. \tag{6.33}$$

In a case where all qubits are nonlocally correlated, $m = 0$, the right-hand side of the inequality is $N^2/2$ given by a single correlator $\mathcal{E}_{N,0}$.

For the Greenberger-Horne-Zeilinger (GHZ) state

$$|\psi\rangle = \frac{1}{\sqrt{2}} \left(\bigotimes_{k=1}^{N} |\uparrow\rangle_k + \bigotimes_{k=1}^{N} |\downarrow\rangle_k \right), \tag{6.34}$$

the QFI reaches the Heisenberg limit, namely $F_q = N^2$, due to the fact that all N qubits are Bell-correlated ($\mathcal{E}_{N,0} = \mathcal{E}_{0,N} = \frac{1}{4}$).

We will now present some prominent examples of many-body systems in order to illustrate our results.

Examples

First, we consider the antiferromagnetic Ising Hamiltonian with open boundary conditions introduced in Chapter 5, namely:

$$\hat{H} = U \sum_{j=1}^{N-1} \hat{\sigma}_z^{(j)} \hat{\sigma}_z^{(j+1)} - \sum_{j=1}^{N} \hat{\sigma}_x^{(j)}, \tag{6.35}$$

where U is the strength of the two-body interactions. We find numerically the ground state of the system for different values of $U < 0$ and calculate the QFI in Eq. (6.6) with the generator in Eq. (6.13) in the direction $\xi = z$. We perform numerical calculations for $N = 6, 8, 10, 12, 14$ and 16. We plot the results on Fig. 6.1 with the gray regions corresponding to the values of U for which $\mathcal{E}_{N,0}$ detects the many-body nonlocality of the growing order. The region of the highest correlations is highlighted with the darkest gray, while the lightest gray shows $(N-3)$-body nonlocality. We observe

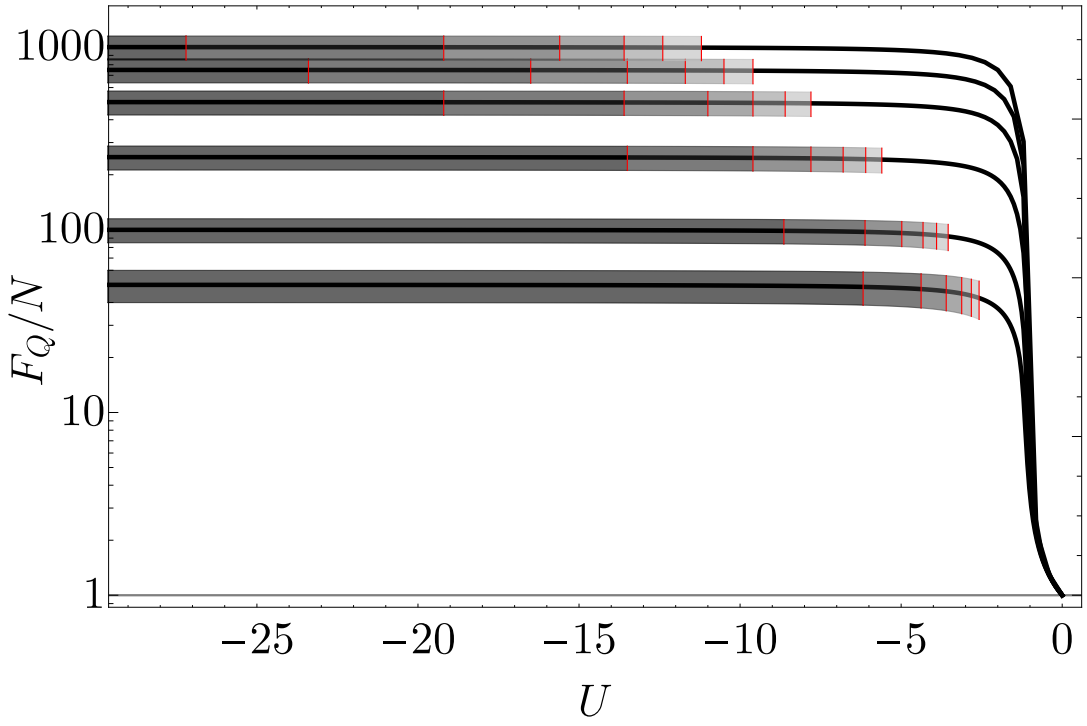

Figure 6.2: The QFI (black solid lines) normalized to standard quantum limit (gray solid line) for the Bose-Einstein condensate in a double-well model as a function of U for $N = 50, 100, 250, 500, 750, 1000$ (starting from the bottom line for $N = 50$). Regions where the correlator $\mathcal{E}_{N,0}$ detects at least k-partite nonlocality are marked on top of each curve, with the darkest patch corresponding to the maximally nonlocal state. The brightest region corresponds to the case where at least $N - 5$ qubits are Bell-correlated. The red lines separate regimes with different strengths of nonlocality. For higher N, the Heisenberg level is approached even when $n < N$ qubits are nonlocally correlated.

that the growing depth of nonlocality is connected with the QFI approaching the Heisenberg limit, in agreement with Eq. (6.33).

As the second example, we take an ultra-cold Bose gas in a double-well trap, for which we recall Hamiltonian in the form:

$$\hat{H} = -\hat{J}_x + U\hat{J}_z^2, \tag{6.36}$$

with, once again, U standing for interactions. The collective spin operators $\hat{J}_x$ and $\hat{J}_z$ are defined by Eq. (6.13) with $\xi = x$ and $\xi = z$, respectively. As we showed in previous chapters, the ground state of this system undergoes a quantum phase transition at $U = -1$ [94, 242]. The interesting regime for our purposes, and from the perspective of the correlator $\mathcal{E}_{N,0}$, would then be $U \in]-\infty, -1]$ as for $U \to -\infty$ the ground state approaches the GHZ state given in Eq. (6.34). In Fig. 6.2 we plot the QFI as a function of U for $N = 50, 100, 250, 500, 750, 1000$. Again, we highlight the regions of U for which correlator $\mathcal{E}_{N,0}$ detects from $N-5$-body nonlocality (the lightest gray area) to a fully nonlocally correlated state of N qubits (the darkest gray area). We observe that the system is highly nonlocal, whenever $F_q/N \simeq N$. For a sufficiently large number of qubits the Heisenberg limit plateau is reached even for $n < N$ nonlocally correlated qubits, because the coefficient $(n_+ - n_-)^2$ from Eq. (6.31) remains close to N^2. Therefore, for $N \to \infty$, it is not necessary to have all qubits correlated to obtain

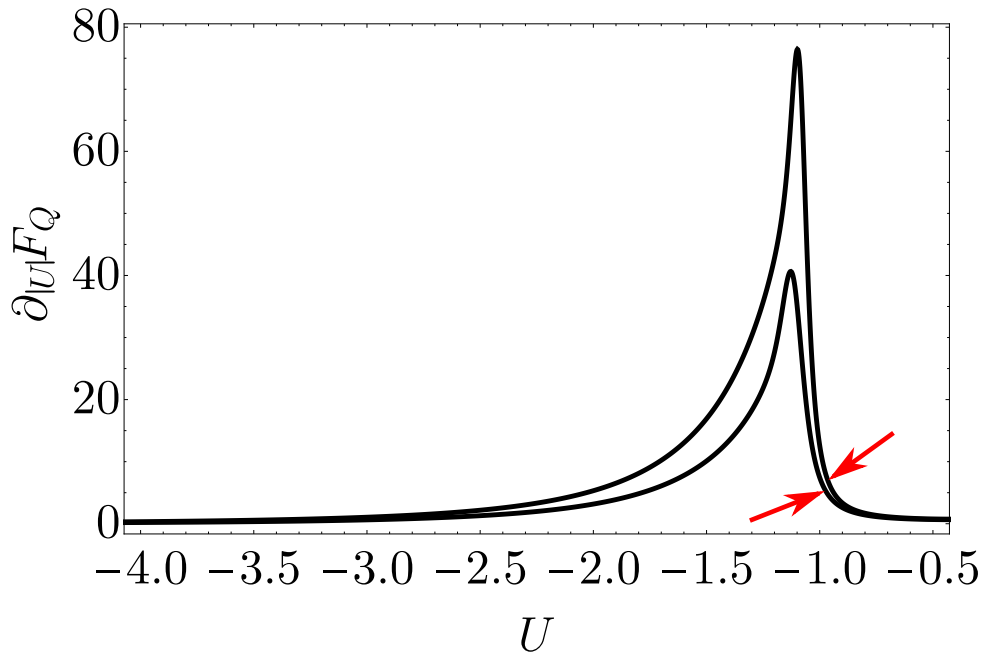

Figure 6.3: The derivative of QFI with respect to U for $N = 100$ (bottom) and 150 (top). The curves show a rapid growth around the point of quantum phase transition $U = -1$, which corresponds to the moment when sensitivity in Figs. 6.1 and 6.2 grows rapidly as well. The red arrows indicate the value of U at the point where the correlator is able to witness the Bell correlations, $\mathcal{E}_{N,0} > \frac{1}{2^N}$.

Heisenberg-like scaling. However, the many-body nonlocality is sufficient to achieve high sensitivity.

In Fig. 6.3 we plot the derivative of the QFI (black solid lines) in respect to $|U|$ for $N = 100$ and $N = 150$. The rapid growth around quantum phase transition, $U = -1$, is accompanied by the appearance of 3-body Bell correlations, $\mathcal{E}_{N,0} > \frac{1}{2^N}$, as marked by red arrows. This shows the importance of nonlocality for quantum metrology and the peculiarity of the quantum transition point [243, 244].

Summarizing this chapter, we have found a link between a many-body nonlocality and ultra-precise metrology. We showed that the QFI can be expressed in terms of various correlators of all orders which are able to witness nonlocality expanding over many qubits. Therefore, we were able to provide the lower bound for the sensitivity and find the necessary condition for Heisenberg-like scaling of the QFI. We presented these results with two examples of multi-qubit systems: a collection of spins forming the one-dimensional Ising model and a gas of ultra-cold atoms trapped in a double-well potential.

Summary and Conclusions

We devoted this dissertation to the study of quantum correlations in many-body systems. We investigated various many-body systems from the perspective of usefulness in quantum metrology. The following paragraphs briefly summarize the results of our work.

First we considered a Bose-Einstein condensate in a double-well potential, in which we presented a method for detecting Bell correlations using the interference pattern of two overlapping atomic clouds. We showed that a certain class of entangled states exhibits nonlocal correlations, signaled by the Bell witness closely related to the sensitivity of the double-well interferometer. Thus, the initial step towards establishing a relation between Bell nonlocality and quantum metrology was made.

We also considered systems where entangled states are produced via the dynamics governed by the unstable saddle fixed point in the mean-field phase space. We showed that these states allow for ultra-precise measurements as the quantum Fisher information reveals the Heisenberg scaling. We presented the optimal interferometric transformation in the case of two-mode and three-mode systems, and we provided the measurement that saturates the quantum Cramér-Rao bound.

In the next step, we derived a correlator that allows one to extract information about many-body entanglement and nonlocality from the single element of the density matrix. Such an object distinguishes the cases where the correlations in the state extend over all spins from the cases where fewer spins are entangled or nonlocally correlated. This was presented with examples of experimentally relevant Hamiltonians of Ising and Heisenberg spin chain models.

Finally, we presented a key result of our studies: we derived the lower bound for the quantum Fisher information in the language of the Bell correlators. This result affirms that many-body nonlocality can be a resource for highly precise measurements. Based on the examples of the Ising model and ultra-cold atoms in a two-mode configuration, we showed that rapid growth of the QFI around the critical point is driven by the appearance of the nonlocality encompassing an increasing number of particles.

Our research presented herein establishes a link between many-body nonlocality and quantum metrology. We showed that the presence of the strongest type of correlations in the entangled systems can provide high sensitivity of the quantum sensors. It is important to note that nonlocality is not a necessary condition for the quantum Fisher information beyond the standard quantum limit, since it has been shown that some quantum states with a local hidden variable model are metrologically useful [245]. We hope the results furnished in this dissertation will contribute to the application of nonlocally correlated systems in quantum information.

Appendix A

Entanglement in the System of Ultra-cold Atoms

Spin-1 Operators

Matrix Representation

$$Jx = \begin{pmatrix} 0 & 1 & 0 \\ 1 & 0 & 1 \\ 0 & 1 & 0 \end{pmatrix} \qquad Jy = \frac{i}{\sqrt{2}} \begin{pmatrix} 0 & -1 & 0 \\ 1 & 0 & -1 \\ 0 & 1 & 0 \end{pmatrix} \qquad Jz = \begin{pmatrix} 1 & 0 & 0 \\ 0 & 0 & 0 \\ 0 & 0 & -1 \end{pmatrix}$$

$$Qxy = i \begin{pmatrix} 0 & 0 & -1 \\ 0 & 0 & 0 \\ 1 & 0 & 0 \end{pmatrix} \qquad Qyz = \frac{i}{\sqrt{2}} \begin{pmatrix} 0 & -1 & 0 \\ 1 & 0 & 1 \\ 0 & -1 & 0 \end{pmatrix} \qquad Qzx = \frac{1}{\sqrt{2}} \begin{pmatrix} 1 & 0 & 0 \\ 0 & 0 & 0 \\ 0 & 0 & -1 \end{pmatrix}$$

$$Dxy = \begin{pmatrix} 0 & 0 & 1 \\ 0 & 0 & 0 \\ 1 & 0 & 0 \end{pmatrix} \qquad Y = \frac{1}{\sqrt{3}} \begin{pmatrix} 1 & 0 & 0 \\ 0 & -2 & 0 \\ 0 & 0 & 1 \end{pmatrix}$$

Second Quantization

The generators of $SU(3)$ algebra in the second quantization:

$$\hat{J}_x = \frac{1}{\sqrt{2}} \left(\hat{a}^\dagger_{-1}\hat{a}_0 + \hat{a}^\dagger_0\hat{a}_{-1} + \hat{a}^\dagger_0\hat{a}_{+1} + \hat{a}^\dagger_{+1}\hat{a}_0 \right), \tag{A.1}$$

$$\hat{Q}_{zx} = \frac{1}{\sqrt{2}} \left(-\hat{a}^\dagger_{-1}\hat{a}_0 - \hat{a}^\dagger_0\hat{a}_{-1} + \hat{a}^\dagger_0\hat{a}_{+1} + \hat{a}^\dagger_{+1}\hat{a}_0 \right), \tag{A.2}$$

$$\hat{J}_y = \frac{i}{\sqrt{2}} \left(\hat{a}^\dagger_{-1}\hat{a}_0 - \hat{a}^\dagger_0\hat{a}_{-1} + \hat{a}^\dagger_0\hat{a}_{+1} - \hat{a}^\dagger_{+1}\hat{a}_0 \right), \tag{A.3}$$

$$\hat{Q}_{yz} = \frac{i}{\sqrt{2}} \left(-\hat{a}^\dagger_{-1}\hat{a}_0 + \hat{a}^\dagger_0\hat{a}_{-1} + \hat{a}^\dagger_0\hat{a}_{+1} - \hat{a}^\dagger_{+1}\hat{a}_0 \right), \tag{A.4}$$

$$\hat{D}_{xy} = \hat{a}^\dagger_{-1}\hat{a}_{+1} + \hat{a}^\dagger_{+1}\hat{a}_{-1}, \tag{A.5}$$

$$\hat{Q}_{xy} = i \left(\hat{a}^\dagger_{-1}\hat{a}_{+1} - \hat{a}^\dagger_{+1}\hat{a}_{-1} \right), \tag{A.6}$$

$$\hat{Y} = \frac{1}{\sqrt{3}} \left(\hat{a}^\dagger_{-1}\hat{a}_{-1} - 2\hat{a}^\dagger_0\hat{a}_0 + \hat{a}^\dagger_{+1}\hat{a}_{+1} \right), \tag{A.7}$$

$$\hat{J}_z = \hat{a}^\dagger_{+1}\hat{a}_{+1} - \hat{a}^\dagger_{-1}\hat{a}_{-1}, \tag{A.8}$$

where $\hat{a}_{m_F}$ ($\hat{a}^\dagger_{m_F}$) is the annihilation (creation) operator of the atom in the m_F Zeeman component. The commutators of the above operators (plus $\hat{J}_{z,s} = \frac{1}{2}(\sqrt{3}\hat{Y} + \hat{D}_{xy})$ and $\hat{J}_{z,a} = \frac{1}{2}(\sqrt{3}\hat{Y} - \hat{D}_{xy})$) are given in the table below.

Table A.1: List of commutation relations for $SU(3)$ algebra generators and spin components in the symmetric and anti-symmetric subspace.

${}_{T_i}{}^{T_j}$	$\hat{J}_x(\hat{J}_{x,s})$	$\hat{Q}_{yz}(\hat{J}_{y,s})$	$\hat{Q}_{zx}(\hat{J}_{x,a})$	$\hat{J}_y(\hat{J}_{y,a})$	$\hat{J}_z$	$\hat{D}_{xy}$	$\hat{Q}_{xy}$	$\hat{Y}$	$\hat{J}_{z,s}$	$\hat{J}_{z,a}$
$\hat{J}_x(\hat{J}_{x,s})$	0	$2i\hat{J}_{z,s}$	$-i\hat{Q}_{xy}$	$i\hat{J}_z$	$-i\hat{J}_y$	$-i\hat{Q}_{yz}$	$i\hat{Q}_{zx}$	$-i\sqrt{3}\hat{Q}_{yz}$	$-2i\hat{Q}_{yz}$	$-i\hat{Q}_{yz}$
$\hat{Q}_{yz}(\hat{J}_{y,s})$	$-2i\hat{J}_{z,s}$	0	$-i\hat{J}_z$	$-i\hat{Q}_{xy}$	$i\hat{Q}_{zx}$	$i\hat{J}_x$	$i\hat{J}_y$	$i\sqrt{3}\hat{J}_x$	$i2\hat{J}_x$	$i\hat{J}_x$
$\hat{Q}_{zx}(\hat{J}_{x,a})$	$i\hat{Q}_{xy}$	$i\hat{J}_z$	0	$2i\hat{J}_{z,a}$	$-i\hat{Q}_{yz}$	$i\hat{J}_y$	$-i\hat{J}_x$	$-i\sqrt{3}\hat{J}_y$	$-i\hat{J}_y$	$-2i\hat{J}_y$
$\hat{J}_y(\hat{J}_{y,a})$	$-i\hat{J}_z$	$i\hat{Q}_{xy}$	$-2i\hat{J}_{z,a}$	0	$i\hat{J}_x$	$-i\hat{Q}_{zx}$	$-i\hat{Q}_{yz}$	$i\sqrt{3}\hat{Q}_{zx}$	$i\hat{Q}_{zx}$	$2i\hat{Q}_{zx}$
$\hat{J}_z$	$i\hat{J}_y$	$-i\hat{Q}_{zx}$	$i\hat{Q}_{yz}$	$-i\hat{J}_x$	0	$2i\hat{Q}_{xy}$	$-2i\hat{D}_{xy}$	0	$i\hat{Q}_{xy}$	$-i\hat{Q}_{xy}$
$\hat{D}_{xy}$	$i\hat{J}_{y,s}$	$-i\hat{J}_x$	$-i\hat{J}_y$	$i\hat{Q}_{zx}$	$-2i\hat{Q}_{xy}$	0	$2i\hat{J}_z$	0	0	0
$\hat{Q}_{xy}$	$-i\hat{Q}_{zx}$	$-i\hat{J}_y$	$i\hat{J}_x$	$i\hat{Q}_{yz}$	$2i\hat{D}_{xy}$	$-2i\hat{J}_z$	0	0	$-i\hat{J}_z$	$i\hat{J}_z$
$\hat{Y}$	$i\sqrt{3}\hat{J}_{y,s}$	$-i\sqrt{3}\hat{J}_x$	$i\sqrt{3}\hat{J}_y$	$-i\sqrt{3}\hat{Q}_{zx}$	0	0	0	0	0	0
$\hat{J}_{z,s}$	$2i\hat{J}_{y,s}$	$-i2\hat{J}_x$	$i\hat{J}_y$	$-i\hat{Q}_{zx}$	$-i\hat{Q}_{xy}$	0	$i\hat{J}_z$	0	0	0
$\hat{J}_{z,a}$	$i\hat{J}_{y,s}$	$-i\hat{J}_x$	$2i\hat{J}_y$	$-2i\hat{Q}_{zx}$	$i\hat{Q}_{xy}$	0	$-i\hat{J}_z$	0	0	0

Anti-symmetric Mean-field Phase Space

Here we will show the equivalence of the anti-symmetric subspace. Similarly to the symmetric case, we have to calculate an average value of Hamiltonian (4.4) on the spin coherent state defined for the anti-symmetric subspace in the following form

$$|\varphi,\theta\rangle_{3\mathrm{m}} = e^{-i\varphi\hat{J}_{z,a}/2}e^{-i\theta\hat{J}_{y,a}/2}|N0\rangle_a \tag{A.9}$$

where $|N0\rangle_a = \frac{\hat{g}_a^{\dagger N}}{\sqrt{N!}}|000\rangle$ with $\varphi \in (0,2\pi)$, $\theta \in (0,\pi)$. Analogically, this state is equivalent to the maximally polarized state $|N0\rangle_a$ in the anti-symmetric subspace rotated twice in the perpendicular directions. State given by Eq. (A.9) is an eigenstate of $\hat{J}_{z,a}$ with the eigenvalue N. Similarly to the symmetric sphere, it is located on the north pole of the Bloch sphere in the anti-symmetric subspace. In $SU(3)$ algebra it can be written as $|N0\rangle_a = e^{-i\pi/4\hat{Q}_{xy}}|00N\rangle$. On the south pole of the anti-symmetric Bloch sphere we have the state with N atoms in the $m_F = 0$ mode.

Therefore, an average value of Hamiltonian (4.4) calculated on the state in Eq. (A.9) is

$$\hat{H}_{3\mathrm{m},a} = \frac{\Lambda}{2}(1-z^2)\sin^2\varphi + z - 1, \tag{A.10}$$

where $z = \cos\theta$ and $\Lambda = -2/q$. The difference between Eqs. (A.10) and (4.16) suggest that the phase portrait for the anti-symmetrical subspace is rotated through $\pi/2$ around the $z-$axis.

Appendix B

Proof for the Algebraic Inequality

Here we prove that

$$\sum_{i=1}^{2^n} |a_i|^2 \geqslant \frac{1}{2^n} \Big| \sum_{i=1}^{2^n} a_i \Big|^2, \tag{B.1}$$

for any set of complex numbers $\{a_1 \dots a_{2^n}\}$. We start with the case $n = 1$. We obtain a simple expression:

$$|a_1|^2 + |a_2|^2 = \frac{1}{2} \left(|a_1 + a_2|^2 + |a_1 - a_2|^2 \right) \geqslant \frac{1}{2} |a_1 + a_2|^2. \tag{B.2}$$

Similarly, for $n = 2$

$$\begin{aligned} &|a_1|^2 + |a_2|^2 + |a_3|^2 + |a_4|^2 = \\ &= \frac{1}{4} \big(|a_1 + a_2 + (a_3 + a_4)|^2 + |a_1 + a_2 - (a_3 + a_4)|^2 + |a_1 - a_2 + (a_3 - a_4)|^2 + \\ &+ |a_1 - a_2 - (a_3 - a_4)|^2 \big) \geqslant \frac{1}{4} |a_1 + a_2 + a_3 + a_4|^2. \end{aligned} \tag{B.3}$$

The calculations can be generalized for higher n as follows: first, we divide the full expression into two, namely

$$b_1 = \sum_{i=1}^{2^{n-1}} a_i, \quad b_2 = \sum_{i=1}^{2^{n-1}} a_{i+2^{n-1}} \tag{B.4}$$

and we apply the formula (B.2) with a_1 and a_2 replaced with b_1 and b_2. Next, we put a minus sign between b_1 and b_2, obtaining

$$c_1 = \sum_{i=1}^{2^{n-2}} a_i - \sum_{i=1}^{2^{n-2}} a_{i+2^{n-2}}, \tag{B.5}$$

$$c_2 = \sum_{i=1}^{2^{n-2}} a_{i+2^{n-1}} - \sum_{i=1}^{2^{n-2}} a_{i+2^{n-1}+2^{n-2}}. \tag{B.6}$$

This procedure is repeated 2^n times, giving 2^n terms

$$\sum_{i=1}^{2^n} |a_i|^2 = \frac{1}{2^n} (|b_1 + b_2|^2 + |b_1 - b_2|^2 + |c_1 + c_2|^2 + |c_1 - c_2|^2 + \dots). \tag{B.7}$$

Neglecting all the terms but the first one, leads to the inequality (B.1).

Bibliography

1. Einstein, A. Über einen die Erzeugung und Verwandlung des Lichtes betreffenden heuristischen Gesichtspunkt. *Annalen der Physik* **322,** 132–148 (1905).
2. Nielsen, M. A. & Chuang, I. L. *Quantum computation and quantum information* (Cambridge University Press, 2000).
3. Einstein, A., Podolsky, B. & Rosen, N. Can Quantum-Mechanical Description of Physical Reality Be Considered Complete? *Phys. Rev.* **47,** 777–780 (1935).
4. Bell, J. S. On the Einstein Podolsky Rosen paradox. *Physics* **1,** 195 (1964).
5. Von Neumann, J. *Mathematische Grundlagen der Quantenmechanik* (Springer, Berlin, 1932).
6. Bohm, D. *Quantum Theory and Measurement* (Prentice-Hall,INC. Englewood-Cliffs, N.J., 1951).
7. Landau, L. & Lifshitz, E. *Quantum Mechanics* (Pergamon, 1974).
8. Hong, C. K., Ou, Z. Y. & Mandel, L. Measurement of subpicosecond time intervals between two photons by interference. *Phys. Rev. Lett.* **59,** 2044–2046 (1987).
9. Erkmen, B. I. & Shapiro, J. H. Ghost imaging: from quantum to classical to computational. *Advances in Optics and Photonics* **2,** 405–450 (2010).
10. Wasak, T., Szańkowski, P., Wasilewski, W. & Banaszek, K. Entanglement-based signature of nonlocal dispersion cancellation. *Physical Review A* **82,** 052120 (2010).
11. Blatt, R. & Wineland, D. Entangled states of trapped atomic ions. *Nature* **453,** 1008–1015 (2008).
12. Sørensen, A. & Mølmer, K. Entanglement and quantum computation with ions in thermal motion. *Phys. Rev. A* **62,** 022311 (2000).
13. Vogels, J. M., Xu, K. & Ketterle, W. Generation of Macroscopic Pair-Correlated Atomic Beams by Four-Wave Mixing in Bose-Einstein Condensates. *Phys. Rev. Lett.* **89,** 020401 (2002).
14. Bonneau, M. *et al.* Tunable source of correlated atom beams. *Phys. Rev. A* **87,** 061603 (2013).
15. Perrin, A. *et al.* Observation of Atom Pairs in Spontaneous Four-Wave Mixing of Two Colliding Bose-Einstein Condensates. *Phys. Rev. Lett.* **99,** 150405 (2007).
16. Krachmalnicoff, V. *et al.* Spontaneous Four-Wave Mixing of de Broglie Waves: Beyond Optics. *Phys. Rev. Lett.* **104,** 150402 (2010).
17. Lopes, R. *et al.* Atomic Hong-Ou-Mandel experiment. *Nature* **520,** 66–68 (2015).
18. Lewis-Swan, R. J. & Kheruntsyan, K. Proposal for demonstrating the Hong–Ou–Mandel effect with matter waves. *Nature Communications* **5** (2014).
19. Shapiro, J. H. & Boyd, R. W. The physics of ghost imaging. *Quantum Information Processing* **11,** 949–993 (2012).

20. Khakimov, R. I. *et al.* Ghost imaging with atoms. *Nature* **540,** 100–103 (2016).
21. Jaskula, J.-C. *et al.* Sub-Poissonian number differences in four-wave mixing of matter waves. *Phys. Rev. Lett.* **105,** 190402 (2010).
22. Kheruntsyan, K. V. *et al.* Violation of the Cauchy-Schwarz Inequality with Matter Waves. *Phys. Rev. Lett.* **108,** 260401 (2012).
23. Wasak, T., Sza ńkowski, P., Zi ń, P., Trippenbach, M. & Chwede ńczuk, J. Cauchy-Schwarz inequality and particle entanglement. *Phys. Rev. A* **90,** 033616 (2014).
24. Wasak, T., Szańkowski, P., Trippenbach, M. & Chwedeńczuk, J. Cauchy–Schwarz inequality for general measurements as an entanglement criterion. *Quantum Information Processing* **15,** 269–278 (2015).
25. Horodecki, R., Horodecki, P., Horodecki, M. & Horodecki, K. Quantum entanglement. *Rev. Mod. Phys.* **81,** 865–942 (2009).
26. Werner, R. F. Quantum states with Einstein-Podolsky-Rosen correlations admitting a hidden-variable model. *Phys. Rev. A* **40,** 4277–4281 (1989).
27. Dür, W., Vidal, G. & Cirac, J. I. Three qubits can be entangled in two inequivalent ways. *Phys. Rev. A* **62,** 062314 (2000).
28. Gühne, O. & Tóth, G. Entanglement detection. *Physics Reports* **474,** 1–75 (2009).
29. Gühne, O., Tóth, G. & Briegel, H. J. Multipartite entanglement in spin chains. *New Journal of Physics* **7,** 229–229 (2005).
30. Wiseman, H. M., Jones, S. J. & Doherty, A. C. Steering, Entanglement, Nonlocality, and the Einstein-Podolsky-Rosen Paradox. *Phys. Rev. Lett.* **98,** 140402 (2007).
31. He, Q. Y., Drummond, P. D., Olsen, M. K. & Reid, M. D. Einstein-Podolsky-Rosen entanglement and steering in two-well Bose-Einstein-condensate ground states. *Phys. Rev. A* **86,** 023626 (2012).
32. Cavalcanti, E. G., Jones, S. J., Wiseman, H. M. & Reid, M. D. Experimental criteria for steering and the Einstein-Podolsky-Rosen paradox. *Phys. Rev. A* **80,** 032112 (2009).
33. Reid, M. D. *et al.* Colloquium. *Rev. Mod. Phys.* **81,** 1727–1751 (2009).
34. Hensen, B. *et al.* Loophole-free Bell inequality violation using electron spins separated by 1.3 kilometres. *Nature* **526,** 682–686 (2015).
35. Clauser, J. F., Horne, M. A., Shimony, A. & Holt, R. A. Proposed Experiment to Test Local Hidden-Variable Theories. *Phys. Rev. Lett.* **23,** 880–884 (1969).
36. Freedman, S. J. & Clauser, J. F. Experimental Test of Local Hidden-Variable Theories. *Phys. Rev. Lett.* **28,** 938–941 (1972).
37. Aspect, A., Grangier, P. & Roger, G. Experimental Tests of Realistic Local Theories via Bell's Theorem. *Phys. Rev. Lett.* **47,** 460–463 (1981).
38. Aspect, A., Dalibard, J. & Roger, G. Experimental Test of Bell's Inequalities Using Time- Varying Analyzers. *Phys. Rev. Lett.* **49,** 1804–1807 (1982).
39. Gröblacher, S. *et al.* An experimental test of non-local realism. *Nature* **446,** 871–875 (2007).

40. Aspect, A., Grangier, P. & Roger, G. Experimental Realization of Einstein-Podolsky-Rosen-Bohm Gedankenexperiment: A New Violation of Bell's Inequalities. *Phys. Rev. Lett.* **49,** 91–94 (1982).

41. Ou, Z. Y. & Mandel, L. Violation of Bell's Inequality and Classical Probability in a Two-Photon Correlation Experiment. *Phys. Rev. Lett.* **61,** 50–53 (1988).

42. Rarity, J. G. & Tapster, P. R. Experimental violation of Bell's inequality based on phase and momentum. *Phys. Rev. Lett.* **64,** 2495–2498 (1990).

43. Eibl, M. *et al.* Experimental observation of four-photon entanglement from parametric down-conversion. *Phys. Rev. Lett.* **90,** 200403 (2003).

44. Lanyon, B. *et al.* Experimental violation of multipartite Bell inequalities with trapped ions. *Phys. Rev. Lett.* **112,** 100403 (2014).

45. Pfaff, W. *et al.* Demonstration of entanglement-by-measurement of solid-state qubits. *Nature Physics* **9,** 29–33 (2013).

46. Ansmann, M. *et al.* Violation of Bell's inequality in Josephson phase qubits. *Nature* **461,** 504–506 (2009).

47. Schmied, R. *et al.* Bell correlations in a Bose-Einstein condensate. *Science* **352,** 441–444 (2016).

48. Hinkley, N. *et al.* An Atomic Clock with 10–18 Instability. *Science* **341,** 1215–1218 (2013).

49. Nicholson, T. L. *et al.* Systematic evaluation of an atomic clock at 2×10^{-18} total uncertainty. *Nature Communications* **6,** 6896 (2015).

50. Bloom, B. J. *et al.* An optical lattice clock with accuracy and stability at the 10^{-18} level. *Nature* **506,** 71–705 (2014).

51. Cramér, H. *Mathematical Methods of Statistics* (Princeton University Press, Princeton, 1946).

52. Rao, C. R. *Information and the Accuracy Attainable in the Estimation of Statistical Parameters. In: Kotz S., Johnson N.L. (eds) Breakthroughs in Statistics.* (Springer, New York, NY, 1992).

53. Fréchet, M. Sur l'extension de certaines evaluations statistiques au cas de petits echantillons. *Revue de l'Institut International de Statistique / Review of the International Statistical Institute* **11,** 182–205 (1943).

54. Fisher, R. A. & Russell, E. J. On the mathematical foundations of theoretical statistics. *Philosophical Transactions of the Royal Society of London. Series A, Containing Papers of a Mathematical or Physical Character* **222,** 309–368 (1922).

55. Fisher, R. A. Theory of Statistical Estimation. *Mathematical Proceedings of the Cambridge Philosophical Society* **22,** 700–725 (1925).

56. Montgomery, D. C. & Runger, G. C. *Applied Statisticsand Probability for Engineers Third Edition* (John Wiley & Sons, Inc., 2002).

57. Krischek, R. *et al.* Useful Multiparticle Entanglement and Sub-Shot-Noise Sensitivity in Experimental Phase Estimation. *Phys. Rev. Lett.* **107,** 080504 (2011).

58. Kacprowicz, M., Demkowicz-Dobrzański, R., Wasilewski, W., Banaszek, K. & Walmsley, I. A. Experimental quantum-enhanced estimation of a lossy phase shift. *Nat. Photonics* **4,** 357–360 (2010).

59. Pezzé, L., Smerzi, A., Khoury, G., Hodelin, J. F. & Bouwmeester, D. Phase Detection at the Quantum Limit with Multiphoton Mach-Zehnder Interferometry. *Phys. Rev. Lett.* **99,** 223602 (2007).

60. Hradil, Z. *et al.* Quantum Phase in Interferometry. *Phys. Rev. Lett.* **76,** 4295–4298 (1996).

61. Zawisky, M. *et al.* Phase estimation in interferometry. *Journal of Physics A: Mathematical and General* **31,** 551–564 (1998).

62. Pezzé, L. & Smerzi, A. Entanglement, nonlinear dynamics, and the Heisenberg limit. *Phys. Rev. Lett.* **102,** 100401 (2009).

63. Helstrom, C. Minimum mean-squared error of estimates in quantum statistics. *Physics Letters A* **25,** 101–102 (1967).

64. Braunstein, S. L. & Caves, C. M. Statistical distance and the geometry of quantum states. *Phys. Rev. Lett.* **72,** 3439–3443 (1994).

65. Braunstein, S. L., Caves, C. M. & Milburn, G. Generalized Uncertainty Relations: Theory, Examples, and Lorentz Invariance. *Annals of Physics* **247,** 135–173 (1996).

66. Hyllus, P., Gühne, O. & Smerzi, A. Not all pure entangled states are useful for sub-shot-noise interferometry. *Phys. Rev. A* **82,** 012337 (2010).

67. Pezzé, L. & Smerzi, A. in *Atom Interferometry: Proceedings of the International School of Physics "Enrico Fermi", Course 188, Varenna on Lake Como, Villa Monastero, 15-20 July 2013* (Societa Italiana di Fisica, 2014).

68. Hellinger, E. Neue Begründung der Theorie quadratischer Formen von unendlichvielen Veränderlichen. *Journal füür die reine und angewandte Mathematik* **1909,** 210–271 (1909).

69. Bures, D. An extension of Kakutani's theorem on infinite product measures to the tensor product of semifinite w^*-algebras. *Trans. Amer. Math. Soc.* **135,** 199–212 (1969).

70. Hübner, M. Explicit computation of the Bures distance for density matrices. *Physics Letters A* **163,** 239–242 (1992).

71. Giovannetti, V., Lloyd, S. & Maccone, L. Quantum-enhanced measurements: beating the standard quantum limit. *Science* **306,** 1330–1336 (2004).

72. Niezgoda, A. *Entanglement detection in multi-mode systems of ultra-cold bosons* MA thesis (Uniwersytet Warszawski, 2018).

73. Niezgoda, A., Chwedeńczuk, J., Pezzé, L. & Smerzi, A. Detection of Bell correlations at finite temperature from matter-wave interference fringes. *Phys. Rev. A* **99,** 062115 (2019).

74. Anderson, M. H., Ensher, J. R., Matthews, M. R., Wieman, C. E. & Cornell, E. A. Observation of Bose-Einstein Condensation in a Dilute Atomic Vapor. *Science* **269,** 198–201 (1995).

75. Andrews, M. R. *et al.* Observation of Interference Between Two Bose Condensates. *Science* **275,** 637–641 (1997).

76. Javanainen, J. Oscillatory exchange of atoms between traps containing Bose condensates. *Phys. Rev. Lett.* **57,** 3164–3166 (1986).

77. Albiez, M. *et al.* Direct Observation of Tunneling and Nonlinear Self-Trapping in a Single Bosonic Josephson Junction. *Phys. Rev. Lett.* **95,** 010402 (2005).

78. Milburn, G. J., Corney, J., Wright, E. M. & Walls, D. F. Quantum dynamics of an atomic Bose-Einstein condensate in a double-well potential. *Phys. Rev. A* **55,** 4318–4324 (1997).

79. Biedenharn, L. C., Louck, J. D. & Carruthers, P. A. *Angular Momentum in Quantum Physics: Theory and Application* (Cambridge University Press, 1984).

80. Spekkens, R. W. & Sipe, J. E. Spatial fragmentation of a Bose-Einstein condensate in a double-well potential. *Phys. Rev. A* **59,** 3868–3877 (1999).

81. Ananikian, D. & Bergeman, T. Gross-Pitaevskii equation for Bose particles in a double-well potential: Two-mode models and beyond. *Phys. Rev. A* **73,** 013604 (2006).

82. Hall, D. S., Matthews, M. R., Wieman, C. E. & Cornell, E. A. Measurements of Relative Phase in Two-Component Bose-Einstein Condensates. *Phys. Rev. Lett.* **81,** 1543–1546 (1998).

83. Böhi, P., Riedel, M., Hoffroge, J., Hänsch, T. W. & Treutlein, P. Coherent manipulation of Bose–Einstein condensates with state-dependent microwave potentials on an atom chip. *Nature Phys* **5,** 592–597 (2009).

84. Raghavan, S., Smerzi, A., Fantoni, S. & Shenoy, S. R. Coherent oscillations between two weakly coupled Bose-Einstein condensates: Josephson effects, π oscillations, and macroscopic quantum self-trapping. *Phys. Rev. A* **59,** 620–633 (1999).

85. Smerzi, A., Fantoni, S., Giovanazzi, S. & Shenoy, S. R. Quantum Coherent Atomic Tunneling between Two Trapped Bose-Einstein Condensates. *Phys. Rev. Lett.* **79,** 4950–4953 (1997).

86. Smerzi, A. & Raghavan, S. Macroscopic quantum fluctuations in the Josephson dynamics of two weakly linked Bose-Einstein condensates. *Phys. Rev. A* **61,** 063601 (2000).

87. Shchesnovich, V. S. & Trippenbach, M. Fock-space WKB method for the boson Josephson model describing a Bose-Einstein condensate trapped in a double-well potential. *Phys. Rev. A* **78,** 023611 (2008).

88. Wineland, D., Bollinger, J., Itano, W. & Heinzen, D. Squeezed atomic states and projection noise in spectroscopy. *Phys. Rev. A* **50,** 67 (1994).

89. Kitagawa, M. & Ueda, M. Squeezed spin states. *Phys. Rev. A* **47,** 5138–5143 (1993).

90. Leggett, A. J. Bose-Einstein condensation in the alkali gases: Some fundamental concepts. *Rev. Mod. Phys.* **73,** 307–356 (2001).

91. Botet, R., Jullien, R. & Pfeuty, P. Size Scaling for Infinitely Coordinated Systems. *Phys. Rev. Lett.* **49,** 478–481 (1982).

92. Gilmore, R. & Feng, D. Phase transitions in nuclear matter described by pseudospin Hamiltonians. *Nuclear Physics A* **301,** 189–204 (1978).

93. Ulyanov, V. & Zaslavskii, O. New methods in the theory of quantum spin systems. *Physics Reports* **216,** 179–251 (1992).

94. Trenkwalder, A. *et al.* Quantum phase transitions with parity-symmetry breaking and hysteresis. *Nature Physics* **12,** 826–829 (2016).

95. Nicklas, E. *et al.* Observation of Scaling in the Dynamics of a Strongly Quenched Quantum Gas. *Phys. Rev. Lett.* **115,** 245301 (2015).

96. Shin, Y. *et al.* Atom interferometry with Bose-Einstein condensates in a double-well potential. *Phys. Rev. Lett.* **92,** 050405 (2004).

97. Chwedeńczuk, J., Hyllus, P., Piazza, F. & Smerzi, A. Sub-shot-noise interferometry from measurements of the one-body density. *New J. Phys.* **14,** 093001 (2012).

98. Pezzè, L., Smerzi, A., Oberthaler, M. K., Schmied, R. & Treutlein, P. Quantum metrology with nonclassical states of atomic ensembles. *Rev. Mod. Phys.* **90,** 035005 (2018).

99. Tura, J. *et al.* Detecting nonlocality in many-body quantum states. *Science* **344,** 1256 (2014).

100. Schmied, R. *et al.* Bell correlations in a Bose-Einstein condensate. *Science* **352,** 441 (2016).

101. Shchesnovich, V. & Trippenbach, M. Fock-space WKB method for the boson Josephson model describing a Bose-Einstein condensate trapped in a double-well potential. *Phys. Rev. A* **78,** 023611 (2008).

102. Juliá-Díaz, B. *et al.* Dynamic generation of spin-squeezed states in bosonic Josephson junctions. *Phys. Rev. A* **86,** 023615 (2012).

103. Gabbrielli, M., Smerzi, A. & Pezzè, L. Multipartite entanglement at finite temperature. *Sci. Rep.* **8,** 15663 (2018).

104. Esteve, J., Gross, C., Weller, A., Giovanazzi, S. & Oberthaler, M. Squeezing and entanglement in a Bose–Einstein condensate. *Nature* **455,** 1216–1219 (2008).

105. Berrada, T. *et al.* Integrated Mach–Zehnder interferometer for Bose–Einstein condensates. *Nat. Commun.* **4** (2013).

106. Spagnolli, G. *et al.* Crossing over from attractive to repulsive interactions in a tunneling bosonic josephson junction. *Phys. Rev. Lett.* **118,** 230403 (2017).

107. Trenkwalder, A. *et al.* Quantum phase transitions with parity-symmetry breaking and hysteresis. *Nat. Phys.* **12,** 826 (2016).

108. Tura, J. *et al.* Detecting nonlocality in many-body quantum states. *Science* **344,** 1256 (2014).

109. Niezgoda, A., Witkowska, E. & Mirkhalaf, S. S. Twist-and-store entanglement in bimodal and spin-1 Bose-Einstein condensates. *Phys. Rev. A* **102,** 053315 (2020).

110. Niezgoda, A., Kajtoch, D. & Witkowska, E. Efficient two-mode interferometers with spinor Bose-Einstein condensates. *Physical Review A* **98** (2018).

111. Niezgoda, A., Kajtoch, D., Dziekańska, J. & Witkowska, E. Optimal quantum interferometry robust to detection noise using spin-1 atomic condensates. *New Journal of Physics* **21,** 093037 (2019).

112. Strobel, H. *et al.* Fisher information and entanglement of non-Gaussian spin states. *Science* **345,** 424–427 (2014).

113. Gross, C., Zibold, T., Nicklas, E., Esteve, J. & Oberthaler, M. K. Nonlinear atom interferometer surpasses classical precision limit. *Nature* **464,** 1165–1169 (2010).

114. Riedel, M. F. *et al.* Atom-chip-based generation of entanglement for quantum metrology. *Nature* **464,** 1170–1173 (2010).

115. Zhang, Z. & Duan, L.-M. Generation of Massive Entanglement through an Adiabatic Quantum Phase Transition in a Spinor Condensate. *Phys. Rev. Lett.* **111,** 180401 (2013).

116. Ling-Na, W. & You, L. Using the ground state of an antiferromagnetic spin-1 atomic condensate for Heisenberg-limited metrology. *Phys. Rev. A* **93,** 033608 (2016).

117. Kajtoch, D. & Witkowska, E. Spin squeezing in dipolar spinor condensates. *Phys. Rev. A* **93,** 023627 (2016).

118. Stamper-Kurn, D. M. & Ueda, M. Spinor Bose gases: Symmetries, magnetism, and quantum dynamics. *Rev. Mod. Phys.* **85,** 1191–1244 (2013).

119. Hamley, C. D., Gerving, C. S., Hoang, T. M., Bookjans, E. M. & Chapman, M. S. Spin-nematic squeezed in a quantum gas. *Nature Physics* **8** (2012).

120. Ockeloen, C. F., Schmied, R., Riedel, M. F. & Treutlein, P. Quantum Metrology with a Scanning Probe Atom Interferometer. *Phys. Rev. Lett.* **111,** 143001 (2013).

121. Vinit, A. & Raman, C. Precise measurements on a quantum phase transition in antiferromagnetic spinor Bose-Einstein condensates. *Phys. Rev. A* **95,** 011603 (2017).

122. Kawaguchi, Y. & Ueda, M. Spinor Bose–Einstein condensates. *Physics Reports* **520.** Spinor Bose–Einstein condensates, 253–381 (2012).

123. Gerbier, F., Widera, A., Fölling, S., Mandel, O. & Bloch, I. Resonant control of spin dynamics in ultracold quantum gases by microwave dressing. *Phys. Rev. A* **73,** 041602 (2006).

124. Law, C. K., Pu, H. & Bigelow, N. P. Quantum Spins Mixing in Spinor Bose-Einstein Condensates. *Phys. Rev. Lett.* **81,** 5257–5261 (1998).

125. Pu, H., Law, C. K., Raghavan, S., Eberly, J. H. & Bigelow, N. P. Spin-mixing dynamics of a spinor Bose-Einstein condensate. *Phys. Rev. A* **60,** 1463–1470 (1999).

126. Hamley, C. D. *Spin-nematic squeezing in a spin-1 Bose-Einstein condensate* PhD thesis (Georgia Institute of Technology, 2012).

127. Law, C. K., Pu, H. & Bigelow, N. P. Quantum Spins Mixing in Spinor Bose-Einstein Condensates. *Phys. Rev. Lett.* **81,** 5257–5261 (1998).

128. Yi, S., Müstecapl ıo ğlu, Ö. E., Sun, C. P. & You, L. Single-mode approximation in a spinor-1 atomic condensate. *Phys. Rev. A* **66,** 011601 (2002).

129. Stamper-Kurn, D. M. & Ueda, M. Spinor Bose gases: Symmetries, magnetism, and quantum dynamics. *Rev. Mod. Phys.* **85,** 1191–1244 (2013).

130. Gerving, C. S. *et al.* Non-equilibrium dynamics of an unstable quantum pendulum explored in a spin-1 Bose-Einstein condensate. *Nature Communications* **3,** 1169 EP - (2012).

131. Kruse, I. *et al.* Improvement of an Atomic Clock using Squeezed Vacuum. *Phys. Rev. Lett.* **117,** 143004 (2016).

132. Lange, K. *et al.* Entanglement between two spatially separated atomic modes. *Science* **360,** 416–418 (2018).

133. Lücke, B. *et al.* Detecting Multiparticle Entanglement of Dicke States. *Phys. Rev. Lett.* **112,** 155304 (2014).

134. Huang, Y.-X., Ma, J., Jing, X.-X. & Wang, X.-G. Spin Squeezing and Fixed-Point Bifurcation. *Communications in Theoretical Physics* **58,** 800–806 (2012).

135. Wineland, D. J., Bollinger, J. J., Itano, W. M., Moore, F. L. & Heinzen, D. J. Spin squeezing and reduced quantum noise in spectroscopy. *Phys. Rev. A* **46,** R6797–R6800 (1992).

136. Feldmann, P. *et al.* Interferometric sensitivity and entanglement by scanning through quantum phase transitions in spinor Bose-Einstein condensates. *Phys. Rev. A* **97,** 032339 (2018).

137. Duan, L.-M., Cirac, J. I. & Zoller, P. Quantum entanglement in spinor Bose-Einstein condensates. *Phys. Rev. A* **65,** 033619 (2002).

138. Hyllus, P. *et al.* Fisher information and multiparticle entanglement. *Physical Review A* **85,** 022321 (2012).

139. Giovannetti, V., Lloyd, S. & Maccone, L. Quantum Metrology. *Phys. Rev. Lett.* **96,** 010401 (2006).

140. Ferrini, J. *Macroscopic Quantum Coherent Phenomena in Bose Josephson Junctions* PhD thesis (l'Universit'e de Grenoble, 2011).

141. Schulte, M., Martínez-Lahuerta, V. J., Scharnagl, M. S. & Hammerer, K. Ramsey interferometry with generalized one-axis twisting echoes. *Quantum* **4,** 268 (2020).

142. Sorelli, G., Gessner, M., Smerzi, A. & Pezzè, L. Fast and optimal generation of entanglement in bosonic Josephson junctions. *Physical Review A* **99** (2019).

143. Kajtoch, D. & Witkowska, E. Quantum dynamics generated by the two-axis countertwisting Hamiltonian. *Phys. Rev. A* **92,** 013623 (2015).

144. André, A. & Lukin, M. D. Atom correlations and spin squeezing near the Heisenberg limit: Finite-size effect and decoherence. *Phys. Rev. A* **65,** 053819 (2002).

145. Anglin, J. R. & Vardi, A. Dynamics of a two-mode Bose-Einstein condensate beyond mean-field theory. *Phys. Rev. A* **64,** 013605 (2001).

146. Bogolyubov, N. N. Kinetic Equations. *Journal of Physics USSR* **10,** 265–274 (1046).

147. Pezzè, L., Smerzi, A., Oberthaler, M. K., Schmied, R. & Treutlein, P. Quantum metrology with nonclassical states of atomic ensembles. *Reviews of Modern Physics* **90,** 035005 (2018).

148. Greenberger, D. M., Horne, M. A. & Zeilinger, A. in *Bell's theorem, quantum theory and conceptions of the universe* 69–72 (Springer, 1989).

149. Greenberger, D. M., Horne, M. A., Shimony, A. & Zeilinger, A. Bell's theorem without inequalities. *American Journal of Physics* **58,** 1131–1143 (1990).

150. Gessner, M., Smerzi, A. & Pezzè, L. Metrological Nonlinear Squeezing Parameter. *Phys. Rev. Lett.* **122,** 090503 (2019).

151. Gerry, C. C. & Mimih, J. The parity operator in quantum optical metrology. *Contemporary Physics* **51,** 497–511 (2010).

152. Song, C. *et al.* Generation of multicomponent atomic Schrödinger cat states of up to 20 qubits. *Science* **365,** 574–577 (2019).

153. Sun, L. *et al.* Tracking photon jumps with repeated quantum non-demolition parity measurements. *Nature* **511,** 444–448 (2014).

154. Ballance, C. J., Harty, T. P., Linke, N. M., Sepiol, M. A. & Lucas, D. M. High-Fidelity Quantum Logic Gates Using Trapped-Ion Hyperfine Qubits. *Phys. Rev. Lett.* **117,** 060504 (2016).

155. Meyer, V. *et al.* Experimental Demonstration of Entanglement-Enhanced Rotation Angle Estimation Using Trapped Ions. *Phys. Rev. Lett.* **86,** 5870–5873 (2001).

156. Andersen, C. K. *et al.* Entanglement stabilization using ancilla-based parity detection and real-time feedback in superconducting circuits. *npj Quantum Information* **5,** 69 (2019).

157. Gao, Y. Y. *et al.* Entanglement of bosonic modes through an engineered exchange interaction. *Nature* **566,** 509–512 (2019).

158. Van Dam, S. B., Cramer, J., Taminiau, T. H. & Hanson, R. Multipartite Entanglement Generation and Contextuality Tests Using Nondestructive Three-Qubit Parity Measurements. *Phys. Rev. Lett.* **123,** 050401 (2019).

159. Besse, J.-C. *et al.* Parity Detection of Propagating Microwave Fields. *Phys. Rev. X* **10,** 011046 (2020).

160. Eckert, K. *et al.* Differential atom interferometry beyond the standard quantum limit. *Phys. Rev. A* **73,** 013814 (2006).

161. Streed, E. W., Jechow, A., Norton, B. G. & Kielpinski, D. Absorption imaging of a single atom. *Nat. Comm.* **3,** 1–5 (1 2012).

162. Sherson, J. F. *et al.* Single-atom-resolved fluorescence imaging of an atomic Mott insulator. *Nature* **467,** 68 (2010).

163. Zhang, H. *et al.* Collective state measurement of mesoscopic ensembles with single-atom resolution. *Phys. Rev. Lett.* **109,** 133603 (2012).

164. Hume, D. B. *et al.* Accurate Atom Counting in Mesoscopic Ensembles. *Phys. Rev. Lett.* **111,** 253001 (2013).

165. Qu, A., Evrard, B., Dalibard, J. & Gerbier, F. *Probing spin correlations in a Bose-Einstein condensate near the single atom level* 2020.

166. Cavalcanti, E. G., Foster, C. J., Reid, M. D. & Drummond, P. D. Bell inequalities for continuous-variable correlations. *Phys. Rev. Lett.* **99,** 210405 (2007).

167. He, Q., Drummond, P. & Reid, M. Entanglement, EPR steering, and Bell-nonlocality criteria for multipartite higher-spin systems. *Physical Review A* **83,** 032120 (2011).

168. Cavalcanti, E., He, Q., Reid, M. & Wiseman, H. Unified criteria for multipartite quantum nonlocality. *Physical Review A* **84,** 032115 (2011).

169. Kim, K. *et al.* Quantum simulation of the transverse Ising model with trapped ions. *New Journal of Physics* **13,** 105003 (2011).

170. Simon, J. *et al.* Quantum simulation of antiferromagnetic spin chains in an optical lattice. *Nature* **472,** 307–312 (2011).

171. Bernien, H. *et al.* Probing many-body dynamics on a 51-atom quantum simulator. *Nature* **551,** 579–584 (2017).

172. De Léséleuc, S. *et al.* Accurate Mapping of Multilevel Rydberg Atoms on Interacting Spin- 1/2 Particles for the Quantum Simulation of Ising Models. *Phys. Rev. Lett.* **120** (2018).

173. Murmann, S. *et al.* Antiferromagnetic Heisenberg Spin Chain of a Few Cold Atoms in a One-Dimensional Trap. *Phys. Rev. Lett.* **115,** 215301 (2015).

174. Graß, T. & Lewenstein, M. Trapped-ion quantum simulation of tunable-range Heisenberg chains. *EPJ Quantum Technology* **1,** 8 (2014).

175. Majumdar, C. K. & Ghosh, D. K. On Next-Nearest-Neighbor Interaction in Linear Chain. I. *Journal of Mathematical Physics* **10,** 1388–1398 (1969).

176. Majumdar, C. K. Antiferromagnetic model with known ground state. *Journal of Physics C: Solid State Physics* **3,** 911–915 (1970).

177. Tóth, G. Multipartite entanglement and high-precision metrology. *Physical Review A* **85,** 022322 (2012).

178. Dall, R. *et al.* Ideal n-body correlations with massive particles. *Nature Physics* **9,** 341–344 (2013).

179. Pan, J.-W., Bouwmeester, D., Daniell, M., Weinfurter, H. & Zeilinger, A. Experimental test of quantum nonlocality in three-photon Greenberger-Horne-Zeilinger entanglement. *Nature* **403,** 515–519 (2000).

180. Kielpinski, D. *et al.* Experimental violation of a Bell's inequality with efficient detection. *Nature* **409,** 791–794 (2001).

181. Shin, D. K. *et al.* Bell correlations between spatially separated pairs of atom. *Nature Communications* **10,** 4447 (2019).

182. Sachdev, S. *Quantum Phase Transitions* (Cambridge University Press, 1999).

183. Monroe, C. Quantum information processing with atoms and photons. *Nature* **416,** 238–246 (2002).

184. Georgescu, I. M., Ashhab, S. & Nori, F. Quantum simulation. *Reviews of Modern Physics* **86,** 153–185 (2014).

185. Esteve, J., Gross, C., Weller, A., Giovanazzi, S. & Oberthaler, M. Squeezing and entanglement in a Bose–Einstein condensate. *Nature* **455,** 1216–1219 (2008).

186. Leroux, I. D., Schleier-Smith, M. H. & Vuletić, V. Orientation-dependent entanglement lifetime in a squeezed atomic clock. *Phys. Rev. Lett.* **104,** 250801 (2010).

187. Bloch, I., Dalibard, J. & Nascimbène, S. Quantum simulations with ultracold quantum gases. *Nature Physics* **8,** 267–276 (2012).

188. Hofstetter, W. & Qin, T. Quantum simulation of strongly correlated condensed matter systems. *Journal of Physics B: Atomic, Molecular and Optical Physics* **51,** 082001 (2018).

189. Browaeys, A. & Lahaye, T. Many-body physics with individually controlled Rydberg atoms. *Nature Physics* **16,** 132–142 (2020).

190. Schmidt-Kaler, F. *et al.* Realization of the Cirac–Zoller controlled-NOT quantum gate. *Nature* **422,** 408–411 (2003).

191. Tan, T. R. *et al.* Multi-element logic gates for trapped-ion qubits. *Nature* **528,** 380–383 (2015).

192. Häffner, H. *et al.* Scalable multiparticle entanglement of trapped ions. *Nature* **438,** 643–646 (2005).

193. Korenblit, S. *et al.* Quantum simulation of spin models on an arbitrary lattice with trapped ions. *New Journal of Physics* **14,** 095024 (2012).

194. Blatt, R. & Roos, C. F. Quantum simulations with trapped ions. *Nature Physics* **8,** 277–284 (2012).

195. Bohnet, J. G. *et al.* Quantum spin dynamics and entanglement generation with hundreds of trapped ions. *Science* **352,** 1297–1301 (2016).

196. Houck, A. A., Türeci, H. E. & Koch, J. On-chip quantum simulation with superconducting circuits. *Nature Physics* **8,** 292–299 (2012).

197. Córcoles, A. D. *et al.* Demonstration of a quantum error detection code using a square lattice of four superconducting qubits. *Nature Communications* **6,** 1–10 (2015).

198. Plantenberg, J., De Groot, P., Harmans, C. & Mooij, J. Demonstration of controlled-NOT quantum gates on a pair of superconducting quantum bits. *Nature* **447,** 836–839 (2007).

199. Zeng, B., Chen, X., Zhou, D.-L. & Wen, X.-G. *Quantum Information Meets Quantum Matter* (Springer, New York, 2019).

200. Calabrese, P. & Cardy, J. Entanglement entropy and quantum field theory. *Journal of Statistical Mechanics: Theory and Experiment* **2004,** P06002 (2004).

201. Hastings, M. B. An area law for one-dimensional quantum systems. *Journal of Statistical Mechanics: Theory and Experiment* **2007,** P08024–P08024 (2007).

202. Franchini, F., Its, A. R. & Korepin, V. E. Renyi entropy of the XY spin chain. *Journal of Physics A: Mathematical and Theoretical* **41,** 025302 (2007).

203. Alba, V., Tagliacozzo, L. & Calabrese, P. Entanglement entropy of two disjoint blocks in critical Ising models. *Phys. Rev. B* **81,** 060411 (2010).

204. Alba, V., Haque, M. & Läuchli, A. M. Entanglement spectrum of the Heisenberg XXZ chain near the ferromagnetic point. *Journal of Statistical Mechanics: Theory and Experiment* **2012,** P08011 (2012).

205. Laflorencie, N. Quantum entanglement in condensed matter systems. *Physics Reports* **646,** 1–59 (2016).

206. Wald, S., Arias, R. & Alba, V. Entanglement and classical fluctuations at finite-temperature critical points. *Journal of Statistical Mechanics: Theory and Experiment* **2020,** 033105 (2020).

207. Życzkowski, K., Horodecki, P., Sanpera, A. & Lewenstein, M. Volume of the set of separable states. *Phys. Rev. A* **58,** 883–892 (1998).

208. Calabrese, P., Tagliacozzo, L. & Tonni, E. Entanglement negativity in the critical Ising chain. *Journal of Statistical Mechanics: Theory and Experiment* **2013,** P05002 (2013).

209. Ruggiero, P., Alba, V. & Calabrese, P. Entanglement negativity in random spin chains. *Physical Review B* **94** (2016).

210. Islam, R. *et al.* Measuring entanglement entropy in a quantum many-body system. *Nature* **528,** 77–83 (2015).

211. Hauke, P., Heyl, M., Tagliacozzo, L. & Zoller, P. Measuring multipartite entanglement through dynamic susceptibilities. *Nature Physics* **12,** 778–782 (2016).

212. Korepin, V. E., Bogoliubov, N. M. & Izergin, A. G. *Quantum Inverse Scattering Method and Correlation Functions* (Cambridge Univ. Press, Cambridge, 1993).

213. Shiroishi, M., Takahashi, M. & Nishiyama, Y. Emptiness Formation Probability for the One-Dimensional IsotropicXYModel. *Journal of the Physical Society of Japan* **70,** 3535–3543 (2001).

214. Razumov, A. V. & Stroganov, Y. G. Spin chains and combinatorics. *Journal of Physics A: Mathematical and General* **34,** 3185–3190 (2001).

215. Abanov, A. G. & Franchini, F. Emptiness formation probability for the anisotropic XY spin chain in a magnetic field. *Physics Letters A* **316,** 342–349 (2003).

216. Brunner, N., Cavalcanti, D., Pironio, S., Scarani, V. & Wehner, S. Bell nonlocality. *Rev. Mod. Phys.* **86,** 419–478 (2014).

217. He, Q., Cavalcanti, E., Reid, M. & Drummond, P. Bell inequalities for continuous-variable measurements. *Phys. Rev. A* **81,** 062106 (2010).

218. Abanov, A. G. *Hydrodynamics of correlated systems* in *Applications of Random Matrices in Physics* (eds Brézin, É., Kazakov, V., Serban, D., Wiegmann, P. & Zabrodin, A.) (Springer Netherlands, Dordrecht, 2006), 139–161.

219. Abanov, A. G. Hydrodynamics of correlated systems. Emptiness formation probability and random matrices. *arXiv: cond-mat/0504307* (2005).

220. Stolze, J. & Garske, T. The emptiness formation probability correlation in homogeneous and dimerized XX chains. *arXiv:0904.3519* (2009).

221. Rajabpour, M. A. Formation probabilities in quantum critical chains and Casimir effect. *EPL (Europhysics Letters)* **112,** 66001 (2015).

222. Morin-Duchesne, A., Hagendorf, C. & Cantini, L. Boundary emptiness formation probabilities in the six-vertex model at $\Delta = -\frac{1}{2}$. *Journal of Physics A: Mathematical and Theoretical* **85,** 022322 (2020).

223. Najafi, M. N. & Rajabpour, M. A. Formation probabilities and statistics of observables as defect problems in free fermions and quantum spin chains. *Physical Review B* **101** (2020).

224. Néel, M. Louis. Propriétés magnétiques des ferrites ; ferrimagnétisme et antiferromagnétisme. *Ann. Phys.* **12,** 137–198 (1948).

225. Franchini, F. An Introduction to Integrable Techniques for One-Dimensional Quantum Systems. *Lecture Notes in Physics* (2017).

226. Beccaria, M., Campostrini, M. & Feo, A. Evidence for a floating phase of the transverse ANNNI model at high frustration. *Phys. Rev. B* **76,** 094410 (2007).

227. Chandra, A. K. & Dasgupta, S. Floating phase in the one-dimensional transverse axial next-nearest-neighbor Ising model. *Phys. Rev. E* **75,** 021105 (2007).

228. Nagy, A. Exploring phase transitions by finite-entanglement scaling of MPS in the 1D ANNNI model. *New Journal of Physics* **13,** 023015 (2011).

229. Sogo, K. Ground state and low-lying excitations in the Heisenberg XXZ chain of arbitrary spin S. *Physics Letters A* **104,** 51–54 (1984).

230. Kirillov, A. N. & Reshetikhin, N. Y. Exact solution of the integrable XXZ Heisenberg model with arbitrary spin. II. Thermodynamics of the system. *Journal of Physics A: Mathematical and General* **20,** 1587–1597 (1987).

231. Sutherland, B. Two-Dimensional Hydrogen Bonded Crystals without the Ice Rule. *Journal of Mathematical Physics* **11,** 3183–3186 (1970).

232. Bethe, H. Zur Theorie der Metalle. *Zeitschrift für Physik,* 205–226 (1931).

233. Lieb, E., Schultz, T. & Mattis, D. Two soluble models of an antiferromagnetic chain. *Annals of Physics* **16,** 407–466 (1961).

234. Jordan, P. & Wigner, E. P. About the Pauli exclusion principle. *Z. Phys.* **47,** 631–651 (1928).

235. Orbach, R. Linear Antiferromagnetic Chain with Anisotropic Coupling. *Phys. Rev.* **112,** 309–316 (1958).

236. Filipp, S. *et al.* Two-qubit state tomography using a joint dispersive readout. *Phys. Rev. Lett.* **102,** 200402 (2009).

237. Mikami, H., Li, Y., Fukuoka, K. & Kobayashi, T. New high-efficiency source of a three-photon W state and its full characterization using quantum state tomography. *Phys. Rev. Lett.* **95,** 150404 (2005).

238. DiCarlo, L. *et al.* Preparation and measurement of three-qubit entanglement in a superconducting circuit. *Nature* **467,** 574–578 (2010).

239. Yadin, B., Fadel, M. & Gessner, M. Quantum metrology assisted by Einstein-Podolsky-Rosen steering. *arXiv preprint arXiv:2009.08440* (2020).

240. Fröwis, F., Fadel, M., Treutlein, P., Gisin, N. & Brunner, N. Does large quantum Fisher information imply Bell correlations? *Phys. Rev. A* **99,** 040101 (2019).

241. Niezgoda, A., Panfil, M. & Chwedeńczuk, J. Quantum correlations in spin chains. *Phys. Rev. A* **102,** 042206 (2020).

242. Dziarmaga, J., Smerzi, A., Zurek, W. & Bishop, A. Dynamics of quantum phase transition in an array of Josephson junctions. *Phys. Rev. Lett.* **88,** 167001 (2002).

243. Hauke, P., Heyl, M., Tagliacozzo, L. & Zoller, P. Measuring multipartite entanglement through dynamic susceptibilities. *Nature Physics* **12,** 778–782 (2016).

244. Piga, A., Aloy, A., Lewenstein, M. & Frérot, I. Bell Correlations at Ising Quantum Critical Points. *Phys. Rev. Lett.* **123,** 170604 (2019).

245. Tóth, G. & Vértesi, T. Quantum States with a Positive Partial Transpose are Useful for Metrology. *Phys. Rev. Lett.* **120,** 020506 (2018).